Universidad Carlos III de Madrid
www.uc3m.es

TESIS DOCTORAL

Direct Numerical Simulation of Reactive and Non-Reactive Mixing Layers

Autor:

Antonio Eduardo Almagro Fernández

Director/es:

Manuel García-Villalba Navaridas

Óscar Flores Arias

Tutor:

Manuel García-Villalba Navaridas

DEPARTAMENTO DE BIOINGENIERÍA E INGENIERÍA AEROESPACIAL

Leganés, octubre de 2017

Universidad Carlos III de Madrid
www.uc3m.es

TESIS DOCTORAL

DIRECT NUMERICAL SIMULATION OF REACTIVE AND NON-REACTIVE MIXING LAYERS

Autor: *Antonio Eduardo Almagro Fernández*

Director/es: Manuel García-Villalba Navaridas,

Óscar Flores Arias

Firma del Tribunal Calificador:

Firma

Presidente: Francisco Higuera Antón

Vocal: Daniel Mira Martínez

Secretario: Antonio Luis Sánchez

Calificación:

Leganés, de de

Direct Numerical Simulation of Reactive and Non-Reactive Mixing Layers

Turbulent flow analysis under the Low-Mach number formulation

Antonio Almagro Fernández

Supervisor: Prof. Manuel García-Villalba Navaridas

Advisor: Prof. Oscar Flores Arias

Departamento de Ingeniería Aeroespacial y Bioingeniería
Universidad Carlos III de Madrid

This dissertation is submitted for the degree of
Doctor of Philosophy

Universidad Carlos III de Madrid November 2017

I would like to dedicate this thesis to my loving mother, Ana Fernández Carrilero, who was always pushing me forward in my education, and to my father, Antonio Almagro Herrero, who is always with me.

In memory of Roberto Barco Quesada, whose love and strength enlightened me.

Acknowledgements

First of all, I would like to thank Oscar Flores and Manolo García-Villalba for their work, guidance and support. This was a long journey with some rocks on the way but we managed to finish it. I would like to thank Antonio L. Sanchez, Forman A. Williams, Amable Liñán and the department of Mechanics and Aerospace Engineering of U.C. San Diego for welcoming me there and bringing me the opportunity to learn combustion from the best. Moreover, I would like to acknowledge Sergio Hoyas and the Computational Fluid Mechanics group at E.T.S.I.A. from U.P.M, for granting me access to the Channel code for incompressible flow turbulence, that I used as a base for building my code LoMa.

In addition, I would like to acknowledge the Spanish MCINN through project CSD2010-00011 for supporting this research. Moreover, the computational resources provided by RES (Red Española de Supercomputación) and by XSEDE (Extreme Science and Engineering Discovery Environment) are gratefully acknowledged.

Thank you José Luis Ortiz and Daniel Moreno, because you made me enjoy my time in San Diego. When I arrived there for the first time you were strangers to me (well, almost...) but I went back to Spain with two very close friends and 4 seasons of The Office watched...

Thank you Felipe Hernández for your friendship. Meeting you was one of the best things of these years. Working was a bit harder since you left.

Thank you Alejandro Reyes and the Dinamics group at UC3M. You helped me to enjoy working out... It is impossible for me to imagine these years without those moments of *chill-out*.

Thank you to my office room-mates Alejandro Gonzalo, Carlos Sanmiguel, Víctor Criado and Marco Raiola. You understood my sense of humor and/or tolerated it... In our next thesis together we should work less and have more fun.

And last but not least, thank you very much Laura for your support, for coming to Madrid with me and for all the sacrifices we have made for this PhD. You are my happiness.

The journey, Not the destination matters...- T.S. Elliot

Abstract

The present dissertation deals with direct numerical simulations of reactive and non reactive, temporally evolving, low speed, variable-density turbulent plane mixing layers. The Navier-Stokes equations in the low-Mach number approximation are solved using a novel algorithm based on an extended version of the velocity-vorticity formulation used for incompressible flows. The details on the formulation, algorithms and implementation of this code are provided.

First, direct numerical simulations of the non-reactive case are performed and analyzed. Four cases with density ratios of $s = 1$, 2, 4 and 8 are considered. The simulations are run with a Prandtl number of 0.7, and achieve a Re_λ up to 150 during the self-similar evolution of the mixing layer. It is found that the growth rate of the mixing layer decreases with increasing density ratio, in agreement with theoretical models of this phenomenon. Comparison with high-speed data shows that the reduction of the growth rates with increasing the density ratio has a weak dependence with the Mach number. In addition, the shifting of the mixing layer to the low-density stream has been characterized by analyzing one point statistics within the self-similar interval. This shifting has been quantified, and related to the growth rate of the mixing layer under the assumption that the shape of the mean velocity and density profiles do not change with the density ratio. This leads to a predictive model for the reduction of the growth rate of the momentum thickness, which agrees reasonably well with the available data. Finally, the effect of the density ratio on the turbulent structure has been analyzed using flow visualizations and spectra. It is found that with increasing density ratio the longest scales in the high density side are gradually inhibited. A gradual reduction of the energy in small scales with increasing density ratio is also observed.

Second, the effects of fuel Lewis number (L_F) and dilution have been investigated for different combustion problems. In order to characterize the influence of these parameters on the flame temperature focusing on transport effects, we consider a single irreversible reaction with infinitely fast rate, with Schlab-Zeldovich coupling functions introduced to write the conservation equations of energy and reactants in a chemistry-free form. The problems analyzed are:

- Counterflow and Coflow Burke-Schumann flames: it is shown that, superadiabatic (subadiabatic) temperatures are found for $L_F < 1$ ($L_F > 1$), but these flame temperatures are not bounded by the peak temperature of diffusion-reaction systems.

- Diffusion flame in a vortex: a time-dependent planar diffusion flame distorted by a vortex is investigated. Results in the limit of $Pe >> 1$ are compared with the full solution of the problem finding good agreement. It is found that for $S < 1$ there exist regions of the flame with temperatures subadiabatic (superadiabatic) for $L_F < 1$ ($L_F > 1$).

- Diffusion flame in turbulent flows (temporal mixing layer): several cases are simulated using DNS. It is found good agreement with the flame temperature characterization obtained for the laminar cases. In particular, for $S < 1$ it is found an atypical behavior similar to the one described on the vortex flow.

The results presented in this thesis show that considering preferential diffusion effects (by means of $L_F \neq 1$) significantly alters the flame temperature distribution, with temperatures values ranging between those obtained for the laminar cases, and affected by the value of the fuel dilution S.

Abstract

La presente tesis trata de simulaciones numéricas directas de capas de mezcla turbulenta de evolución temporal, considerando densidad variable y en régimen de baja velocidad, tanto del caso reactivo como inerte. Las ecuaciones de Navier-Stokes en la formulación de low-Mach se resuelven utilizando un nuevo algoritmo basado en un versión extendida de la formulación de velocidad-vorticidad utilizada para flujos incompresibles. Los detalles de la formulación, los algoritmos desarrollados y su implementación se incluyen en este trabajo.

En primer lugar, se realizan y analizan las simulaciones numéricas directas (DNS) del caso inerte. Se consideran para este estudio cuatro casos con relaciones de densidad de $s = 1$, 2, 4 y 8, y un número de Prandtl de 0.7, alcanzando un valor de $Re_\lambda = 150$ durante la evolución auto-semejante de la capa de mezcla. Se ha observado que la tasa de crecimiento de la capa de mezcla disminuye cuando se aumenta la relación de densidades, en sintonía con las predicciones de los modelos teóricos de este fenómeno. La comparación con resultados de capas de mezcla de alta velocidad muestra que la reducción de la tasa de crecimiento con el aumento de la relación de densidades tiene una débil dependencia con el número de Mach. Además, el deslizamiento de la capa de mezcla hacia la corriente de baja densidad ha sido caracterizado analizando estadísticas durante el periodo de auto-semejanza. Este deslizamiento ha sido calculado y relacionado con la tasa de crecimiento de la capa de mezcla. En base a esto se ha obtenido un modelo predictivo para la reducción de la tasa de crecimiento del espesor de momento que concuerdo muy bien con los datos disponibles. Finalmente, el efecto de la relación de densidades en las estructuras turbulentas ha sido analizado mediante visualizaciones de flujo y análisis de espectros. Se ha visto que al aumentar la relación de densidades, las escalas más grandes del lado de alta densidad se van inhibiendo gradualmente. Una reducción gradual de la energía en las escalas pequeñas también se observa al aumentar la relación de densidades.

En segundo lugar, los efectos del número de Lewis del fuel (L_F) y la dilución han sido investigados para diferentes problemas de combustión. Para caracterizar la influencia de estos parámetros en la temperatura de llama y centrarnos en los efectos de transporte, consideramos una única reacción infinítamente rápida e irreversible, con las funciones de Schlab-

Zeldovich introducidas para reducir las ecuaciones de conservación de la energía y los reactivos a una forma sin química. Los problemas analizados son:

- Llamas de difusión Counterflow y Coflow: se encuentran temperaturas superadiabáticas (subadiabáticas) para $L_F < 1$ ($L_F > 1$), pero estas temperaturas no están limitadas por la temperatura máxima de sistemas de reacción-diffusión.

- Llamas de difusión en un vórtice: se investiga una llama de difusión plana, que evoluciona con el tiempo distorsionada por un campo de velocidades alrededor de un vórtice. Los resultados en el límite de Peclet $>> 1$ se comparan con los resultados de las ecuaciones completas, mostrando un buen acuerdo. Se muestra que para diluciones $S < 1$ existen regiones de la llama con temperaturas subadiabáticas (superadiabáticas) para $L_F < 1$ ($L_F > 1$).

- Llamas de difusión en capas de mezcla turbulenta: varios casos se simular usando DNS. Se encuentra un buen acuerdo con la caracterización de temperatura de llama obtenida para los casos laminar previamente estudiados. En particular, para $S < 1$ se encuentra un comportamiento atípico similar al descrito en el problema del vórtice.

Los resultados presentados en esta tesis muestran que la consideración de los efectos de difusión preferencial (a través de $L_F \neq 1$), alteran significativamente la distribución de temperatura en la llama, con valores de temperatura que oscilan alrededor de los obtenidos en los casos laminares e influenciados por el valor de la dilución S.

Table of contents

List of figures

List of tables

Chapter 1

Introduction

1.1 Motivation

In many industrial applications, combustion takes place in chambers where the fuel and oxidizer are injected separately (non-premixed combustion). When the chemical reaction is sufficiently fast, oxygen and fuel only coexist in a thin layer, where the reaction takes place after the reactants arrive by convection and diffusion from opposite sides. Classical examples of these *diffusion flames* are lighters, candles, diesel engines, rocket engines, or the gas burners of thermal power stations.

The limiting process in these flames is *mixing*, since the rate of reaction is determined by the rate at which the two species are brought together to the flame. However, the processes of mixing and chemical reaction in the diffusion flame occur in time scales that are not resolved in industrial simulation (LES, and mostly RANS). Because of that, temperature and concentration fluctuations must be introduced via turbulent combustion models such as the flamelets.

Many difficulties arise when trying to simulate diffusion flames due to the non-linear interaction between the different physical phenomena involved:

- Differential diffusion and fuel dilution. Departures between oxidizer and fuel stream diffusivities produce preferential diffusion, altering the resulting flame temperature. Moreover, fuel dilution also alters the flame position and its temperature.

- Turbulent transport. The Reynolds number strongly affects the transport processes. In most engineering applications, the flow is turbulent as a result of the large Reynolds number and the diffusion flames are embedded in thin mixing layers separating the air and the fuel streams.

- Thermal expansion. Fluid properties as density, viscosity and thermal conductivity are affected by strong local temperature changes produced during the combustion processes. On the other hand, in most of the applications, the flow velocity is much smaller than the sound velocity. The use of Low Mach number formulation allows to consider the thermal expansion within incompressible flow.

The lack of understanding on the interaction of these processes could lead to a bad temperature prediction by the industrial tools currently available, and therefore a bad estimation on the pollutants produced during the combustion.

1.2 State of the art

In the framework of this thesis, a diffusion flame may be defined as a non-premixed, quasisteady, nearly isobaric flame in which most of the reaction occurs in a narrow zone that can be approximated as a surface ([70]). The coupling-function formulation, as described in section §2.5 provides a convenient framework to face theses problem.

As introduced in the previous section, turbulence is present in most of the engineering applications. In general, in these turbulent diffusion flames we find strong two-way-coupling between turbulent flow and the chemical reaction, i.e. mixing of the two species is enhanced by turbulence, while the turbulent flow is altered by the chemical reaction through the variations of density and transport coefficients associated with the temperature increase [21].

This strong coupling, together with the inherent complexity of the variable-density flow, makes impossible to find efficient numerical tools commercially available. Note that, turbulent flows require high resolution (large number of grid points), therefore the simulations are computational intensive. On the other hand, the coupling between continuity and energy equations, not found on the constant-density case, requires a different strategical design with regards to algorithms and implementation.

Several fundamental analyses based on direct numerical simulations of turbulent diffusion flames in simplified geometries have been reported in the literature (see for instance [55], [36], [45], [51]). Most of them consider unity Lewis numbers of the reactants ($L_F = 1$), an assumption that limits the applicability of many of the resulting conclusions; in this situation the flame temperature is constant along the flame surface and equal to the adiabatic flame temperature. Actually, for many fuels the Lewis number L_F differs significantly from unity, the only exception being methane, for which the assumption $L_F = 1$ is fairly accurate. Thus, hydrogen has $L_F = 0.3$, while heavy hydrocarbons typically have $L_F \gtrsim 1.7$. These departures from $L_F = 1$ produce preferential diffusion, altering the resulting flame temperature (super-adiabatic temperatures for $L_F < 1$ and sub-adiabatic temperatures for $L_F > 1$). A more detailed literature survey about differential molecular diffusion is included in Chapter 4.

Since most the chemical reactions involved in combustion processes typically have a strong temperature dependence, temperature changes associated with preferential diffusion have a profound effect, in particular in connection with the production of Nitrogen oxides (NO_x), which is becoming a critical factor on the design of combustion chambers.

An additional limiting assumption of most of the studies pertain to the dilution of the fuel feed. Computations are facilitated by considering dilute fuel feed with order-unity values of the resulting air-to-fuel stoichiometric ratio S (the mass of air needed to burn the unit mass of fuel stream in stoichiometric proportions). In most realistic applications, however, the fuel

feed is undiluted, resulting in large values of $S \sim 15$. The resulting flames tend to migrate towards the air side of the mixing layers, where turbulence is more intermittent. This affects the turbulent transport of the species, which ultimately controls the rate of reaction.

As discussed on the Motivation, it is important to consider thermal expansion when simulating diffusion flames because it alters the fluid properties. Increasing temperature decreases density (and momentum) of the flow, and increases viscosity (reducing the local Reynolds numbers). Similar effects are also present in other engineering areas in non-reactive flows, like in heat exchangers and in geophysical flows. In all these cases, the velocity in the fluid is much smaller than the speed of sound (Low Mach number range [35]). As a consequence, the thermodynamic pressure is essentially constant, and density is inversely proportional to temperature. Because of this, variable density turbulence retains some of the properties of incompressible flows, although the density variations modify the momentum and energy cascades in ways that are not yet fully understood.

The variable-density effects on turbulent flows have been studied from many different fronts, as can be found on [13]. Among the first authors investigating the pressure and velocity fields of the incompressible mixing layer experimentally we find Spencer & Jones [63], Brown & Roshko [10] as well as Dimotakis & Brown [22] who identified the important role of coherent structures and their pairing for the mixing process. On the other hand, Bell & Mehta [6] showed that incompressible mixing layers attained a self-similar state with a constant thickness growth rate and a collapse of the averaged flow variables profiles. In 1994, the first Direct Numerical Simulation (DNS) of temporally evolving incompressible mixing layers up to a fully turbulent state were performed by Rogers & Moser [58]. Since then, focus shifted from Low-Mach (incompressible limit) to finite Mach (subsonic flow) turbulent flow. The Chapter 3 of this dissertation contains a more thorough review of the state of the art on this topic.

1.3 Objectives

The analysis of variable-density turbulent flows is difficult to address both experimentally and numerically. In this work, we make use of DNS in order to improve the understanding about non-reactive and reactive turbulent flows and the physical processes involved.

The primary objective of this research is to improve the understanding on turbulent diffusion flames, in particular, analyzing the effect of L_F, S and Re on the flame temperature. Due to the complexity of the flow addressed (as explained in the previous section), we have developed our own code, using a new algorithm for solving the Navier-Stokes equations under the Low-Mach approximation [47], including a generalized Burke-Schumann formulation [59].

The study is separated into two stages. In the first stage, we will focus on the characterization of variable-density effects on turbulent non-reactive flows using the canonical configuration of a temporal mixing layer. In particular, in this stage our objective is to understand how the free-stream density ratio affects the mixing layer growth rate, to describe the turbulent structures of variable-density mixing layers, and to describe the differences of the low speed case ($M \rightarrow 0$) with respect to the high speed case ($M >> 0$), where compressible effects are important.

In the second stage, our objective is to characterize the effect of preferential diffusion and dilution on the flame temperature of combustion processes. In order to focus directly on transport effects, we will consider a single irreversible reaction with infinitely fast rate, with Schlab-Zeldovich coupling functions introduced to write the conservation equations of energy and reactants in a chemistry-free form.

1.4 Outline of the dissertation

Besides this first chapter, which is a general introduction defining the objectives behind this thesis, this dissertation includes three units dealing with different aspects of the research. Chapter 2 includes the description of the formulation and numerical implementation of the two key numerical tools developed for this thesis (loMa and loMaHZ). Chapter 3 shows the results obtained for the turbulent non-reactive variable-density mixing layer case with density ratios ranging from 1 to 8, including an overview over the relevant literature. Note that, this chapter is a version from our published paper [1]. In Chapter 4, combustion problems with infinitely fast chemistry formulation are studied, including turbulent mixing layer simulations and an overview over the relevant literature of differential molecular diffusion. Finally, the Chapter 5 is dedicated to conclusion and outcome discussion about the results of this research.

Chapter 2

DNS: Formulation, implementation and computational set-up

2.1 Introduction

Two main numerical tools have been developed in order to solve two different relevant problems:

- First, the code LoMa (coming from *Low Mach*) was created aiming to study variable-density turbulent flows under the low-Mach approximation formulation. In this step, we decided to analyze the problem assuming constant viscosity and thermal conductivity. The reason behind this decision was that the available references were working under this assumption. Moreover, the algorithm and numerical treatment is much simpler this way.
- Second, the code LoMaHZ was created (starting with LoMa) in order to solve reactive mixing layers, adding the HZ formulation [59] to replace the energy evolution equation. Furthermore, the constant fluid properties assumption was revised and replaced by a temperature dependance, with the developed algorithm becoming more complicated than the non-reactive version.

After some research, we decided that, instead of starting a brand new code, it would be better to start from the incompressible code developed in the Universidad Politécnica de Madrid for turbulent channel flows ([24], [30]). This way, we took advantage of the high efficiency of the code and scalability.

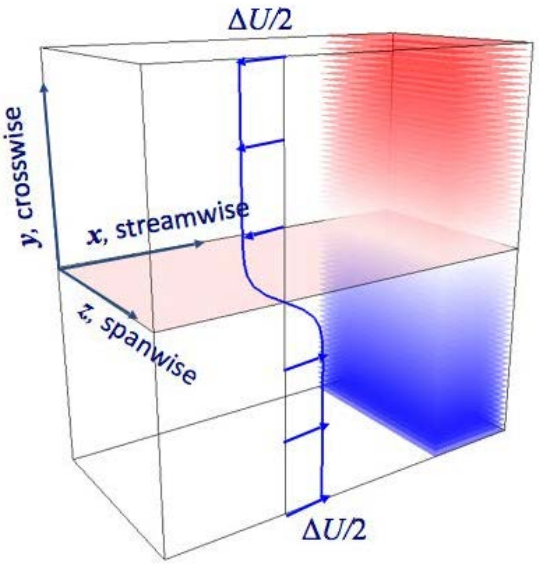

Fig. 2.1 Variable density mixing layer flow configuration sketch.

In the following, the formulation for both problems (non-reactive and reactive variable-density mixing layers) is presented. Details about implementation and computational set-up are also provided in this section.

2.2 Formulation

The flow under consideration is a three-dimensional, temporally-evolving mixing layer developing between two streams with variable density. The lower stream flows at a velocity $\Delta U/2$ in the positive x direction with a density ρ_b, while the upper stream flows at a velocity $\Delta U/2$ with density ρ_t in the oposite direction, so that the velocity difference between both streams is ΔU (see figure 2.1).

As explained in the previous chapter, for the present study we consider that temperature and density fluctuations are much more significant than pressure fluctuations. Therefore, the governing equations are the Navier-Stokes under the low Mach number approximation [44, 16, 47] together with the equation of state. These equations read (Einstein's summation

convention is employed)

$$\frac{\partial \rho}{\partial t} + \frac{\partial (\rho u_i)}{\partial x_i} = 0, \tag{2.1}$$

$$\frac{\partial (\rho u_i)}{\partial t} + \frac{\partial (\rho u_i u_j)}{\partial x_j} = -\frac{\partial p^{(1)}}{\partial x_i} + \frac{\partial \tau_{ij}}{\partial x_j}, \tag{2.2}$$

$$p^{(0)} = \rho R T, \tag{2.3}$$

where ρ is the fluid density, u_i are the velocity components, T is the temperature, τ_{ij} is the viscous stress tensor, and R is the specific gas constant.

Within the low Mach number approximation, the variables are expanded in a Taylor series where the Mach number is the small parameter. The first two terms of the pressure expansion appear in eqs. (2.1-2.3), denoted $p^{(0)}$ and $p^{(1)}$. The former, $p^{(0)}$, is usually called the thermodynamic pressure, since it only appears in the equation of state. In the present case, $p^{(0)}$ can be considered to be constant, since the temporal mixing layer is an open system [47]. The latter, $p^{(1)}$, plays the same role as in incompressible flow and it is usually called the mechanical pressure. The viscous stress tensor is given by $\tau_{ij} = \mu(\partial u_i/\partial x_j + \partial u_j/\partial x_i - 2/3\delta_{ij}(\partial u_k/\partial x_k))$, where μ is the dynamic viscosity and δ_{ij} is the Kronecker delta.

Note that we still need one equation to close the problem. In the case of non-reactive mixing layer this would be the energy conservation equation, namely

$$\rho C_p \frac{\partial T}{\partial t} + \rho C_p u_i \frac{\partial T}{\partial x_i} = \frac{\partial}{\partial x_i}\left(\kappa \frac{\partial T}{\partial x_i}\right), \tag{2.4}$$

where κ is the thermal conductivity and C_p is the specific heat at constant pressure. However, this equation is substituted by two scalar evolution equations in the reactive case. This additional set of equations require special consideration and will be presented in detail in section §2.2.1.

Compacting the formulation, the momentum equation (2.5), can be rewritten as

$$\frac{\partial \rho \vec{u}}{\partial t} = \vec{N} - \nabla p' + \vec{M} \tag{2.5}$$

With the following definitions:

$$\begin{aligned} N_i &= -\frac{\partial(\rho u_i u_j)}{\partial x_j}, \\ M_i &= \frac{\partial}{\partial x_j}\left(\mu\left(\frac{\partial u_i}{\partial x_j}+\frac{\partial u_j}{\partial x_i}\right)\right) = \frac{\partial \tau'_{ij}}{\partial x_j}, \end{aligned} \tag{2.6}$$

where the mechanical component of the pressure has absorbed the normal component of the viscous stress tensor, i.e.

$$p' = p^{(1)} + \frac{2}{3}\mu\frac{\partial u_j}{\partial x_j}. \tag{2.7}$$

Considering the role played by the mechanical pressure, we solve the governing equations using an algorithm analogous to the algorithm for incompressible flow of [34]. In that work, the momentum equation is recast in terms of two evolution equations, the first one for the vertical component of the vorticity, ω_y, and the second one for the laplacian of the vertical component of the velocity, $\nabla^2 v$. In that way, pressure is removed from the equations and continuity is enforced by construction. In order to employ a similar formulation, we decompose the momentum vector

$$\rho\vec{u} = \vec{m} + \nabla\psi, \tag{2.8}$$

where $\vec{m}$ is a divergence-free component, so that

$$\frac{\partial m_x}{\partial x} + \frac{\partial m_y}{\partial y} + \frac{\partial m_z}{\partial z} = 0, \tag{2.9}$$

and $\nabla\psi$ is a curl-free component. We define Ω_y as the vertical component of the rotor of the momentum vector, namely

$$\Omega_y = \frac{\partial m_x}{\partial z} - \frac{\partial m_z}{\partial x}, \tag{2.10}$$

and ϕ as the laplacian of the vertical component of $\vec{m}$,

$$\phi = \nabla^2 m_y \tag{2.11}$$

Hence, equations (2.1-2.4) can be recast as evolution equations for T, Ω_y, ϕ. By taking the curl of (2.5) we obtain the evolution equation for Ω_y as

$$\frac{\partial \Omega_y}{\partial t} = \frac{\partial N_x}{\partial z} - \frac{\partial N_z}{\partial x} + \left(\frac{\partial M_x}{\partial z} - \frac{\partial M_z}{\partial x} \right), \tag{2.12}$$

note that, by taking the curl, the pressure term defined as a gradient has been eliminated.

When considering constant fluid properties, the last term of eq. (2.12) can be manipulated and be expressed as a function of the vertical component of the vorticity ω_y

$$\frac{\partial M_x}{\partial z} - \frac{\partial M_z}{\partial x} = \mu \nabla^2 \omega_y \tag{2.13}$$

In order to find the evolution equation for ϕ, we make use of the algebra identity over the curl of the curl, namely

$$\nabla \times \vec{\Omega} = -\nabla^2 \vec{m} \tag{2.14}$$

Now, we can take the curl of equation (2.12) in order to find the evolution equation for ϕ:

$$\frac{\partial \phi}{\partial t} = \frac{\partial^2}{\partial x^2}\left(N_y + M_y\right) + \frac{\partial^2}{\partial z^2}\left(N_y + M_y\right) - \frac{\partial}{\partial y}\left(\frac{\partial}{\partial x}\left(N_x + M_x\right) + \frac{\partial}{\partial z}\left(N_z + M_z\right) \right). \tag{2.15}$$

Considering constant fluid properties, this procedure leads to a system of four evolution equations for the variables ϕ, Ω_y, T and ρ together with the equation of state (2.3),

$$\frac{\partial \phi}{\partial t} = F(\rho, u_j) = \frac{\partial^2 N_y}{\partial x^2} + \frac{\partial^2 N_y}{\partial z^2} - \frac{\partial}{\partial y}\left(\frac{\partial N_x}{\partial x} + \frac{\partial N_z}{\partial z} \right) - \frac{1}{Re}\, \nabla^2 (\nabla \times \vec{\omega})\big|_y, \tag{2.16}$$

$$\frac{\partial \Omega_y}{\partial t} = G(\rho, u_j) = \frac{\partial N_x}{\partial z} - \frac{\partial N_z}{\partial x} + \frac{1}{Re}\left(\nabla^2 \omega_y\right), \tag{2.17}$$

$$\frac{\partial T}{\partial t} = E(\rho, u_j) = -u_i \frac{\partial T}{\partial x_i} + \frac{T}{Pe} \nabla^2 T, \tag{2.18}$$

$$\frac{\partial \rho}{\partial t} = C(\rho, u_j) = -\nabla(\rho \vec{u}) = -\nabla^2 \psi. \tag{2.19}$$

For convenience, the equations are written in dimensionless form, with the Reynolds number defined as $Re = \rho_0 \Delta U \delta_m^0 / \mu_0$ and the Peclet number as $Pe = PrRe$, with the Prandtl number defined as $Pr = \mu_0 C_p / \kappa_0$; where the subscript 0 stands for the reference values used in the non-dimensionalisation.

The manipulations to obtain eqs. (2.16-2.17) involve taking spatial derivatives of the momentum equations. In this process, information concerning the horizontally averaged

momentum vector is lost, requiring additional evolution equations to keep this information. Averaging eq. (2.5) over the homogeneous directions x and z, we obtain equations for $\langle \rho u \rangle$ and $\langle \rho w \rangle$,

$$\frac{\partial \langle \rho u \rangle}{\partial t} = -\frac{\partial \langle \rho u v \rangle}{\partial y} + \frac{\partial \langle \tau_{xy} \rangle}{\partial y}, \tag{2.20}$$

$$\frac{\partial \langle \rho w \rangle}{\partial t} = -\frac{\partial \langle \rho v w \rangle}{\partial y} + \frac{\partial \langle \tau_{zy} \rangle}{\partial y}, \tag{2.21}$$

and averaging eq. (2.1) over the homogeneous directions x and z and integrating in y we obtain an equation for $\langle \rho v \rangle$,

$$\int_{-\infty}^{y} \frac{\partial \langle \rho \rangle}{\partial t} dy = -\int_{-\infty}^{y} \frac{\partial \langle \rho v \rangle}{\partial y} dy = \langle \rho v \rangle_b - \langle \rho v \rangle(y). \tag{2.22}$$

Note that $\langle \rho u \rangle$, $\langle \rho v \rangle$ are in principle function of the vertical coordinate y and time, therefore small one-dimensional arrays to be updated every time-step.

2.2.1 Reactive case

In the reactive mixing layer case, we consider two streams of different gases: one being the oxidizer, at a temperature T_A carrying a mass fraction $Y_{O_2 A}$ of oxidizer (oxygen for example), and the other stream at temperature T_0 carrying a mass fraction Y_{F0} of a fuel. The air stream will be located on the upper side of the mixing. These two species are assumed to react in an exothermic infinitely fast chemical reaction, so that, a diffusion flame exists in the mixing layer where an amount of heat q is released per unit mass of burned fuel.

In this scenario, we have to modify the energy equation (2.18), adding the production term and consider the evolution equation of mass fraction of both species Y_O and Y_F:

$$\frac{\partial T}{\partial t} + u_i \frac{\partial T}{\partial x_i} = \frac{1}{\rho C_p} \frac{\partial}{\partial x_i} \left(\kappa \frac{\partial T}{\partial x_i} \right) + \frac{q Y_{F0}}{C_p} \dot{\omega_F}, \tag{2.23}$$

$$\frac{\partial Y_F}{\partial t} + u_i \frac{\partial Y_F}{\partial x_i} = \frac{1}{\rho} \frac{\partial}{\partial x_i} \left(D_F \frac{\partial Y_F}{\partial x_i} \right) - \dot{\omega_F}, \tag{2.24}$$

$$\frac{\partial Y_O}{\partial t} + u_i \frac{\partial Y_O}{\partial x_i} = \frac{1}{\rho} \frac{\partial}{\partial x_i} \left(D_O \frac{\partial Y_O}{\partial x_i} \right) - S \dot{\omega_F}. \tag{2.25}$$

In these equations, the chemical source term $\dot{\omega}_F$ is written in terms of the mass of fuel consumed per unit volume per unit time, D_i are the diffusivities of the different species (in particular, $D_T = \kappa/(\rho C_p)$ is the thermal diffusivity) and $S = \frac{sY_{F0}}{Y_{O_2A}}$, with s being the amount of oxygen needed to burn the unit mass of fuel. Recalling the definition of Lewis number as $L_i = D_T/D_i$, these three equations can be rewritten in terms of D_T with L_F and L_O. Finally, let us assume the oxidizer Lewis number as the unity, the typical value of air.

Thus, following [40], the problem is formulated in terms of coupling functions, including the two mixture-fraction variables

$$Z = \frac{SY_F - Y_O + 1}{S + 1}, \tag{2.26}$$

and

$$\tilde{Z} = \frac{SY_F/L_F - Y_O + 1}{S/L_F + 1}, \tag{2.27}$$

together with the excess-enthalpy variable:

$$H = \frac{T - T_A}{T_A} + \frac{\gamma(S + 1)}{S}(Y_O - 1), \tag{2.28}$$

where the definition $\gamma = \frac{qY_{F0}}{c_p T_A(1+S)}$ has been used.

After proper manipulation of equations (2.23-2.25), the system can be replaced by the evolution equation of these coupling functions, therefore removing the singularity associated with the reaction term $\dot{\omega}_F$:

$$\rho\frac{\partial Z}{\partial t} + \rho u_i\frac{\partial Z}{\partial x_i} = \frac{1}{L_m}\frac{\partial}{\partial x_i}\left[\rho D_T\frac{\partial \tilde{Z}}{\partial x_i}\right] \tag{2.29}$$

$$\rho\frac{\partial H}{\partial t} + \rho u_i\frac{\partial H}{\partial x_i} = \frac{\partial}{\partial x_i}\left(\rho D_T\frac{\partial H}{\partial x_i}\right) \tag{2.30}$$

with $L_m = (S + 1)/(S/L_F + 1)$. Equation (2.29) and (2.30) must be complemented with the chemical equilibrium condition $Y_F Y_O = 0$ for infinitely fast rate reaction, and the definitions in equations (2.26) and (2.28) to allow us to calculate Y_F, Y_O and T in terms of Z (or $\tilde{Z}$) and H. The flame is located where Y_F and Y_O are simultaneously zero, corresponding to values of the mixture fraction $Z = Z_S = 1/(S + 1)$ and $\tilde{Z}_S = 1/(S/L_F + 1)$.

For $Z \geq Z_s$:

$$\begin{aligned} Y_O &= 0 \\ Y_F &= \frac{Z - Z_S}{1 - Z_S} = \frac{\tilde{Z} - \tilde{Z}_S}{1 - \tilde{Z}_S} \\ T &= T_A \left(H + \frac{\gamma}{1 - Z_S} \right) + T_A \end{aligned} \tag{2.31}$$

For $Z \leq Z_s$:

$$\begin{aligned} Y_F &= 0 \\ Y_O &= 1 - \frac{Z}{Z_S} = 1 - \frac{\tilde{Z}}{\tilde{Z}_S} \\ T &= T_A \left(H + \frac{\gamma}{1 - Z_S} \frac{Z}{Z_S} \right) + T_A. \end{aligned} \tag{2.32}$$

Note that all these expressions replace the energy conservation equation (2.4) in the non-reactive case.

Another important change in the formulation with respect to the non-reactive one is that now we would generalize the equations considering the viscosity and the thermal diffusivity changing with temperature. In particular, we will define a power-law such

$$\frac{\mu}{\mu_A} = \frac{\rho D_T}{\rho_A D_{T_A}} = \left(\frac{T}{T_A} \right)^{\sigma} \tag{2.33}$$

With $\sigma = 0.7$ used as a good approximation of the behavior with real gases. Furthermore, we will assume $C_p = C_{p_A}$ as constant. In fact, this consideration makes much more complicated to obtain the terms involved in equations (2.12) and (2.15); note that, the terms M_i become non-linear if the viscosity depends on temperature.

It is important to note that the gradients of $\tilde{Z}$ and H are continuous at the flame surface, whereas that of Z exhibits a jump, associated with the localized chemical source. This consideration is cumbersome when solving equation (2.29). If we try to evolve equation (2.29) in terms of Z, we need to make use of the chain rule in order to write the diffusion term (with $\tilde{Z}$) in terms of Z. This approach would end up with a second derivative of a piecewise function given by (2.31) and (2.32), therefore introducing a bad conditioned function on our evolution equations. In fact, in previous versions of the code LomaHZ, we unsuccessfully

tried this approach and we had to abandon it because the resolution requirements were too high.

However, taking advantage of the continuous gradient of $\tilde{Z}$ on the surface, and that the terms involving Z on the evolution equation are just first order derivatives, we formulate the equation (2.29) in terms of $\tilde{Z}$ as

$$\rho\frac{\partial\tilde{Z}}{\partial t}+\rho u_i\frac{\partial\tilde{Z}}{\partial x_i}=\frac{d\tilde{Z}}{dZ}\frac{1}{L_m}\frac{\partial}{\partial x_i}\left(\rho D_T\frac{\partial\tilde{Z}}{\partial x_i}\right), \tag{2.34}$$

where the property $dZ/d\tilde{Z}=1/(d\tilde{Z}/dZ)$ has been used.

Summarizing, the equations to solve for the reactive case, expressed in dimensionless form are:

$$\begin{aligned}\frac{\partial\phi}{\partial t}=F'(\rho,u_j)=&\frac{\partial^2}{\partial x^2}\left(N_y+M_y\right)+\frac{\partial^2}{\partial z^2}\left(N_y+M_y\right),\\&-\frac{\partial}{\partial y}\left[\frac{\partial}{\partial x}\left(N_x+M_x\right)+\frac{\partial}{\partial z}\left(N_z+M_z\right)\right],\end{aligned} \tag{2.35}$$

$$\frac{\partial\Omega_y}{\partial t}=G'(\rho,u_j)=\frac{\partial N_x}{\partial z}-\frac{\partial N_z}{\partial x}+\frac{\partial M_x}{\partial z}-\frac{\partial M_z}{\partial x}, \tag{2.36}$$

$$\frac{\partial\tilde{Z}}{\partial t}=J(\rho,u_j)=-u_i\frac{\partial\tilde{Z}}{\partial x_i}+\frac{d\tilde{Z}}{dZ}\frac{\rho}{PeL_m}\frac{\partial}{\partial x_i}\left(T^\sigma\frac{\partial\tilde{Z}}{\partial x_i}\right), \tag{2.37}$$

$$\frac{\partial H}{\partial t}=E'(\rho,u_j)=-u_i\frac{\partial H}{\partial x_i}+\frac{\rho}{Pe}\frac{\partial}{\partial x_i}\left(T^\sigma\frac{\partial H}{\partial x_i}\right), \tag{2.38}$$

$$\frac{\partial\rho}{\partial t}=C(\rho,u_j)=-\nabla(\rho\vec{u})=-\nabla^2\psi. \tag{2.39}$$

It is important to consider that, from equations (2.32) and (2.31), not only we have the piecewise discontinuity of $d\tilde{Z}/dZ$ but also the one from the temperature definition as $T=T(\tilde{Z},H)$. In section §2.5.1, the numerical implementation of these expression will be discussed.

2.3 Temporal discretization

In most of the turbulent studies, researches use implicit solvers mostly due to the stiffness introduced by the presence of walls in the domain. However, in the problem addressed of temporal mixing layer there is no wall and, as shown in the formulation presented in the previous section, there are no linear terms involved in the right hand side of the conservation equations. For these reasons, we decided to use an explicit solver.

The algorithm implemented to solve eqs. (2.16-2.19) is split into two parts. First, we employ an explicit, low-storage, 3-stage Runge-Kutta scheme for eqs. (2.16-2.18), that for the i-th stage reads

$$\begin{aligned} \phi^i &= \phi^{i-1} + \gamma_i \Delta t F(\rho, u_j)^{i-1} + \epsilon_i \Delta t F(\rho, u_j)^{i-2}, \\ \Omega_y^i &= \Omega_y^{i-1} + \gamma_i \Delta t M(\rho, u_j)^{i-1} + \epsilon_i \Delta t M(\rho, u_j)^{i-2}, \\ T^i &= T^{i-1} + \gamma_i \Delta t E(\rho, u_j)^{i-1} + \epsilon_i \Delta t E(\rho, u_j)^{i-2}, \end{aligned} \tag{2.40}$$

where $\gamma_i = (8/15, 5/12, 3/4)$ and $\epsilon_i = (0, -17/60, -5/12)$ are the coefficients of the explicit scheme [62]. For eq. (2.19) we employ an implicit, low-storage, 3-stage Runge-Kutta scheme, that for the i-th stage reads

$$\rho^i = \rho^{i-1} - \Delta t \left(\alpha_i \nabla^2 \psi^{i-1} + \beta_i \nabla^2 \psi^i \right), \tag{2.41}$$

where $\alpha_i = (5/66, 17/15, 1/22)$ and $\beta_i = (151/330, -1, 19/66)$ are the coefficients of the implicit scheme, optimized to enhance the stability of the code in a similar way as Jang and de Bruyn Kops [32] (further details about the computation of these coefficients are given in 2.3.1).

Note that this equation is a Poisson problem for ψ^i if ρ^i is known. However, from the point of view of mass conservation, it is beneficial to express $\rho^i - \rho^{i-1}$ in terms of the temperature, and use the fact that $\nabla^2 \psi = -\partial \rho / \partial t = T^{-2} \partial T / \partial t = T^{-2} E(\rho, u_j)$, yielding

$$\nabla^2 \psi^i = \frac{1}{\beta_i \Delta t} \frac{T^i - T^{i-1}}{T^i T^{i-1}} - \frac{\alpha_i}{\beta_i} \left(\frac{E(\rho, u_j)}{T^2} \right)^{i-1}. \tag{2.42}$$

With this formulation, we are assuring that the energy equation acts as a constraint for the continuity equation (as suggested by 47), keeping both equations synchronised at every time step.

From eq. (2.40) we obtain ϕ^i, Ω_y^i and T^i. Using eq. (2.3) we obtain ρ^i, and solving the Poisson problem (2.41) we obtain ψ^i. In order to compute the right hand side of eqs. (2.16-2.18) the velocity and the vorticity are needed. The velocity is constructed as follows.

First, knowing ϕ we solve the Poisson problem eq. (2.11) to obtain m_y. Knowing Ω_y, we can solve eqs. (2.9) and (2.10) to obtain m_x and m_z. Finally, knowing ψ and ρ, from the definition, eq. (2.8), we obtain the velocity field and by derivation the vorticity field.

For the timestep computation, a Courant-Friedrichs-Lewy (CFL) condition has been implemented taking care of convective and diffusive terms.

$$\Delta t = \frac{\sigma_{CFL}}{\frac{|u|}{\Delta x} + \frac{|v|}{\Delta y} + \frac{|w|}{\Delta z} + 2\delta_D \left(\frac{1}{\Delta x^2} + \frac{1}{\Delta y^2} + \frac{1}{\Delta z^2} \right)} \tag{2.43}$$

where u, v and w are the maximum local velocities, and

$$\delta_D = \max \left(\frac{T_{\max}^{\sigma+1}}{Re}, \frac{T_{\max}^{\sigma+1}}{Pe}, \frac{T_{\max}^{\sigma+1}}{PeL_m} \right), \tag{2.44}$$

in the generalized case including combustion. Note that, the maximum temperature in the field has to be obtained for this calculation. In particular, for the non-reactive case with viscosity and thermal diffusivity not changing with temperature ($\sigma = 0$) we get $\delta_D = T^{max}/Pe$ when $Pr < 1$.

In terms of temporal discretization, the reactive code LoMaHZ is equivalent to the non-reactive case replacing the temperature evolution equation, eq. (2.4), with the conservation equations of the scalars H and $\tilde{Z}$, eqs. (2.29) and (2.30) respectively. For each sub-step, the temperature as $T = T(\tilde{Z}, H)$ is computed in order to obtain equation (2.42).

Concerning the boundary conditions, from a physical point of view the velocity and density fluctuations should tend to zero as $y \to \pm\infty$, with an additional constraint that relates the entrainment and the ambient pressure. From a computational point of view, we impose free-slip boundary conditions for the fluctuations of $\vec{m}$, homogeneous Dirichlet boundary conditions for the density fluctuations and homogeneous Neumann boundary conditions for the ψ. In terms of entrainment, the global mass balance in the system leads to one equation with two unknowns, namely the mass flux through the upper and lower boundaries of the system. A second equation is obtained imposing that the ratio of these two mass fluxes should be equal to the square root of the density ratio [19, 20]. This condition is equivalent to the one imposed by [29], matching the mass fluxes to an outer wave region where acoustic effects are important.

Namely, we impose

$$\begin{aligned} &\rho = \rho_b, \quad u = \Delta U/2, \quad w = 0 \quad \text{at } y \to -\infty, \\ &\rho = \rho_t, \quad u = -\Delta U/2, \quad w = 0 \quad \text{at } y \to \infty. \end{aligned} \tag{2.45}$$

Due to the entrainment there is a non-zero value of $\langle \rho v \rangle$ at $y \to \pm\infty$. Integrating eq. (2.22) from $-\infty$ to ∞ we obtain the total mass outflow, Φ, as

$$\Phi = \int_{-\infty}^{\infty} \frac{\partial \langle \rho \rangle}{\partial t} dy = \langle \rho v \rangle_b - \langle \rho v \rangle_t. \tag{2.46}$$

It is possible to express the total mass outflow as a function of the vertical entrainment ratio, $E_v = -\langle v \rangle_b / \langle v \rangle_t$, as

$$\Phi = \langle \rho v \rangle_b \left(1 + \frac{1}{E_v s} \right). \tag{2.47}$$

with s being the density ratio, namely ρ_b/ρ_t. Dimotakis [19] suggests that, for a variable-density temporal mixing layer, the entrainment ratio should be equal to the square root of the density ratio, an argument attributed to [9]. Using this result and computing during runtime the value of Φ we obtain $\langle \rho v \rangle_b$ from eq.(2.47) and $\langle \rho v \rangle_t = \langle \rho v \rangle_b - \Phi$.

In the reactive case, we make use of the same boundary conditions, but the entrainment condition is simplified when $T_A = T_0 = 1$ (see equation 2.47 with $s = 1$). On the other hand, instead of setting the boundary conditions for the temperature, in the reactive case we have to force the boundary values on the variables H and $\tilde{Z}$, with all values going to zero except for the mean value (00 mode). In particular: $\tilde{Z}_A = 0$, $\tilde{Z}_F = 1$, $H_A = 0$, $H_F = -\gamma/(1 - Z_S)$.

2.3.1 Consistency and stability of the new RK3 scheme

In this section, we will give the details about how the Runge-Kutta coefficients were obtained. First, the consistency of the explicit-implicit scheme (energy-continuity), will be analyzed, trying to obtain the maximum order of error while remaining stable.

We make use of the explicit parameters γ_i and ϵ_i obtained by [62], and solve the consistency equations in order to find the six parameters from the implicit part of the scheme (α_i, β_i).

The explicit part of the scheme is given by the energy equation in (2.40). This is expanded for the three sub-steps as

$$\begin{aligned}
T^{(1)} &= T^{(0)} + \Delta t \gamma_1 E(T^{(0)}) \\
T^{(2)} &= T^{(1)} + \Delta t \gamma_2 E(T^{(1)}) + \Delta t \epsilon_2 E(T^{(0)}) \\
T^{(3)} &= T^{(2)} + \Delta t \gamma_3 E(T^{(2)}) + \Delta t \epsilon_3 E(T^{(1)})
\end{aligned} \tag{2.48}$$

Where T^0 is the temperature at the beginning of the step n and T^3 is the density for the new step $n+1$.

On the other hand, the continuity equation can be expressed in terms of the temperature as

$$\frac{\partial T}{\partial t} = T^2 \nabla^2 \psi = C(T) \tag{2.49}$$

$$\begin{aligned} T^{(1)} &= T^{(0)} + \alpha_1 \Delta t C(T^{(0)}) + \beta_1 \Delta t C(T^{(1)}) \\ T^{(2)} &= T^{(1)} + \alpha_2 \Delta t C(T^{(1)}) + \beta_2 \Delta t C(T^{(2)}) \\ T^{(3)} &= T^{(2)} + \alpha_3 \Delta t C(T^{(2)}) + \beta_3 \Delta t C(T^{(3)}) \end{aligned} \tag{2.50}$$

Therefore, solving $C(T^i)$ for each substep:

$$\begin{aligned} C(T^{(1)}) &= \frac{1}{\beta_1 \Delta t} \left(T^{(1)} - T^{(0)} - \alpha_1 \Delta t C(T^{(0)}) \right) \\ C(T^{(2)}) &= \frac{1}{\beta_2 \Delta t} \left(T^{(2)} - T^{(1)} - \alpha_2 \Delta t C(T^{(1)}) \right) \\ C(T^{(3)}) &= \frac{1}{\beta_3 \Delta t} \left(T^{(3)} - T^{(2)} - \alpha_3 \Delta t C(T^{(2)}) \right) \end{aligned} \tag{2.51}$$

Now, equation (2.48) can be used in order to replace the temperature differences showed in the equation above ($T^{(i+1)} - T^{(i)}$), as they were obtained from Energy Equation. Following this procedure, we arrive to the next equations:

$$\begin{aligned} C(T^{(1)}) &= \frac{\gamma_1}{\beta_1} E(T^{(0)}) - \frac{\alpha_1}{\beta_1} C(T^{(0)}) \\ C(T^{(2)}) &= \frac{1}{\beta_2} \left(\gamma_2 E(T^{(1)}) + \epsilon_2 E(T^{(0)}) \right) - \frac{\alpha_2}{\beta_2} C(T^{(1)}) \\ C(T^{(3)}) &= \frac{1}{\beta_3} \left(\gamma_3 E(T^{(2)}) + \epsilon_3 E(T^{(1)}) \right) - \frac{\alpha_3}{\beta_3} C(T^{(2)}) \end{aligned} \tag{2.52}$$

Now we will impose that the timestep for the explicit scheme matches the implicit one. In other words:

$$\begin{aligned} \gamma_1 &= \alpha_1 + \beta_1 \\ \gamma_2 + \epsilon_2 &= \alpha_2 + \beta_2 \\ \gamma_3 + \epsilon_3 &= \alpha_3 + \beta_3 \end{aligned} \tag{2.53}$$

Substituting α_i from Eq 2.53 within equation 2.52, simplifying and considering that starting the step both functions are equivalent ($C(T^{(0)}) = E(T^{(0)})$) we get

$$\begin{aligned} C(T^{(1)}) &= E(T^{(0)}) \\ C(T^{(2)}) &= \frac{\gamma_2}{\beta_2} E(T^{(1)}) + \left(1 - \frac{\gamma_2}{\beta_2}\right) E(T^{(0)}) \\ C(T^{(3)}) &= \frac{\gamma_3}{\beta_3} E(T^{(2)}) + \left[\frac{\epsilon_3}{\beta_3} + \frac{\gamma_2}{\beta_2}\left(1 - \frac{\gamma_3 + \epsilon_3}{\beta_3}\right)\right] E(T^{(1)}) \\ &\quad + \left[\left(1 - \frac{\gamma_2}{\beta_2}\right)\left(1 - \frac{\gamma_3 + \epsilon_3}{\beta_3}\right)\right] E(T^{(0)}) \end{aligned} \tag{2.54}$$

Where we have already substitute the expresion of $C(T^{(i)})$ for the previous sub-step as expressed in equation (2.52). Thus, these are the right hand side of the continuity equation C as a function of the right hand side of the energy equation for each sub-step.

Now, writing the Taylor expansion of each $E(T^{(i)})$ and introducing them on equation (2.54), we can solve the coefficients in order to achieve first order accuracy on the scheme. Equivalently, we could make use of the *Butcher Tableau* in order to obtain these same coefficients.

For order Δt we get this equation:

$$1 = \gamma_1 \left[\frac{\epsilon_3}{\beta_3} + \frac{\gamma_2}{\beta_2}\left(1 - \frac{\gamma_3 + \epsilon_3}{\beta_3}\right)\right] + \frac{\gamma_3}{\beta_3}(\gamma_1 + \gamma_2 + \epsilon_2) \tag{2.55}$$

From order Δt, we can express the obtained equation as $\beta_3 = f(\beta_2)$, after some algebra

$$\beta_3 = \frac{\gamma_1\epsilon_3\beta_2 - \gamma_1\gamma_2\gamma_3 - \gamma_1\gamma_2\epsilon_3 + \gamma_3\beta_2(\gamma_1 + \gamma_2 + \epsilon_2)}{\beta_2 - \gamma_1\gamma_2}$$

Attention must to be paid to the value making zero the denominator $\beta_2 = \gamma_1\gamma_2$. Once the value for β_3 is fixed we can obtain α_3 from Equation 2.53: $\alpha_3 = \gamma_3 + \epsilon_3 - \beta_3$.

The second equation that we obtain is

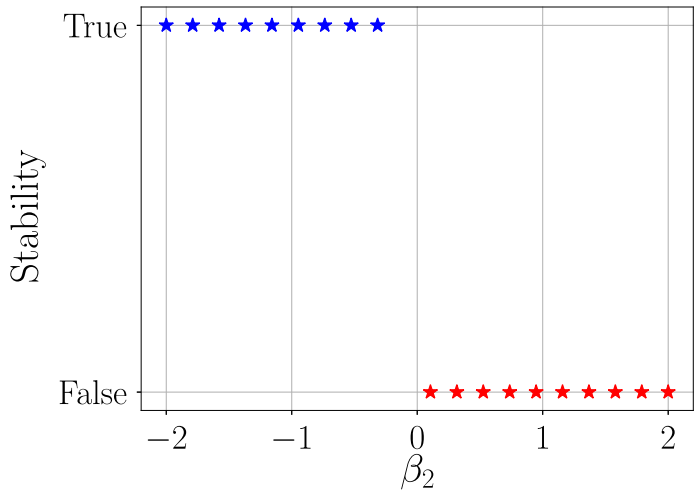

Fig. 2.2 Stability results of new RK3 scheme. Solving 1D temporal mixing layer for density ratio of 4.

$$\gamma_1(\beta_1 + \alpha_2) + (\gamma_1 + \gamma_2 + \epsilon_2)(\beta_2 + \alpha_3) + \beta_3 = 1/2 \tag{2.56}$$

All together, we have 5 equations (three from (2.53), (2.56) and (2.56)) to solve for 6 parameters. Therefore we have a *one parameter free* family of solutions to consider for stability testing.

In order to find this parameter, we need to test the stability of the scheme for different values of this free parameter β_2. Instead of solving a full 3D problem with LoMa, we solved the 1D mixing layer in order to make the calculations faster. The implementation of 1D evolution equations were done in Python using this same RK3 scheme with the same full 3D algorithm applied for the mean values, the equations are presented in appendix A. As an example, in figure 2.2, the stability results for β_2 in the range between -2 and 2 are shown for a density ratio of 4. From the results presented in figure 2.2, we chose the value of $\beta_2 = -1$. Several runs of this 1D problem were performed for different time-steps (CFL coefficients). The results of the temperature profile at the last step were compared with the self-similarity results (Self-similar solution obtained following the description from appendix A). The absolute error is shown in figure 2.3 versus the different CFL used.

Note that, using the Butcher Tableau, an additional equation for second order on the explicit part of the scheme is obtained. This second order scheme has been proved to be unstable for our problem and therefore not suitable.

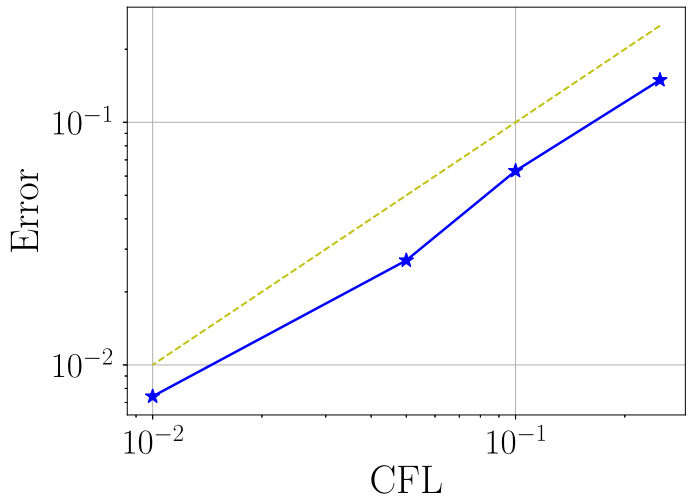

Fig. 2.3 Example of order of error of the new RK3 scheme. Results obtained evolving 1D temporal mixing layer for density ratio of 4 and comparing with the self-similar solution.

Finally, in order to make sure that this new temporal scheme works as well for the 3D case, several test were performed for an isotropic decaying turbulence box problem using Low-Mach formulation with variable density.

The simulations were performed for a 2π computational box with 96 grid points for each direction. The case of study was carried out with a density ratio (s) of 8 with a Reynolds number of 500. The simulations were initialized with a constant density case and then a cosine distribution of temperature was imposed with a maximum temperature s reached in the middle of the vertical direction.

As an example, in figure 2.4 a snapshot of one of the simulations is shown. In this plot, two iso-surfaces of $T = 1$ are represented, with color indicating the vertical position of the points. These tests proved that the scheme was also stable when considering the 3D turbulent case.

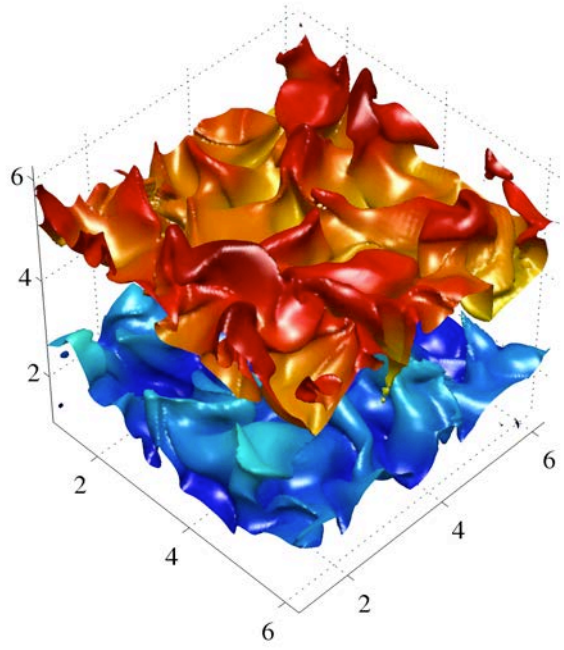

Fig. 2.4 Example of a 3D turbulent box with variable density. Iso-surfaces of $T = 1$, color scheme representing value of y-coordinate on the surfaces.

2.4 Spatial discretization

In the temporal mixing layer configuration, we have two homogeneous directions, namely streamwise (x) and spanwise (z) directions. This allow us to discretize these two directions using Fourier decomposition. Fourier space discretization have two important advantages over other approaches, as finite differences for instance. First, this method gives spectral resolution, being able to accurately resolve derivatives up to the minimum length scale discretized. Second, the linear operators involving derivatives are simplified to algebraic operations over each mode in Fourier space.

There exist two different numerical implementations of spectral methods regarding the computation of the non-linear terms. Full spectral methods (or just *spectral*), would compute these terms in Fourier space by means of convolution operations. These computations are, however, expensive in terms of computational time. A second method, called *pseudo-spectral*, would transform the field to a quadrature grid in order to perform the non-linear operations and then transform back to Fourier space. Our code uses this second approach.

One of the most important downsides of pseudo-spectral methods is aliasing. This effect refers to the distortion or artifact that results when the signal reconstructed from samples

is different from the original continuous signal. When the non-linear operations involve multiplication of two signals (or variables), it is well known that aliasing can be prevented by using the 2/3 rule [49]. Note that, due to the non-linearity appearing in the equation of state, it is not possible to completely remove aliasing errors in the present formulation. Thus, in this code we have used the 2/3 rule and assumed that some aliasing errors will appear in our computations.

For the non-homogeneous direction, namely crosswise (y), we make use of 7th and 5th order compact finite differences for first and second derivatives respectively, as in [30]. These schemes are obtained following the work of Lele [38] giving spectral-like resolution.

The solution of the Poisson equation for ψ (see section §2.5) is done in Fourier space, solving a penta-diagonal linear system for each Fourier mode with a LU decomposition.

Finally, besides the 2/3 rule already discussed, no explicit filtering is used in the present implementation.

2.5 Algorithm and implementation

In figure 2.5, an schematics of the algorithm designed is shown. White numbered rectangles represent state nodes in the code implying important transformations or calculations; orange rectangles stand for relevant outputs obtained in these transformations. A detailed explanation of this flowchart is presented in this section following the numbers.

One of the most important things to keep in mind when reading the description of this algorithm is that the code is pseudo-spectral. As explained in section §2.4, that means that all linear operations are performed in Fourier space, but the non-linear operations have to be performed in quadrature points (*physical space*). One of the main challenges in developing this algorithm was to minimize the number of buffers that have to be converted to physical space. These operations are very demanding in resources and time. Note that, before reaching the current optimized version of the algorithm, two set of transformations to physical domain and back were performed, increasing aliasing errors and computational costs.

1. Laplacian Solver ($\phi = \nabla^2 m_y$).
   Here we will obtain m_y and $\dfrac{\partial m_y}{\partial y}$ needed to calculate the rest of $\vec{m}$ components. Solving this laplacian the boundary conditions on m_y are imposed.

2. Solving for m_x and m_z.
   The system of equations to solve comes from the zero-divergence property of $\vec{m}$ (eq. 2.9) and the definition of Ω_y (eq. 2.10). Solving for m_x, m_z:

$$\begin{aligned} m_x &= \frac{ik_x}{k_x^2+k_z^2}\frac{\partial m_y}{\partial y} - \frac{ik_z}{k_x^2+k_z^2}\Omega_y \\ m_z &= \frac{ik_z}{k_x^2+k_z^2}\frac{\partial m_y}{\partial y} + \frac{ik_x}{k_x^2+k_z^2}\Omega_y \end{aligned} \tag{2.57}$$

   where the algebraich properties of the derivative on the homogeneus direction x and z have been used, i.e. multiplying by the wavenumbers ik_x and ik_z. Furthermore, in this stage we will partially evolve Ω_y, ϕ, and T, with the previous stage right hand side (RHS) terms (this corresponds to the ξ_i coefficients).

3. Obtain momentum vector $\rho\vec{u}$.
   From ψ and the already known values for m_i we get ρu_i; by construction

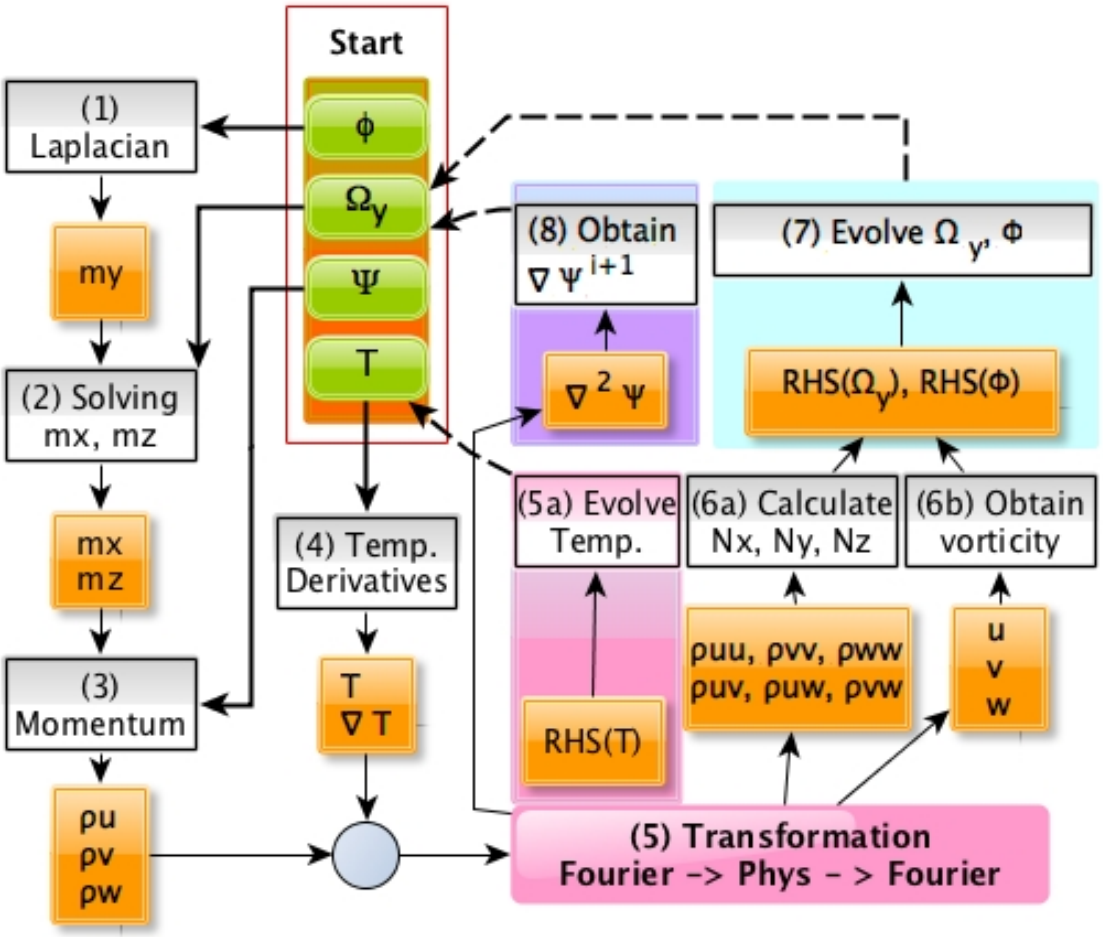

Fig. 2.5 Flowchart of LoMa code algorithm.

$$\rho u = m_x + \frac{\partial \psi}{\partial x} = m_x + ik_x\psi \tag{2.58}$$

$$\rho w = m_z + \frac{\partial \psi}{\partial z} = m_z + ik_z\psi \tag{2.59}$$

$$\rho v = m_y + \frac{\partial \psi}{\partial y} \tag{2.60}$$

Adding the ($k_x = 0, k_z = 0$) modes ($\langle \rho u \rangle$, $\langle \rho v \rangle$ and $\langle \rho w \rangle$), as explained in the formulation, we obtain the complete momentum vector.

4. Calculating derivatives of T.

   In order to calculate the nonlinear terms in physical domain, we need T, $\frac{\partial T}{\partial x_i}$ and $\nabla^2 T$, all terms using their own buffer.

5. Transforming to physical domain and back to Fourier (PHYS2FOU).

   We enter here with ρu_i, T, $\frac{\partial T}{\partial x_i}$ and $\nabla^2 T$. In order to obtain the RHS of equations (2.40), first we calculate the following terms as follow:

$$\begin{aligned} u_i &= \rho u_i T \\ \rho u_i u_j &= \rho u_i \rho u_j T \\ RHS(T) &= -u_i \frac{\partial T}{\partial x_i} + \frac{T}{Pe}\nabla^2 T \end{aligned} \tag{2.61}$$

   Note that we are using triple products in physical domain, so that, aliasing effects can occur. In this step, we also compute $\nabla\psi$ using eq. 2.42.

   (a) RHS(T) and T evolution:

   In order to improve accuracy and performance of the code, we compute and save the RHS(T,n) within physical domain, evolving using eq. (2.40).

6. Exiting PHYS2FOU

   We transform again to Fourier space a total of 11 buffers, separated in different groups following the next operations:

   (a) Convective products ($\rho u_i u_j$) (6 buffers): With these convective products, we can obtain N_j terms:

$$\begin{aligned} N_x &= -\frac{\partial \rho uu}{\partial x} - \frac{\partial \rho uv}{\partial y} - \frac{\partial \rho uw}{\partial z} \\ N_y &= -\frac{\partial \rho vu}{\partial x} - \frac{\partial \rho vv}{\partial y} - \frac{\partial \rho vw}{\partial z} \\ N_z &= -\frac{\partial \rho wu}{\partial x} - \frac{\partial \rho wv}{\partial y} - \frac{\partial \rho ww}{\partial z} \end{aligned} \tag{2.62}$$

It is important to remember saving the $(k_x = 0, k_z = 0)$ terms.

$$\begin{aligned} \langle N_x \rangle &= -\frac{\partial \langle \rho uv \rangle}{\partial y} \\ \langle N_z \rangle &= -\frac{\partial \langle \rho wv \rangle}{\partial y} \end{aligned} \tag{2.63}$$

(b) Velocity components u_i (3 buffers)

Knowing the velocity components, it is straight forward to get all components of vorticity: $\omega_x, \omega_y, \omega_z$

(c) $\nabla^2\psi$ and T(n+1) (2 buffers).

7. Compute RHS of Ω_y and ϕ and evolve.
Now we can compute RHS from eqs. (2.16) and (2.66). Similarly, we save the RHS of the $(k_x = 0, k_z = 0)$ modes evolving equations. Once this is computed, we can make use of eqs. (2.40) in order to compute the value of the variables at the next substep.

8. Obtain $\nabla^2\psi$.

From $\Delta\rho$ we can calculate the next step $\nabla^2\psi$ using eq. (2.41).

2.5.1 Reactive case (LoMaHZ).

For most of the steps, this algorithm for is similar to the one presented for LoMa. However, as discussed before, considering the viscosity and the thermal diffusivity to be a function of the temperature, complicates the computation of the RHS of ϕ, Ω_y and H-$\tilde{Z}$. On the other hand, due to the piecewise definitions used for $\tilde{Z}$ and T, we need to define a numerical strategy to smooth out the discontinuities.

Note that in Fourier space, the homogeneous derivatives (x, z) are computed multiplying by the corresponding wavenumber, without loss of accuracy if successive derivatives are taken. Nevertheless, this is not the case for y-derivatives computed using Finite Compact Differences. Therefore, in order to reduce the dispersion error we need to isolate 2nd order derivatives.

The main challenge here is that using a pseudo-spectral method, non-linear operations (like multiplying two or more variables) need to be computed in physical domain, but derivatives need to be computed on Fourier space.

Finally, as already mentioned, it is important to avoid changing to physical domain and back more than once each sub-step. This could increase aliasing errors and impact the code performance significantly.

With all these points considered, a new algorithm was designed for the reactive case formulation. First, the momentum equation (2.5) can be rewritten separating y-derivatives as,

$$\frac{\partial \rho \vec{u}}{\partial t} = \vec{A} + \frac{\partial}{\partial y}\vec{B} - \nabla p' \tag{2.64}$$

Where:

$$\begin{aligned} A_i &= -\frac{\partial}{\partial x_j}(\rho u_i u_j) + \frac{\partial \tau_{ij}}{\partial x_j};\ \text{for j} \neq 2, \\ B_i &= -\rho u_i v + \tau_{i2}. \end{aligned} \tag{2.65}$$

Following the steps described in §2.2, taking the curl of (2.64) we obtain the equation evolution for Ω_y as,

$$\frac{\partial \Omega_y}{\partial t} = \frac{\partial}{\partial z}\left(A_x + \frac{\partial B_x}{\partial y}\right) - \frac{\partial}{\partial x}\left(A_z + \frac{\partial B_z}{\partial y}\right) \tag{2.66}$$

Now we need to zoom in the y-derivative terms. Expressed in dimensionless form we can re-write the derivatives of B_x and B_z as

$$\begin{aligned}
\frac{\partial B_x}{\partial y} &= -\frac{\partial \rho u v}{\partial y} + \frac{1}{Re}\frac{\partial}{\partial y}\left(T^\sigma \frac{\partial u}{\partial y} + T^\sigma \frac{\partial v}{\partial x}\right) = -\frac{\partial \rho u v}{\partial y} + \frac{1}{Re}\frac{\partial}{\partial y}\left(\tau_{12}\right), \\
\frac{\partial B_z}{\partial y} &= -\frac{\partial \rho w v}{\partial y} + \frac{1}{Re}\frac{\partial}{\partial y}\left(T^\sigma \frac{\partial w}{\partial y} + T^\sigma \frac{\partial v}{\partial z}\right) = -\frac{\partial \rho w v}{\partial y} + \frac{1}{Re}\frac{\partial}{\partial y}\left(\tau_{32}\right).
\end{aligned} \tag{2.67}$$

Recall that we enter FOU2PHYS with ρu_i and not with u_i. Making use of the chain rule, we can express the velocity derivatives (first and second) in terms of the known terms

$$\begin{aligned}
\frac{\partial u_i}{\partial x_j} &= T\frac{\partial(\rho u_i)}{\partial x_j} + \rho u_i \frac{\partial T}{\partial x_j} \\
\frac{\partial^2 u_i}{\partial x_j^2} &= T\frac{\partial^2(\rho u_i)}{\partial x_j^2} + 2\frac{\partial(\rho u_i)}{\partial x_j}\frac{\partial T}{\partial x_j} + \rho u_i \frac{\partial^2 T}{\partial x_j^2}, \\
T^\sigma \frac{\partial u_i}{\partial x_j} &= \frac{\partial\left(T^\sigma u_i\right)}{\partial x_j} - \sigma u_i T^{\sigma-1}\frac{\partial T}{\partial x_j}.
\end{aligned} \tag{2.68}$$

Using these relations we can express the viscous tensor as

$$\tau_{ij} = T^\sigma \frac{\partial u_j}{\partial x_i} + T^\sigma \frac{\partial u_i}{\partial x_j} = \underbrace{\frac{\partial(T^\sigma u_i)}{\partial x_j} + \frac{\partial(T^\sigma u_j)}{\partial x_i}}_{\tau_{ij}^A} \underbrace{- \sigma T^\sigma \left(\rho u_i \frac{\partial T}{\partial x_j} + \rho u_j \frac{\partial T}{\partial x_i}\right)}_{\tau_{ij}^B} = \tau_{ij}^A - \tau_{ij}^B \tag{2.69}$$

For example, in the case of the tensor components involving y-derivatives, they can be expressed explicitly in terms of second y-derivatives, namely

$$\frac{\partial}{\partial y}\left(\tau_{i2}\right) = \frac{\partial}{\partial y}\left(T^\sigma \frac{\partial v}{\partial x_i} + T^\sigma \frac{\partial u_i}{\partial y}\right) = \frac{\partial \tau_{i2}^A}{\partial y} - \frac{\partial \tau_{i2}^B}{\partial y} \tag{2.70}$$

with

$$\frac{\partial \tau_{i2}^A}{\partial y} = \frac{\partial^2}{\partial y^2}\left(T^\sigma u_i\right) + \frac{\partial}{\partial y}\left(\frac{\partial\left(T^\sigma v\right)}{\partial x_i}\right) \tag{2.71}$$

$$\frac{\partial \tau_{i2}^B}{\partial y} = \frac{\partial}{\partial y}\left(\sigma T^\sigma \rho u_i \frac{\partial T}{\partial y}\right) + \frac{\partial}{\partial y}\left(\sigma T^\sigma \rho v \frac{\partial T}{\partial x_i}\right) \tag{2.72}$$

So that, we can explicitly obtain the 2nd-order y-derivative terms, with a unique Fourier-Physical-Fourier transformation per sub-step.

In order to obtain the ϕ equation we would make use of the mathematical identity

$$\nabla \times \left(\nabla \times \vec{Q} \right) = \nabla \left(\nabla . \vec{Q} \right) - \nabla^2 \vec{Q}, \tag{2.73}$$

taking now the curl of equation (2.66) together with this identity, we get

$$\frac{\partial \phi}{\partial t} = \left(\frac{\partial^2}{\partial x^2} + \frac{\partial^2}{\partial z^2} \right) \left(A_y + \frac{\partial B_y}{\partial y} \right) - \frac{\partial}{\partial x} \frac{\partial}{\partial y} \left(A_x + \frac{\partial B_x}{\partial y} \right) - \frac{\partial}{\partial z} \frac{\partial}{\partial y} \left(A_z + \frac{\partial B_z}{\partial y} \right), \tag{2.74}$$

and arranging the terms by y-derivative order we get,

$$\frac{\partial \phi}{\partial t} = \left(\frac{\partial^2}{\partial x^2} + \frac{\partial^2}{\partial z^2} \right) \left(A_y + \frac{\partial B_y}{\partial y} \right) - \frac{\partial}{\partial y} \left(\frac{\partial A_x}{\partial x} + \frac{\partial A_z}{\partial z} \right) - \frac{\partial}{\partial x} \frac{\partial^2 B_x}{\partial y^2} - \frac{\partial}{\partial z} \frac{\partial^2 B_z}{\partial y^2}. \tag{2.75}$$

Once we have introduced this new arrangement, it is straight forward to follow the algorithm similarly to the one described before for the non-reactive case.

Piecewise functions implementation

One important challenge to face when numerically integrating equations (2.37), (2.38) together with the piecewise definitions presented in (2.31) and (2.32) is the jump on the derivatives of these expressions.

First of all, in order to use a continuous function implemention (thus avoiding *if clauses*) for this piecewise definition, we need to define an analytical function replacing the *step function* (also called *Heaviside function*). For instance, the partial derivative of T with respect of $\tilde{Z}$ can be written as

$$\frac{\partial T}{\partial \tilde{Z}} = \frac{\gamma}{(1 - Z_S)\tilde{Z}_S} \Xi(\tilde{Z}_S - \tilde{Z}). \tag{2.76}$$

Note that T is continuous in H; the discontinuity of the temperature derivative with respect to $\tilde{Z}$ at the flame surface ($\tilde{Z} = \tilde{Z}_S$) can be smooth out replacing $\Xi(x)$ by $\Xi_\beta(x) = \frac{1}{2}(\tanh(\beta x) + 1)$. This approximation amounts to assigning a finite thickness to the flame, measured by β^{-1}, as explained by [29]. They found that their results did not depend on β provided it was sufficiently large for the transport effects to dominate in the scale of this artificial thickness. A typical value of $\beta = 50$ is found for turbulent calculations in [51]. So that, we can explicitly

write this approximation as

$$\frac{\partial T}{\partial \tilde{Z}} = \frac{\gamma}{(1-Z_S)\tilde{Z}_S}\Xi(\tilde{Z}_S - \tilde{Z}) = \frac{\gamma}{(1-Z_S)\tilde{Z}_S}\frac{1}{2}\left(\tanh(\beta(\tilde{Z}_S - \tilde{Z})) + 1\right). \quad (2.77)$$

In order to avoid spurious temperature values, we need to be consistent on our definition of T, hence we will need to integrate (2.77) in order to obtain a new analytical expression for $T = T(\tilde{Z}, H, \beta)$, namely

$$T = 1 + H + \frac{\gamma}{(1-Z_S)\tilde{Z}_S 2\beta}\left[\beta\tilde{Z} - \ln(\cosh(\beta(\tilde{Z}_S - \tilde{Z}))) + \ln(\cosh(\beta\tilde{Z}_S))\right] + C \quad (2.78)$$

Where the constant C can be obtained from the boundary conditions at the top, where $T = T_A$ and $Z = \tilde{Z} = H = 0$. So that, we obtain $C = 0$ for the case under consideration. Analogously, this same method can be implemented for $d\tilde{Z}/dZ$.

This implementation was used in previous versions of the code. However, one of the main focus on this thesis is the flame temperature characterization for different values of S. It turns out that for moderately large values of S ($S > 4$) this approximation could significantly affect the flame temperature description.

In figure 2.6, as an example, temperature profiles as a function of $\tilde{Z}$ are presented for different values of S with $L_F = 0.3$ and $\gamma = 4$. Here, a simple relation $\tilde{Z} = 0.5(\tanh(y/2)+1)$ and $H = H_F 0.5(\tanh(y/2) + 1)$ is assumed, with y being the crosswise coordinate. With dashed lines, we represent the results for $\beta = 100$ (twice larger than the reference value of $\beta = 50$). Continuous lines are obtained using a different approach allowing sharper gradients and therefore more accurate results of the temperature near the flame. Vertical dotted lines are used in figure 2.6 to highlight the flame location. In all cases of S depicted in the figure, we observe that both approaches give the same result for all $\tilde{Z}$ except for the temperature at the flame. In particular, for $S = 15$, we can see that this model would predict a flame temperature about a 10% lower than the real one, and would predict regions with higher temperatures than the temperature at the flame.

On the other hand, expression (2.78) ceases to be valid for values of $\beta \gtrsim 200$ (limit depending on S) due to the logarithm expressions involved. Therefore there exist a maximum *sharpness* that we can implement using that method.

For the turbulent flows studied in this research it is important to accurately predict temperatures at the flame. Thus, we needed a different approach with more aggressive gradient definitions. We will make use of the tanh expressions for the Heaviside function approximation, but instead of approximating the temperature derivative, we will approximate the temperature itself.

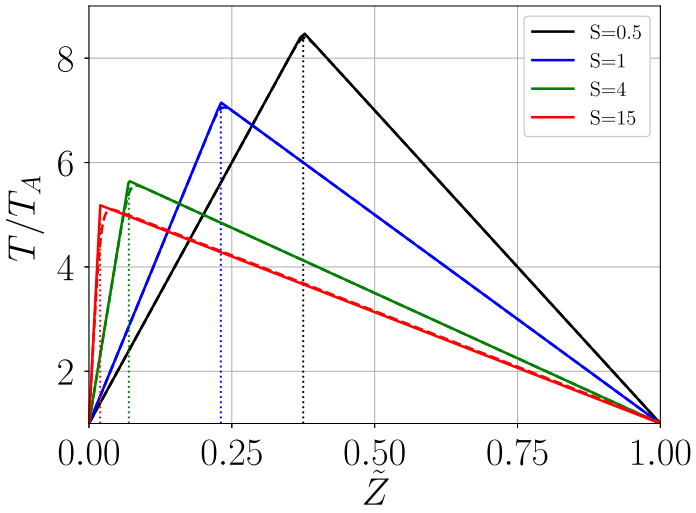

Fig. 2.6 Toy model for $T = T(\tilde{Z})$ for different values of S with $L_F = 0.3$ and $\gamma = 4$. Dashed lines for high dumping and continuous lines for present approach.

Explicitely, we define T as

$$T = 1 + H + \frac{\gamma}{(1 - Z_S)} \frac{\tilde{Z}}{\tilde{Z}_S} \Xi(\tilde{Z}_S - \tilde{Z}) + \frac{\gamma}{1 - Z_S} \Xi(\tilde{Z} - \tilde{Z}_S) \tag{2.79}$$

with $\Xi(x) = 0.5(\tanh(\beta x) + 1)$. Differentiating this expression, we obtain

$$\frac{dT}{d\tilde{Z}} = \frac{\gamma}{(1 - Z_S)\tilde{Z}_S} \Xi(\tilde{Z}_S - \tilde{Z}) - \frac{\gamma}{(1 - Z_S)} \frac{\tilde{Z}}{\tilde{Z}_S} \Xi'(\tilde{Z}_S - \tilde{Z}) + \frac{\gamma}{(1 - Z_S)} \Xi'(\tilde{Z} - \tilde{Z}_S), \tag{2.80}$$

with $\Xi'(x) = 0.5\beta(1 - \tanh(\beta x)^2)$.

With this approach, the valid range for the constant β varies from 1000 to 10^5. We performed several tests for 1D reactive mixing layers stability analysis using the two piecewise approximation methods (using $\beta = 50$ for the first approach and $\beta = 10^5$ for the second one). Both methods gave the same results, therefore proving the validity of this new piecewise implementation.

Finally, note that for the temperature gradient computation we would make use of the chain rule, namely

$$\frac{\partial T}{\partial x_i} = \frac{\partial H}{\partial x_i} + \frac{dT}{d\tilde{Z}} \frac{\partial \tilde{Z}}{\partial x_i} \tag{2.81}$$

Algorithm

This algorithm is based on the one described for non-reactive mixing layers and therefore details are skipped in order to avoid repetition.

1. Laplacian Solver ($\phi = \nabla^2 m_y$).
2. Solving for m_x and m_z.
3. Obtaining momentum vector $\rho\vec{u}$.
4. Calculating derivatives of H and $\tilde{Z}$,
   Now, we compute the gradient components and laplacian of H and $\tilde{Z}$.
5. Transforming to physical space and back to Fourier
   Similar to the non-reactive algorithm, we now transform the variables to physical space, including the derivatives and laplacian of $\tilde{Z}$. Note that the variable H is somehow substituting the T in the non-reactive implementation. In this stage, we compute RHS(H) and RHS($\tilde{Z}$), evolving both magnitudes in physical domain.
6. Exiting PHYS2FOU
   In this case, we have to transform up to 18 buffers grouped as follows:
   (a) $H(n+1)$, $\tilde{Z}(n+1)$ (2 buffers)
   (b) Convective products ($\rho u_i u_j$) (6 buffers)
   (c) Diffusive terms for τ_{ij} computation (9 buffers) The terms τ_{ij}^A and τ_{ij}^B are computed.
   (d) $\nabla^2\psi$ (1 buffer)
7. Compute RHS of Ω_y and ϕ and evolve.
8. Obtain $\nabla^2\psi$.

2.6 Performance

Both LoMa and LoMaHZ are highly scalable parallel code, ready to efficiently work with a very high number of processors. The most important reason behind this scalability and performance is the conversion from planes when working on Fourier space to lines when calculating operations in physical domain. This feature is a heritage from their predecessor, the Channel code from UPV Madrid ([30]), and therefore we will not focus on the details behind.

However, changing from a constant density formulation to a Low-Mach variable density formulation, implied many complications arising in terms of number of operations, buffer efficiency and complexity of the formulation. In particular, one of the most important challenges in terms of numerical efficiency was to maintain one transformation from Fourier to physical space per sub-step.

The algorithm and implementation explained in the previous sections of the chapter, allowed LoMa and LoMaHZ to remain efficient and highly scalable as shown in figure 2.7. In this figure, the computational time per step in seconds is shown for different simulations

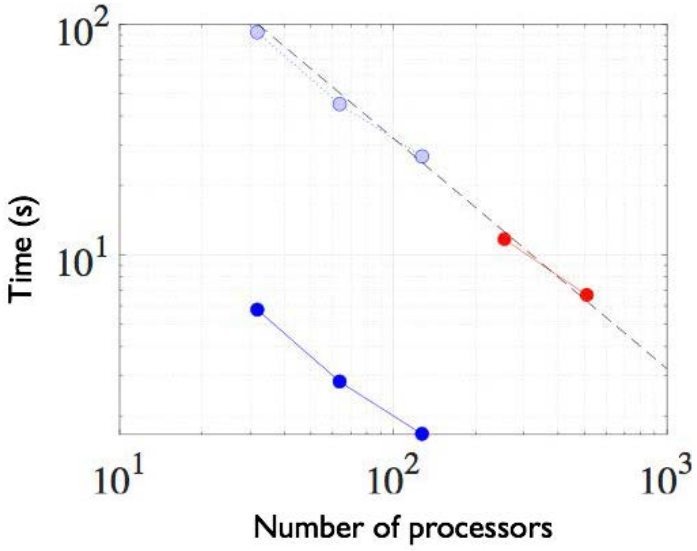

Fig. 2.7 Scaling of LoMa code. Blue dots for simulations performed on Icaro with $2 \cdot 10^7$ grid points, red dots show results from simulations performed on Comet(XSEDE) with $35 \cdot 10^7$ grid points. Grey dots belong to the projection from Icaro results multiplied by a factor of 16.

performed on Icaro and Comet with different number of grid points. In this figure we can see how the time per step is reduced with increasing number of processors with a given parallel efficiency above 90%. The grey dots on fig. 2.7 are obtained by multiplying by a factor of

16 the times obtained from Icaro (simulations performed with a relative small number of processors).

Chapter 3

Non-reactive turbulent mixing layers with variable density

3.1 Introduction

Variable density effects in turbulent flows are often encountered in the natural environment and in many engineering applications [13, 66]. In the oceans, density variations are due to temperature and salinity variations [65], while in the atmosphere they are due to both temperature and moisture changes [71]. In both situations, the buoyancy effects are mainly due to gravity. In absence of gravity, density effects may still be important due to pressure and/or temperature fluctuations. For example in aeronautical applications, density variations due to high speed in gas flows are very relevant [39, 26]. In that case, the main effect is due to velocity induced pressure variations. In other applications, density variations due to dilatation effects are important even at low speeds. This is for example the case in combustion applications [70, 53], where the heat release by chemical reaction leads to the thermal expansion of the fluid. An additional kind of density effect is associated with the mixing of two non-reactive fluids of different density or to the mixing of different temperature bodies of the same fluid [13, 21]. In this work we are concerned with the latter since we study a variable-density low-speed temporal turbulent mixing layer in the absence of gravity.

As reviewed by [19], in spatially-developing turbulent shear layers the density ratio influences the spreading rate of the layer, the entrainment rate and the convective velocity of the large-scale eddies. The influence on the spreading rate was already observed in early experiments [10]. However, the effect of increasing the Mach number, M, was found to be more drastic and that led to a main focus on compressibility effects in subsequent works [7, 52, 15, 27, 67, 41, 48, 31]. A notable exception is the work of [50] who studied both

compressibility effects and density ratio effects in direct numerical simulations of turbulent compressible temporal mixing layers. They found that, with increasing density ratio, the shear layer growth rate decreases substantially and that the dividing streamline is shifted towards the low-density stream. The variation of the density ratio by [50] was performed at high speed, with a convective Mach number $M_c = 0.7$, so that density variations due to both pressure effects and temperature effects were likely to affect the flow. In this work we try to separate these two effects by considering a variable-density layer at low speed in the limit $M_c \to 0$, using the low Mach number approximation [44, 16, 47].

The current understanding of the effect of the density ratio on the structure of the turbulent mixing layer is still unsatisfactory. Part of the problem is that it is difficult to perform experiments at low speeds with a large density ratio. Numerical studies are also scarce and most of them deal with the initial stages of transition to turbulence, and not with the turbulent regime itself. Most numerical studies consider variable density effects in the limit of incompressible flow, i.e. the velocity field is solenoidal, the density is given by an advection equation and the energy equation is therefore decoupled from the momentum equation. For instance, [37] reported calculations of a variable-density, incompressible, temporal mixing layer. They performed visualizations of the vorticity and scalar fields and of the motion of material surfaces, focusing on the manifestation of three dimensional instabilities. They found an asymmetric entrainment pattern favouring the low-density stream. Also in the incompressible regime, [61] performed two-dimensional simulations of spatially-developing variable-density mixing layers. They found that the speed of the unstable waves is biased toward that of the high-density stream and also that the entrainment of the high-density stream is inhibited relative to the low-density stream. The instability characteristics of variable-density incompressible mixing layers have been studied by [57] and [25]. On the modelling side, [56] developed a simple model for predicting the thickness of a variable-density mixing layer. [3] included variable-density effects in a one-dimensional turbulence approach. Using this approach they studied both temporally-developing and spatially-developing mixing layers, and despite the limitations of the approach, their results provide information concerning the expected behaviour of the mixing layers at high density ratios. In addition, there are also not so many studies in the literature using Large Eddy Simulation (LES) in variable density turbulent flows. Some examples are Wang et al. [69], who analyzed spatially developing axisymmetric jets, and McMullan et al. [43], who considered a spatially developing mixing layer.

In this chapter, we address the following issues. How is the growth rate of the turbulent mixing layers affected by the free-stream density ratio? What is the turbulent structure of variable-density mixing layers? What are the differences of the low speed case, $M \to 0$,

with respect to the high speed case, $M_c = 0.7$, [50]? The manuscript is organized as follows. In §3.2 the computational setup is described including the details of a novel algorithm developed to solve the low Mach number approximation of the Navier-Stokes equations. This is followed by a description of the simulation parameters in §3.3. Results are presented in §3.4. First, we analyze the self-similar evolution of the mixing layers. Secondly, we characterize their growth rate and compare to a model proposed in the literature. Third, we analyze the mean density and Favre averaged velocity, and propose a semi-empirical model for the observed shifting. After this, we complete the characterization of the vertical profiles with mean temperature. This is followed in §3.4.4 by the analysis of the higher order statistics. Section §3.4 finalizes with the analysis of the flow structures, using flow visualizations and premultiplied spectra of temperature and velocity. Conclusions are provided in §3.5.

3.2 Computational Setup

The flow under consideration is a three-dimensional, temporally-evolving mixing layer developing between two streams of different density, ρ_t (upper stream) and ρ_b (lower stream). The flow is assumed to be homogeneous in the horizontal directions, x and z, while it is inhomogeneous in the vertical direction, y. The lower stream flows at a velocity $\Delta U/2$ in the positive x direction, while the upper stream flows at a velocity $\Delta U/2$ in the oposite direction, so that the velocity difference between both streams is ΔU. For the present work, $\rho_b > \rho_t$, although since we do not consider gravity effects, the case with $\rho_b < \rho_t$ can be obtained by changing the direction of the y-axis.

The details of the algorithm used to integrate in time this coupled system of equations is described detail in Chapter 2. For completeness, we provide here a brief description. The time integration is performed using a three-stage low-storage Runge-Kutta scheme. Initial conditions are provided specifying the mean streamwise velocity and density profiles

$$\overline{u}(y) = \frac{\Delta U}{2} \tanh\left(-\frac{y}{2\delta_m^0}\right), \tag{3.1}$$

$$\overline{\rho}(y) = \rho_0 \left(1 + \lambda(s) \tanh\left(-\frac{y}{2\delta_m^0}\right)\right), \tag{3.2}$$

where $\lambda(s) = (\rho_b - \rho_t)/(\rho_b + \rho_t) = (s-1)/(s+1)$. The mean spanwise and vertical velocity components are set to zero. In order to promote a quick transition to turbulence, random velocity fluctuations are added. This is done in a manner similar to Pantano and Sarkar [50], da Silva and Pereira [17] and others: a random solenoidal velocity fluctuation field with a 10% turbulence intensity and a peak wavenumber of $k_0\delta_m^0 \approx 0.84$. The region in space were the fluctuating velocity field is defined is limited by a gaussian filter, $e^{-\left(y/\delta_m^0\right)^2}$. Also, no fluctuations are imposed on wavenumbers smaller than $k_x\delta_m \approx 0.05$, so that the initial transient of the mixing layer is as *natural* as possible, as discussed by da Silva and Pereira [17].

It should be noted that in the previous paragraphs we have been using δ_m^0 to denote the initial value of the momentum thickness δ_m. For a variable density boundary layer the momentum thickness is defined as

$$\delta_m(t) = \frac{1}{\rho_0 \Delta U^2} \int_{-\infty}^{\infty} \overline{\rho} \left(\frac{1}{2}\Delta U - \tilde{u}\right)\left(\frac{1}{2}\Delta U + \tilde{u}\right) dy, \tag{3.3}$$

where $\tilde{u} = \overline{\rho u}/\overline{\rho}$ denotes the Favre average of u, and $\overline{u}$ is the standard Reynolds average (i.e., averaged over the homogeneous directions and over the different runs performed for each

density ratio). The Favre perturbations are defined as $u'' = u - \tilde{u}$, so that the turbulent stress tensor, R_{ij}, is defined as

$$R_{ij} = \frac{\overline{\rho u_i'' u_j''}}{\overline{\rho}}. \tag{3.4}$$

For completeness, we also provide here the definition of the vorticity thickness

$$\delta_w(t) = \frac{\Delta U}{|\partial \tilde{u}/\partial y|_{max}}, \tag{3.5}$$

which is similar to the *visual* thickness of the mixing layer (see 56, 10, 20 and experimental works in general), and it will be used in the discussion of the results in the following sections.

3.3 Simulation Parameters

As mentioned above, the set-up of the simulations consists of a three-dimensional temporally-evolving mixing layer with two streams with different density. A total of four density ratio cases have been studied in this work, namely $s = \rho_b/\rho_t = 1$, 2, 4 and 8. Four different realizations have been run for each density ratio (with different random initial conditions, discussed below), in order to perform ensemble averaging. For the case with $s = 1$, the temperature is treated as a passive scalar: density is constant in time and space, and the energy equation is solved for the temperature disregarding the equation of state. The Reynolds and Prandtl numbers are fixed for all cases, with $Re = 160$ and $Pr = 0.7$. The value of other relevant parameters are presented in Table 3.1. For instance, the Reynolds number based on the Taylor micro-scale, Re_λ, is moderately large for the $s = 1$ case ($Re_\lambda = 150$), although it decreases with the density ratio ($Re_\lambda = 95$ for $s = 8$).

In terms of temporal resolution, all simulations presented here are run with a $CFL = 0.5$. The computational domain is $L_x \times L_y \times L_z = 461\delta_m^0 \times 368\delta_m^0 \times 173\delta_m^0$, roughly twice larger in every direction than that employed by Pantano and Sarkar [50]. The plane $y = 0$ is at the center of the computational domain, so that the upper and lower vertical boundaries are at $y = \pm L_y/2 = 184\delta_m^0$. The computational domain is discretized using $1536 \times 851 \times 576$ collocation grid points, resulting in a spatial resolution in the homogeneous directions of $\Delta x = \Delta z = 0.30\delta_m^0$ before dealiasing (collocation points). In the vertical direction, the grid points are equispaced in the central part of the domain ($|y| \leq 20\delta_m^0$), with a resolution $\Delta y = 0.2\delta_m^0$. In the region $20\delta_m^0 \leq |y| \leq 150\delta_m^0$ the resolution increases with a maximum stretching of 1%, up to a maximum grid spacing of $\Delta y = 0.85\delta_m^0$. Finally, in order to avoid numerical issues in the calculation of the vertical derivatives at the boundaries, the grid spacing is reduced again in the region $150\delta_m^0 \leq |y| \leq 184\delta_m^0$ with a maximum stretching of 3%, resulting in a resolution of $\Delta y = 0.3\delta_m^0$ at the top and bottom boundaries of the computational domain.

As shown in Table 3.1, the resolution of the simulations is very good in terms of the local Kolmogorov lengthscale η (i.e., averaged in horizontal planes only). The horizontal grid spacing is smaller than 1.8η during the self-similar evolution of the mixing layer. The vertical resolution is slightly better, to account for the worse resolution properties of compact finite differences compared to Fourier expansions [38]. For reference, the resolution in the compressible simulations of Pantano and Sarkar [50] is $\Delta x/\eta \approx 3-4$. Compared to typical resolution of DNS of incompressible flows, the values of the resolution reported in Table 3.1 would indicate that our simulations are slightly over-resolved (e.g, 46 recomends $\Delta x = 8\eta$ in the streamwise direction, and $\Delta y = 4\eta$ in the shear-wise direction for homogeneous shear turbulence). However, it should be noted that the non-linear terms of equations (2.16)-(2.19)

s	τ_0 - τ_f	Re_w	Re_λ	$(\Delta x/\eta)_{\max}$	$(\Delta y/\eta)_{\max}$	D_w
1	380-520	4200-6300	140-150	1.7-1.6	1.1 - 1.05	4.8
2	400-520	4500-5800	130-140	1.6-1.5	1.05 - 0.95	5.2
4	440-620	4500-6500	110-120	1.4-1.3	0.9 - 0.8	6.1
8	550-730	4900-7000	85-95	1.2-0.9	0.7 - 0.6	7.7

Table 3.1 Relevant parameters of the simulations within self-similar period. All the ranges correspond to the values of the parameter at the beginning ($\tau = \tau_0$) and end ($\tau = \tau_f$) of the self-similar evolution, discussed in section 3.4.1. $Re_w = \rho_0 \Delta U \delta_w / \mu$, where δ_w is the vorticity thickness. $Re_\lambda = q\lambda/\nu$, where λ is the Taylor microscale and q^2 is twice the turbulent kinetic energy. Δx and Δy are the streamwise and vertical grid spacings in collocation points, respectively. η is the Kolmogorov lengthscale. $D_w = \delta_w/\delta_m$, where δ_m is the momentum thickness and δ_w is the vorticity thickness.

are not quadratic, resulting in stronger aliasing and stricter limitations in the resolution than typically encountered in incompressible flows.

Finally, it should be noted that the use of relatively large computational domains is motivated by two reasons, fidelity of the turbulent structures in the mixing layer and statistical convergence. First, a large domain in the y-direction allows the mixing layer to grow for longer times before confinement effects develop, resulting in a longer self-similar range. In the present simulations, the visual thickness of the mixing layer at the end of the self-similar range is smaller than 30% of the vertical size of the computational domain. Second, the horizontal size of the domain also needs to be large enough to capture the largest structures of the flow. For reference, in our simulations less than 6% of the turbulent kinetic energy is contained in infinitely large modes in the streamwise ($k_x = 0$) and spanwise ($k_z = 0$) directions at the end of the self-similar range, when the turbulence structures are largest. As discussed later in section 3.4.5, this percentage is a little bit larger for the temperature variance ($\approx 15\%$), which tends to have a stronger signature in $k_z = 0$ modes than the turbulent kinetic energy. Also, in order to improve the statistical convergence, the horizontal averaging is complemented with an ensemble average over the four independent runs (i.e., with different initial conditions) performed for each density ratio.

3.4 Results

3.4.1 Self-similar evolution

It is well known that temporal mixing layers reach a self-similar evolution after an initial transient, in which the initial perturbations evolve into the structure of the fully developed turbulent mixing layer [58, 50]. In the self-similar evolution, the mixing layer thickness grows linearly with time, and large-scale quantities scaled with the variation across the mixing layer (i.e., ΔU, $\rho_b - \rho_t$, etc.) collapse into a single profile when plotted as a function of $y/\delta_m(t)$ or $y/\delta_\omega(t)$.

In order to evaluate the self-similar evolution of the present DNS results, figure 3.1(a) shows the evolution of $\delta_m(t)$ for the four cases considered here. The variability in δ_m is estimated using the standard deviation of the momentum thicknesses over the four runs, and is indicated with error-bars in the figure. Also, figure 3.1(b) shows the time evolution of the integrated dissipation rate of turbulent kinetic energy

$$\zeta = \int_{-\infty}^{\infty} \overline{\epsilon} dy. \tag{3.6}$$

The quantity ζ scales with ΔU^3 and, therefore, should be constant with time, once self-similarity has been achieved. The expression for the dissipation rate of turbulent kinetic energy for variable density flows can be found in [13], and is reproduced here for completeness

$$\overline{\rho}\,\overline{\epsilon} = \frac{4}{3}\mu\overline{\theta'^2} + \mu\overline{\omega_i'\omega_i'} + 2\mu\left(\frac{\partial^2\overline{u_i'u_j'}}{\partial x_i \partial x_j} - 2\frac{\partial\overline{\theta' u_j'}}{\partial x_j}\right), \tag{3.7}$$

where primed variables denote fluctuations with respect to the mean, $\theta = \partial u_i/\partial x_i$ is the divergence of the velocity, and ω_i are the components of the vorticity.

The results presented in figure 3.1 show that self-similarity is achieved after an initial transient, with $\delta_m(t)$ growing linearly with time and $\zeta(t)$ becoming approximately constant (at least within the errors in ζ). However, comparing figures 3.1(a) and 3.1(b) it can be observed that the linear growth of δ_m starts at $\tau = t\Delta U/\delta_m^0 \approx 200$, a time at which ζ is still growing. This behavior was also observed by [58], and it indicates that the determination of the time interval where self-similarity is achieved needs a careful consideration, and should not be determined exclusively from a linear evolution of $\delta_m(t)$.

In the present study, and for the purpose of collecting statistics, we have defined the time interval $[\tau_0, \tau_f]$ where the mixing layer is self-similar by analyzing the collapse of the instantaneous (i.e., averaged in the horizontal directions only) profiles of the normal Reynolds

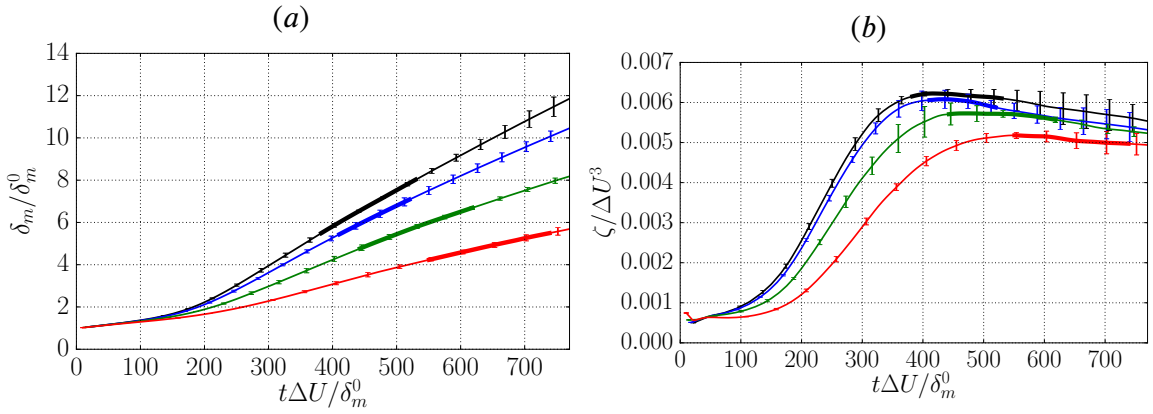

Fig. 3.1 Temporal evolution of (*a*) the momentum thickness δ_m divided by the initial momentum thickness δ_m^0, and (*b*) the non-dimensional integrated turbulent energy dissipation rate, $\zeta/\Delta U^3$. Line types are black for $s = 1.0$, blue for $s = 2.0$, green for $s = 4.0$ and red for $s = 8$. The values correspond to the ensemble average of the 4 runs for each density ratio, and the error bars are the corresponding standard deviation. The thick line shows the ranges of self-similar evolution for each density ratio.

stresses, $R_{11}(y/\delta_m, \tau)$, $R_{22}(y/\delta_m, \tau)$, and $R_{33}(y/\delta_m, \tau)$. We have computed the temporal mean and standard deviation of these Reynolds stresses for several time intervals, selecting for each run the longest time interval in which the standard deviation of the normal Reynolds stresses is smaller than 5% of the maximum. The resulting time intervals (more explicitly, the maximal time interval over the four runs for each density ratio) are shown in figure 3.1 and reported in table 3.1, yielding a total self-similar range of at least 10 eddy-turnover times per density ratio. For illustration, figure 3.2 shows all the R_{11} profiles within the self-similar range for the cases $s = 1$ and $s = 4$, using different color for each run. The agreement of the profiles is good, especially taking into account that there are 26 and 31 curves on each plot, respectively. The differences are more apparent near the maximum of the Reynolds stresses. It is interesting to note that the variability of the profiles within each run is small, similar to that reported by [50]. On the other hand, the variability between different runs is a bit larger, and it is probably linked to differences between the largest structures developed in each run (i.e., by different realizations of the initial conditions), emphasizing the importance of running several realizations of each density ratio to accumulate statistics for the largest structures in the mixing layer.

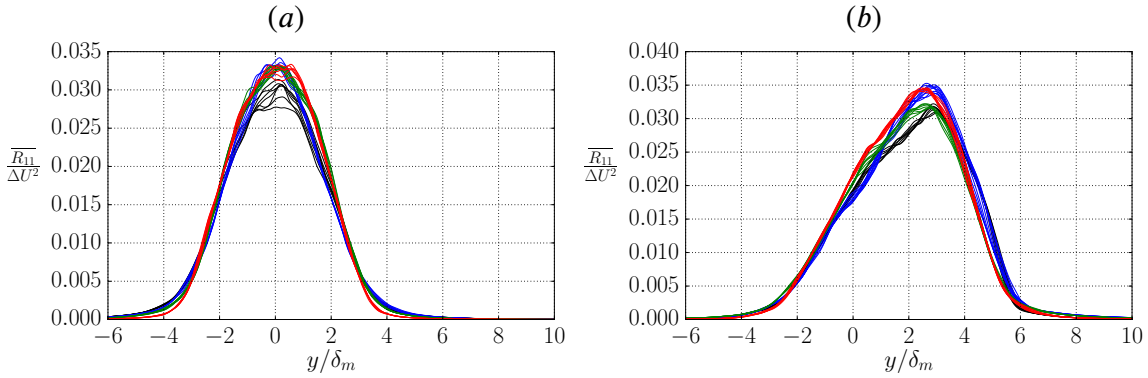

Fig. 3.2 Reynolds stress R_{11} profiles within the self-similar range for (a) case $s = 1$, all runs with a total of 26 profiles, and (b) case $s = 4$, all runs, with a total of 31 profiles. Colors are used to differentiate between runs.

3.4.2 Effects of the density ratio on the growth rate

Once the self-similar time interval has been defined, we analyse the effect that the density ratio has on the growth rate of the temporal mixing layer, comparing the results of the present zero Mach cases with those obtained by [50] for convective Mach number $M_c = 0.7$. First, consider the growth rate of the momentum thickness, $\dot{\delta}_m$, which is evaluated here following the expression derived in [67],

$$\dot{\delta}_m \approx -\frac{2}{\rho_0 \Delta U^2} \int_{-\infty}^{\infty} \overline{\rho} R_{12} \frac{\partial \tilde{u}}{\partial y} dy. \tag{3.8}$$

This expression is obtained differentiating (3.3) with respect to time, and neglecting viscous terms. An alternative method to compute $\dot{\delta}_m$ is to fit a linear law to the data shown in figure 3.1(a). The differences in the mean and standard deviation of the growth rate of the momentum thickness obtained from both methods are small: for $s = 1$, the first method yields $\dot{\delta}_m/\Delta U = 0.0168 \pm 0.0003$, while the second method yields $\dot{\delta}_m/\Delta U = 0.0170 \pm 0.0002$.

The value of the growth rate of the momentum thickness for $s = 1$ is in good agreement with previous works, especially taking into account the scatter of the available data. For instance, in the "unforced" experiments quoted by [20] the growth rate of the momentum thickness varies from 0.014 to 0.022. Also, [58] report $\dot{\delta}_m/\Delta U = 0.014$ in simulations of incompressible temporal mixing layers, and the experimental data of [6] yield a value of 0.016. For $M_c = 0.3$ and $s = 1$, [50] report $\dot{\delta}_m/\Delta U \approx 0.0184$, a value that decreases to 0.0108 when the Mach number is increased to $M_c = 0.7$.

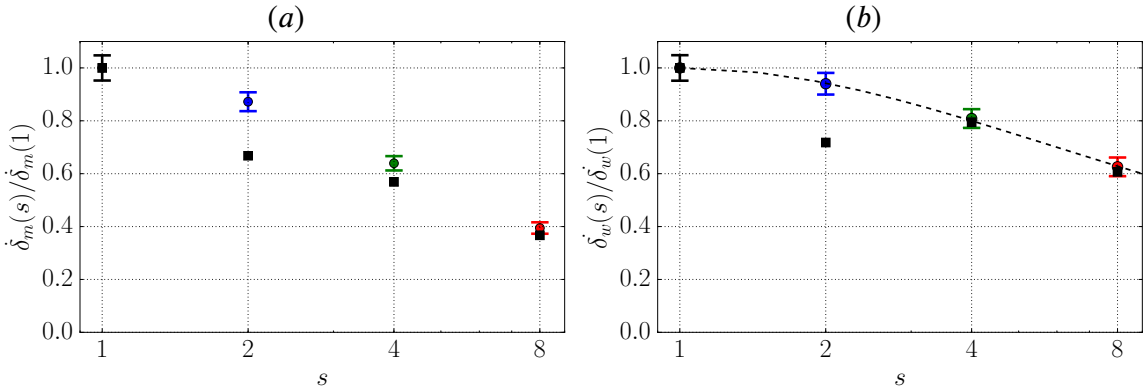

Fig. 3.3 Mixing-layer growth rate as a function of the density ratio. Growth rate based on (a) momentum thickness $\dot{\delta}_m$, and (b) vorticity thickness $\dot{\delta}_w$, normalised by the growth rate for $s = 1.0$. In both panels the horizontal axis is in logarithmic scale. Colored dots with error bars stand for the present results, squares represent results for $M_c = 0.7$ [50]. The dashed curve in (b) corresponds to equation (3.9), from Ramshaw [56].

As the density ratio increases, the values of $\dot{\delta}_m$ decrease. This can be observed in figure 3.3(a), which shows the growth rate ratios, $\dot{\delta}_m(s)/\dot{\delta}_m(1)$, as a function of s. At $s = 8$, our results show that the growth rate of δ_m has been reduced by 60% with respect to the growth rate of the case with $s = 1$. A similar behaviour is observed for the subsonic cases of [50] at $M_c = 0.7$, also included in the figure. The ratio $\delta_m(s)/\delta_m(1)$ is very similar for the $M_c = 0$ and $M_c = 0.7$ cases for large density ratios, with significant differences for the smaller density ratio, $s = 2$. Careful inspection shows that the density ratio $s = 2$ is indeed somewhat anomalous in Pantano and Sarkar [50], presenting a non-monotonic behaviour for some quantities (see for instance the growth rates and the profiles of Reynolds stress, as shown in table 6 and figure 18 respectively in their paper).

The results shown in figure 3.3(a) for $\dot{\delta}_m$ are very similar to those obtained for $\dot{\delta}_w$, which are plotted in figure 3.3(b). Again, our results are compared to the $M_c = 0.7$ cases of [50], and the theoretical prediction by [56]. The latter is based on a model for the growth of the *visual* thickness of a variable density mixing layer at $M_c = 0$, directly comparable to the present results. The model is obtained by extending a linear stability analysis to the nonlinear regime through scaling hypothesis, leading after proper manipulation to

$$\frac{\dot{\delta}_w(s)}{\dot{\delta}_w(1)} = \frac{2\sqrt{s}}{s+1}. \tag{3.9}$$

Figure 3.3(b) shows a very good agreement between Ramshaw's model and our data. The agreement is also fairly good with the subsonic data of [50] at $M_c = 0.7$, except for the case

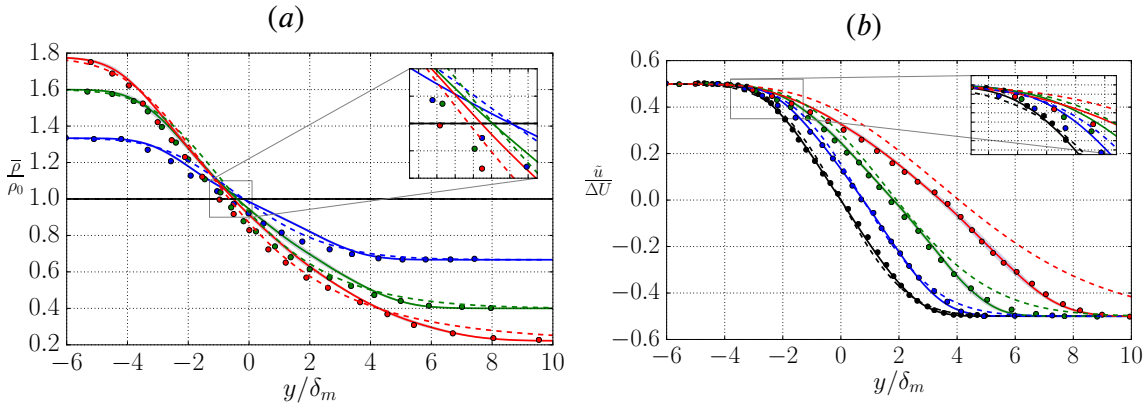

Fig. 3.4 (*a*) Mean density profiles. (*b*) Favre-averaged streamwise velocity profiles. Different colors correspond to different density ratios: black, $s = 1$; blue, $s = 2$; green, $s = 4$; and red, $s = 8$. Solid lines are the present turbulent temporal mixing layers. Dashed lines are the laminar temporal mixing layers (see appendix A). Symbols: Rogers and Moser [58] for $s = 1$, Pantano and Sarkar [50] for s=2, 4 and 8.

$s = 2$ as it happened also for $\dot{\delta}_m$. It should be noted that, to the best of our knowledge, this is the first direct validation of the Ramshaw model with a variable density DNS at $M_c = 0$.

Overall, the results presented in this subsection show that the growth rates of the $M_c = 0$ cases are significantly higher than those reported by Pantano and Sarkar [50] for $M_c = 0.7$, in agreement with previous works. However, the effect of s on the growth rate seems to be very similar at both Mach numbers, with essentially the same reduction in the growth rate except for maybe the low density ratio case, $s = 2$. Also, the effect of s seems to be stronger on δ_m than on δ_w, with $\dot{\delta}_m(s = 8)/\dot{\delta}_m(s = 1) \approx 0.4$ and $\dot{\delta}_w(s = 8)/\dot{\delta}_w(s = 1) \approx 0.6$. As a consequence, the ratio between the two thicknesses, $D_w = \delta_w/\delta_m$, increases with s, as it can be observed in table 3.1. Note that since δ_w and δ_m grow linearly with time, $D_w \approx \dot{\delta}_w/\dot{\delta}_m$ for sufficiently long times. For reference, [50] report a value of $D_w = 5.0$ for a compressible mixing layer with $M_c = 0.3$ and $s = 1$, in good agreement with $D_w = 4.83$ for our $s = 1$ case.

3.4.3 Mean density, velocity and temperature

We now proceed to analyze the one point statistics of the present DNS (mean values in this subsection, higher order moments in §3.4.4), averaging the data in the horizontal directions and in time, binning in $y/\delta_m(t)$. In all the vertical profiles presented in this section, a shadowing has been applied around plus/minus one standard deviation of the horizontally averaged data with respect to the mean, in order to show the uncertainty of the statistics.

Figure 3.4(a) shows mean density profiles, comparing the present zero Mach results with the results of the subsonic mixing layer of Pantano and Sarkar [50] at $M_c = 0.7$. The figure also includes for comparison the results from laminar temporal mixing layers, obtained as discussed in appendix A. As the density ratio increases, the density mixing layer extends further into the low-density stream, with small variations in the position where $\overline{\rho} = \rho_0$. The profiles of the $M_c = 0.7$ and $M_c = 0$ cases are qualitatively similar at any given density ratio, although there are some differences in the profiles in the central part of the mixing layer ($|y| \lesssim 3\delta_m$). The agreement between the $M_c = 0$ and $M_c = 0.7$ cases is better for the Favre averaged velocity, shown in figure 3.4(b). The only exception is maybe the region closer to the high-density free-stream, where the edge of the mixing layer seems sharper for the present simulations ($M_c = 0$). The figure also includes the incompressible data of [58] for $s = 1$, showing a very good agreement with our incompressible case.

Besides some small changes in the shape of the profiles (which will be discussed later), the most apparent effect of the density ratio in $\overline{\rho}$ and $\tilde{u}$ is the shifting of the $\tilde{u}$ profile towards the low density side. Note that this effect is apparent in both turbulent cases ($M_c = 0$ and $M_c = 0.7$), as well as in the laminar self-similar profiles (dashed lines in figure 3.4). This shifting of the mean density and velocity profiles with the density ratio has already been reported in previous studies, both experimental and numerical, and it has been explained qualitatively in terms of the behaviour of the large scales near the denser stream [10] and their linear stability properties [61]. Fewer authors have tried to quantify this shift. For instance, Pantano and Sarkar [50] quantified the shift in terms of the differences between the $\overline{\rho}$ and $\tilde{u}$ profiles, using two semi-empirical relationships, $\overline{\rho}(\tilde{u})$ and $R_{12}(\tilde{u})$. They later used these relationships to estimate the reduction of the momentum thickness growth rate. Also, Bretonnet et al. [8] studied laminar mixing layers with density variations due to different effects (high-speed, thermal, mass), characterizing the drift as the distance between the inflection points of the velocity and density mean profiles.

In order to quantify this shifting, we propose here to use Δ: the distance between the y locations where $\tilde{u} = 0$ and $\overline{\rho} = \rho_0$, positive when $\tilde{u}$ is displaced towards y-positive (low-density side in our simulations). The main advantage of the present definition with respect to those used by Pantano and Sarkar [50] and Bretonnet et al. [8] is that it can be easily computed from the mean profiles of velocity and density, without having to compute higher order derivatives. This distance is plotted in figure 3.5 as a function of the density ratio, for turbulent mixing layers with $M_c = 0$ and $M_c = 0.7$, and for the laminar self-similar solutions. The figure shows two possible scalings for Δ, with δ_m (figure 3.5a) and with δ_w (figure 3.5b). The different datasets collapse better with the second scaling, especially for

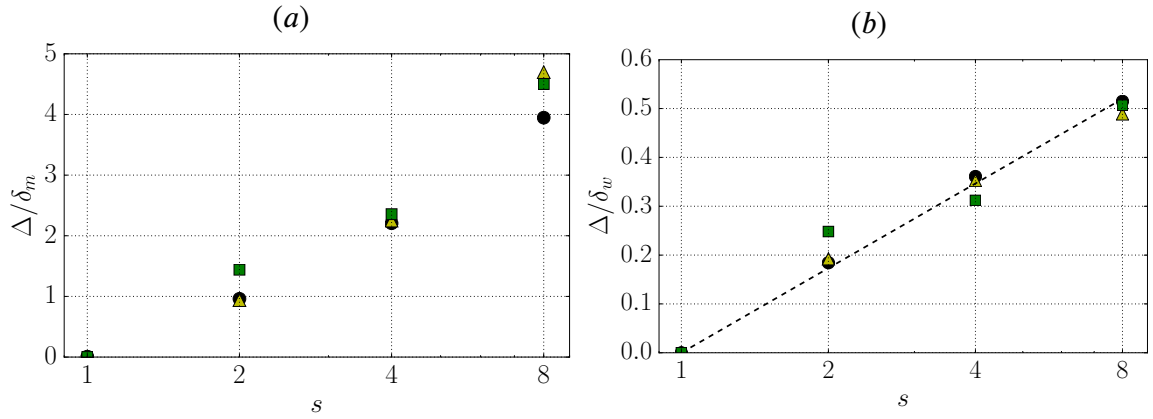

Fig. 3.5 Shifting of the mixing layer, normalized with (*a*) the momentum thickness, (*b*) the vorticity thickness. Circles for present DNS at $M_c = 0$. Squares for Pantano and Sarkar [50] at $M_c = 0.7$. Triangles for laminar self-similar solutions. The dashed line in (*b*) corresponds to $\Delta/\delta_w = 0.25\log(s)$.

$s = 8$ cases, suggesting an empirical relation

$$\Delta(s) = \delta_w(s) C_\Delta \log(s), \tag{3.10}$$

with $C_\Delta = 0.25$. This empirical approximation yields correlation coefficients of $R^2 = 0.998$ for the present DNS results at $M_c = 0$. Similar values of C_Δ are obtained for the other datasets in the figure. The results of [50] at $M_c = 0.7$ yield $C_\Delta = 0.23$ and $R^2 = 0.956$, and the laminar self-similar solutions yield $C_\Delta = 0.23$ and $R^2 = 0.994$.

Although the present definition of shifting is not directly comparable to the one used by [50], it is also possible to relate the present Δ to the ratio $\delta_m(s)/\delta_w(s)$. Lets assume that the mean density and velocity profiles are

$$\overline{\rho} = \rho_0 + \frac{\rho_t - \rho_b}{2} F_\rho\left(\frac{y}{\delta_w}\right), \quad \text{and} \quad \tilde{u} = -\frac{\Delta U}{2} F_u\left(\frac{y}{\delta_w} - \frac{\Delta}{\delta_w}\right), \tag{3.11}$$

where $F_u(\xi)$ and $F_\rho(\xi)$ tend to ± 1 when $\xi \to \pm\infty$, and Δ is assumed to be a function of the density ratio, s. Note that this is equivalent to limit the effect of s to a shift between the profiles of $\overline{\rho}$ and $\tilde{u}$, with no explicit change in their shape. Introducing (3.11) into (3.3), it is possible to show that

$$\frac{\delta_m(s)}{\delta_w(s)} = \frac{\delta_m(1)}{\delta_w(1)} + \frac{\lambda(s)}{2}\int_{-\infty}^{\infty} F_\rho(\xi)\left[1 - \left(F_u\left(\xi - \frac{\Delta}{\delta_w}\right)\right)^2\right] d\xi = \frac{\delta_m(1)}{\delta_w(1)} + \lambda(s) G\left(\frac{\Delta}{\delta_w}\right), \tag{3.12}$$

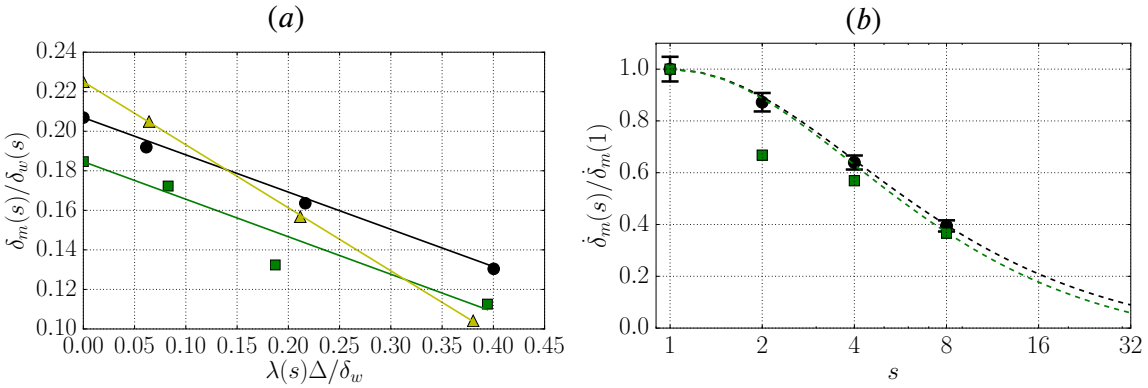

Fig. 3.6 Effects of s and Δ on the reduction of the momentum thickness. (a) δ_m/δ_w versus $\lambda(s)\Delta/\delta_w$. ($b$) $\dot{\delta}_m/\dot{\delta}_w$ versus s. In both panels, cicles are the present DNS at $M_c = 0$, squares are [50] at $M_c = 0.7$, and triangles are the self-similar solution for the laminar temporal mixing layer. The solid lines in (a) correspond to equation (3.13) with: black, $C = 0.188$; green, $C = 0.190$; yellow, $C = 0.32$. The dashed lines in (b) correspond to (3.14) with: black, $C' = 0.047$ and $\dot{\delta}_w(1)/\dot{\delta}_m(1) = 4.8$, green, $C' = 0.047$ and $\dot{\delta}_w(1)/\dot{\delta}_m(1) = 5.4$.

where $\lambda(s) = (s-1)/(s+1)$. Note that by construction $G(0) = 0$ and $G'(0) < 0$. Hence, it is possible to simplify (3.12) to

$$\frac{\delta_m(s)}{\delta_w(s)} = \frac{\delta_m(1)}{\delta_w(1)} - C\lambda(s)\frac{\Delta}{\delta_w} + O\left(\frac{\Delta}{\delta_w}\right)^2. \tag{3.13}$$

Interestingly, piecewise linear expressions for F_ρ and F_u yield $C = 1/3$ and a cubic leading order error in (3.13).

In order to estimate C from the DNS data, figure 3.6(a) shows the ratio $1/D_w = \delta_m/\delta_w$ as a function of $\lambda(s)\Delta/\delta_w$. The figure shows that $C = 0.188$ for the present $M_c = 0$ data, yielding a correlation coefficient between the data and the linear approximation equal to $R^2 = 0.998$. For the $M_c = 0.7$ case, the ratio of the growth rates at $s = 1$ is smaller, but the slope of the curve seems to be approximately the same ($C = 0.190$, $R^2 = 0.920$), supporting the assumption that F_ρ, F_u (and hence C) do not vary much with the density ratio. Note that for the laminar case, with notable differences in the shape of $\tilde{u}$ and ρ (and hence in F_u and F_ρ), the value of the constant is $C = 0.32$ and the linear approximation is exact ($R^2 = 1$).

Finally, it is possible to combine (3.9), (3.10) and (3.13) to obtain a semi-empirical prediction of the reduction of the momentum thickness growth rate with the density ratio,

$$\frac{\dot{\delta}_m(s)}{\dot{\delta}_m(1)} \approx \frac{2\sqrt{s}}{s+1}\left(1 - \frac{\dot{\delta}_w(1)}{\dot{\delta}_m(1)}C'\log(s)\right). \tag{3.14}$$

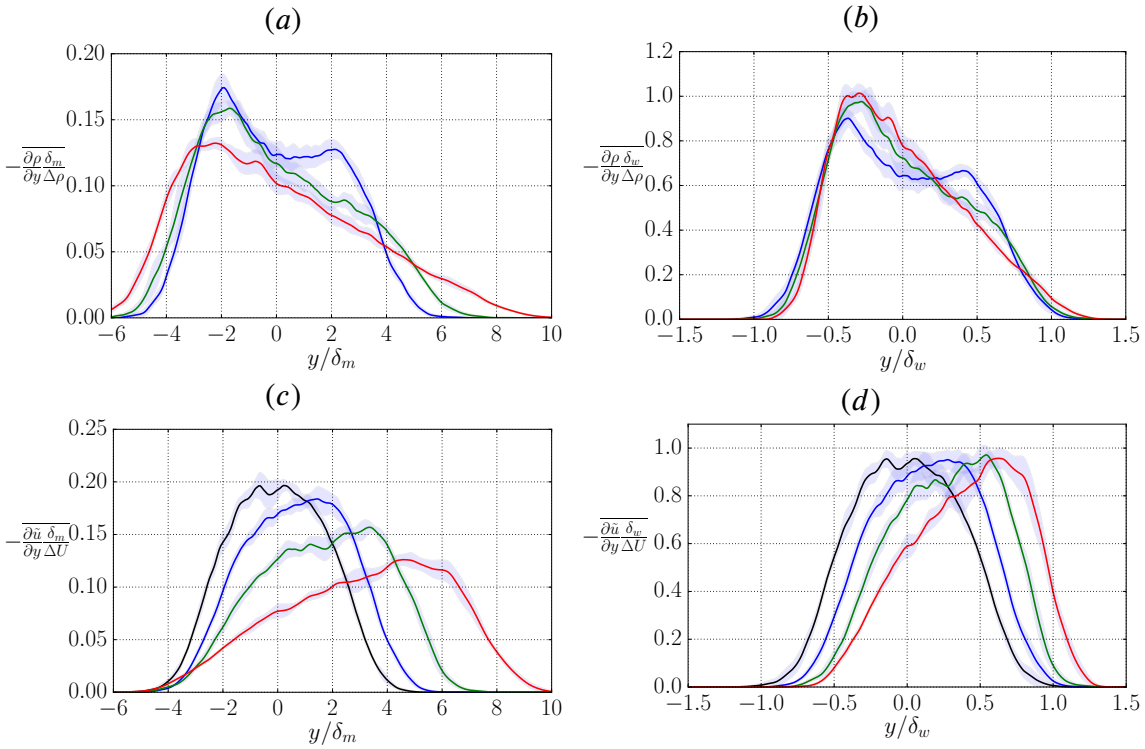

Fig. 3.7 (a),(b) Profiles of the vertical gradients of the mean density. (c),(d) Profiles of the vertical gradients of the Favre-averaged streamwise velocity. (a),(c) Normalized with the momentum thickness. (b),(d) Normalized with the vorticity thickness. Different colours correspond to different density ratios: black, $s = 1$; blue, $s = 2$; green, $s = 4$; red, $s = 8$.

To obtain (3.14) we have also taken advantage of $1/D_w = \delta_m/\delta_w \approx \dot{\delta}_m/\dot{\delta}_w$, which is a reasonable approximation for sufficiently long times. The performance of this simple model for the reduction of the momentum thickness growth rate is evaluated in figure 3.6(b), where the dashed lines corresponds to equation (3.14) with $C' = C \cdot C_\Delta = 0.047$ and the appropriate value for $\dot{\delta}_w(1)/\dot{\delta}_m(1)$, black for $M_c = 0$ and green for $M_c = 0.7$. The figure also includes the DNS data for both mach numbers. The agreement between the DNS data and the model is very good, except for the lower density ratios of the $M_c = 0.7$ cases, which already showed differences when compared to the present $M_c = 0$ cases in figure 3.3.

In the previous discussion, the effect of s on the shape of the profiles of $\overline{\rho}$ and $\tilde{u}$ has been neglected, resulting in a reasonable approximation for the reduction in the growth rate of the mixing layer with s. However, the density ratio has some effects in the shapes of $\overline{\rho}$ and $\tilde{u}$, which are responsible for changes in the structure of the turbulence in the mixing layer. These effects, which are difficult to evaluate in figure 3.4, are better observed in figure 3.7, which shows the vertical gradients of the mean profiles with different normalizations.

In particular, the gradients of the mean density normalized with $\Delta\rho = \rho_b - \rho_t$ and δ_w seem to collapse reasonably well (see figure 3.7b), especially in the high density side (lower stream). More differences are visible near the low density side, where it is apparent that the gradients tend to become smoother with increasing s. Indeed, for $s = 8$, figure 3.7a and b show that the gradient of $\overline{\rho}$ is roughly linear, so that $\overline{\rho}$ becomes roughly parabolic for $y \gtrsim -2\delta_m \approx -0.25\delta_w$. Although outside of the scope of the present paper, it would be interesting to check whether the same linear region in $\partial\overline{\rho}/\partial y$ is obtained for higher density ratios. The shifting of the velocity profiles discussed above is clearly visible when looking at their corresponding gradients, figures 3.7(c) and (d). For $\tilde{u}$ the change of shape of the profile results in the maximum gradients appearing nearer to the lower density side, with smoother gradients in the high density side. Indeed, opposite to what is observed for ρ, case $s = 8$ seems to develop a nearly parabolic profile for $\tilde{u}$ towards the higher density side of the mixing layer ($y \lesssim 4\delta_m \approx y \lesssim 0.5\delta_w$).

To finalize this subsection, we turn our attention to the mean temperature distribution, more especifically to the non-dimensional temperature jump $\overline{\theta} = (\overline{T} - T_b)/(T_t - T_b)$. It is interesting to study the temperature since it follows and advection-diffusion equation, equation (2.4). This allows the comparison of the variable density cases ($s = 2$, 4 and 8) with the passive scalar simulated for the uniform density case ($s = 1$). Note that although the temperature is inversely proportional to the density (equation of state), the same is not true for the mean temperature and mean density. Figure 3.8(a) shows the mean temperature profiles for all cases and figure 3.8(b) the corresponding profiles of the vertical gradients of the mean temperature. The passive scalar shows a roughly symmetric distribution, with $\partial\overline{\theta}/\partial y$ peaking near the edges of the mixing layer ($|y/\delta_w| \approx 0.5$). The small deviation with respect to a symmetric profile provides an impression about the convergence of the statistics. With increasing s, the mean temperature profiles shifts towards the upper stream (low density stream) in a similar way as the Favre-averaged streamwise velocity. The profiles also become more asymmetric, which is more clearly visible in the mean temperature gradients shown in figure 3.8(b). As the density ratio increases, the gradients at the high density edge of the mixing layer are strongly damped, while the gradients at the low density edge are enhanced.

3.4.4 Higher order statistics

The shifts in the mean velocity and temperature, as well as the changes in their gradients, are also accompanied by changes in the root mean square of velocity and temperature fluctuations, which are analized in figure 3.9. In particular, figure 3.9(a)-(c) displays the vertical profiles of the turbulent stress tensor, R_{ij}, where the spanwise component, R_{33}, has been

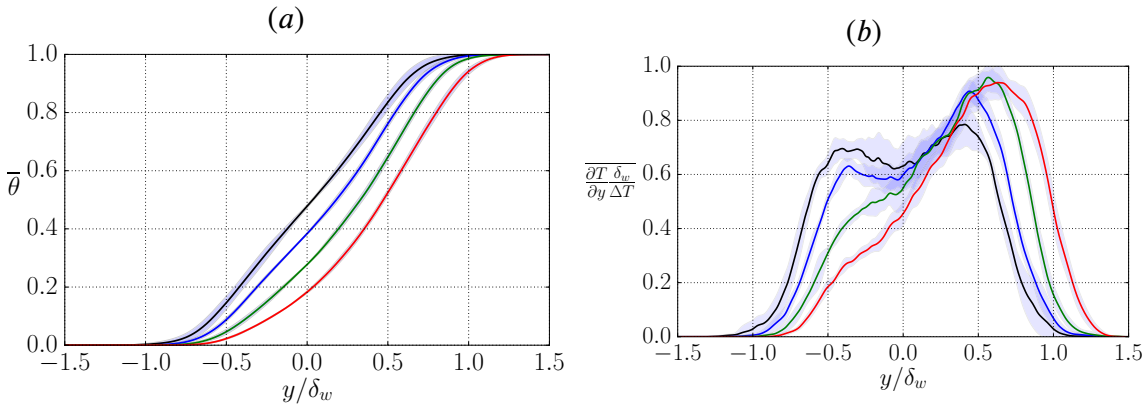

Fig. 3.8 (*a*) Mean temperature profiles. (*b*) Profiles of the vertical gradients of the mean temperature. Different colours correspond to different density ratios: black, $s = 1$; blue, $s = 2$; green, $s = 4$; red, $s = 8$.

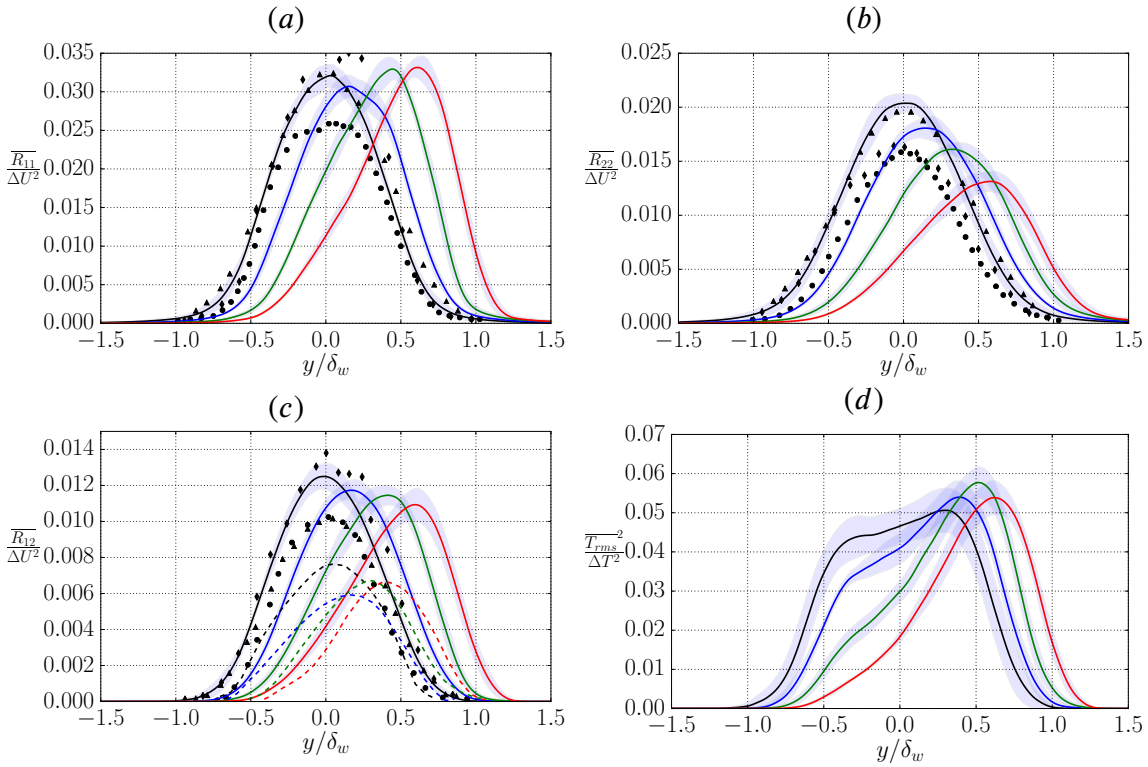

Fig. 3.9 Vertical profiles of (*a*) $R_{11}/\Delta U^2$, (*b*) $R_{22}/\Delta U^2$, (*c*) $R_{12}/\Delta U^2$, and (*d*) $T^2_{rms}/\Delta T^2$. Different colours correspond to different density ratios: black, $s = 1$; blue, $s = 2$; green, $s = 4$; and red, $s = 8$. Solid lines are the present turbulent temporal mixing layers. Symbols are data from incompresible mixing layers: dots from simulations of [58], triangles from experiments of [6] and diamonds from experiments of [63]. Dashed lines in (*c*) represent results from $M_c = 0.7$ [50].

omitted since it is qualitatively similar to the cross-stream component R_{22}. The plots include the data for the incompressible mixing layer of Rogers and Moser [58], and the experimental results of Bell and Mehta [6] and Spencer and Jones [63]. Both datasets show profiles that are consistent with the shape of the present $s = 1$ case, although there is considerable scatter between the three datasets. The scatter in R_{12} (figure 3.9*c*) is consistent with the scatter in the growth-rates of the mixing layers, since these two quantities are related through equation (3.8). This could also explain the scatter in R_{11} and R_{22}. As the density ratio increases, R_{ij} tend to shift towards the low-density region, following the maximum gradient of $\tilde{u}$. Interestingly, while the peak values of R_{22}, R_{12} and R_{33} (the latter is not shown in figure 3.9) decrease with increasing s, the peak values of R_{11} seem to remain roughly constant (at least within the uncertainty in the statistics, shown in the figure by the shaded areas around each curve). The high-speed data of [50] are also included in figure 3.9*c*, and they also show a decrease of the peak values of R_{12} with increasing s, although for the $M_c = 0.7$ data the decrease is not monotonic as it is for the present $M_c = 0$ results. Note also that, as expected, the $M_c = 0.7$ profiles have lower maximum values, consistent with the lower growth rate of the subsonic mixing layers (as discussed in §3.4.2 and in 50).

Figure 3.9(*d*) displays the variance of the temperature, T^2_{rms}, normalized with the jump in temperature across the mixing layer, $\Delta T = T_t - T_b$. For $s = 1$ the temperature corresponds to the passive scalar, which starts to show the double-peak rms observed in high Reynolds numbers mixing layers by others (e.g., see 54). When the density ratio is increased, the peak on the high density side gradually decreases, while the peak on the low-density side shifts with the mean temperature gradients (see figure 3.8*b*). Indeed, consistent with the mean temperature gradients, the peaks of $T^2_{rms}/\Delta T^2$ increase with s, except for maybe case $s = 8$. At the present moment, the reason for the non-monotonous behaviour of $s = 8$ is unclear. It could be related to a decrease in the Re_λ for this case. Another possible explanation could be the onset of interferences of the finite-size of the computational domain with the evolution of the mixing layer.

Finally, figure 3.10 shows the profiles of the skewness, S, and kurtosis, K, of the temperature and the velocity field. Since these profiles are more noisy than the second order moments beyond the edge of the mixing layer, figure 3.10 only shows them in the region limited by 98% of the free stream velocity, indicated with vertical dotted lines. For reference, the horizontal dashed lines represent the expected value for a Gaussian distribution, i.e. $S = 0$ and $K = 3$. Due to the symmetry of the configuration for the passive scalar case, $s = 1$, we expect an antisymmetric distribution for the skewness and a symmetric distribution for the kurtosis. Deviations from this symmetry in figure 3.10 are small and provide an impression of the convergence of the statistics. Note also that the almost linear profile of $\overline{\theta}$

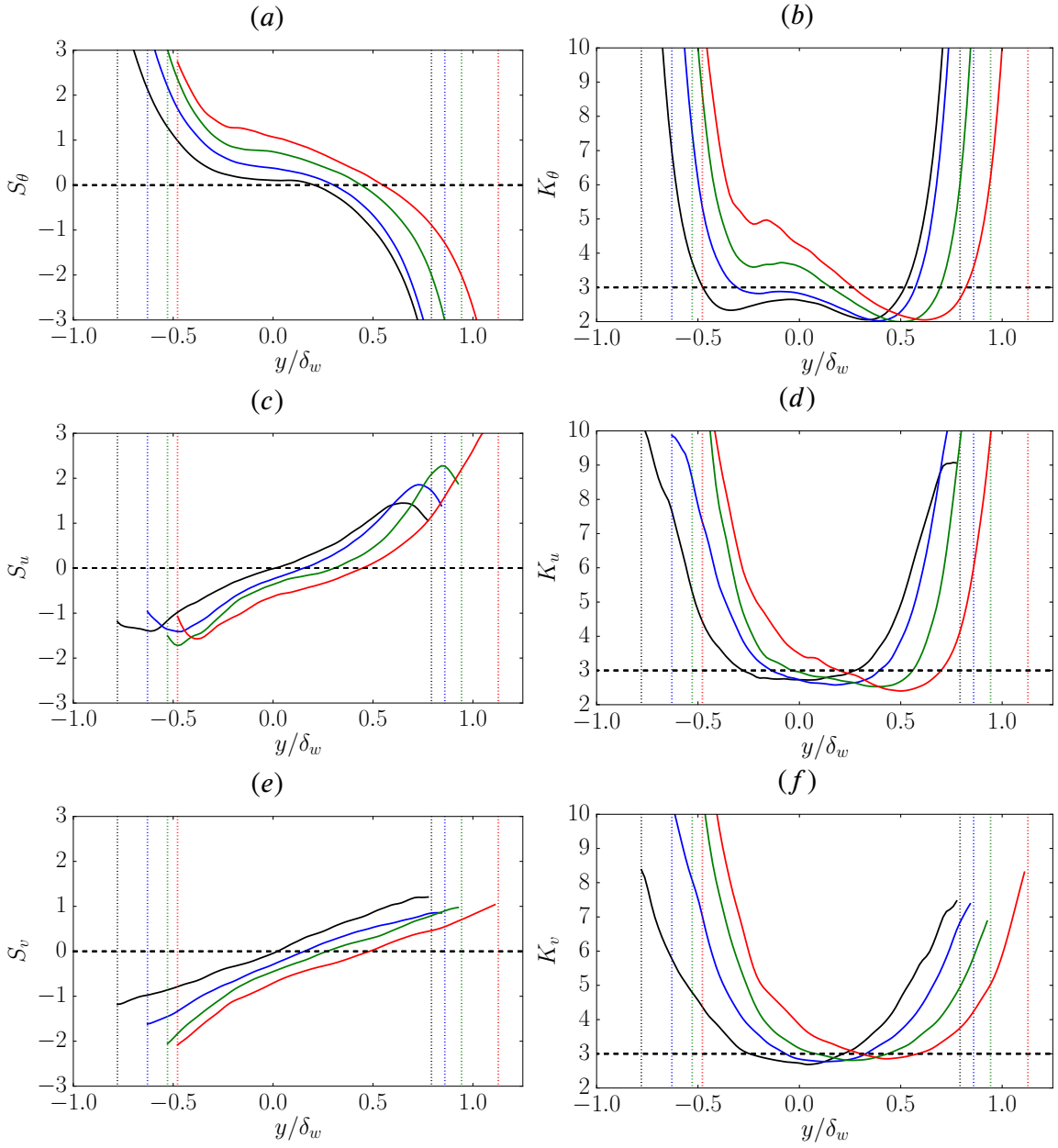

Fig. 3.10 (*a*) Skewness distribution and (*b*) Kurtosis distribution of temperature θ; (*c*) Skewness distribution and (*d*) Kurtosis distribution of streamwise velocity u; (*e*) Skewness distribution and (*f*) Kurtosis distribution of vertical velocity v. Different colours correspond to different density ratios: black, $s = 1$; blue, $s = 2$; green, $s = 4$; and red, $s = 8$.

in the center of the mixing layer results in $S_\theta \approx 0$ for the case with $s = 1$ (remind the broad maximum of the vertical gradient of $\overline{\theta}$ in figure 3.8).

[11] measured the skewness and kurtosis in a spatially-developing mixing layer. Their neutral case is comparable to the present passive scalar case. They distinguish between two zones. First, a mixed region in the central part, characterized by a moderate slope of the temperature skewness profile and an almost constant value of all kurtosis profiles. The value of K in this region is somewhat smaller than the Gaussian value. Secondly, the entrained region in the outer part that presents higher slopes of the temperature skewness profile than the mixed, region and also steep gradients of all kurtosis profiles. All these features are clearly observed in the present profiles for the passive scalar case.

Overall, increasing s results in a shift of the profiles of S and K to the low density side, for both temperature and velocity. This is especially clear in S_u, S_v and K_v, which show small variations on the shape of the profiles (see figures 3.10c, e and f). For the skewness of the temperature (see figure 3.10a) we can observe the same shift, and a gradual increase of S_θ on the high density half of the central region of the mixing layer. This is probably a consequence of the narrowing of the maximum of $\partial\overline{\theta}/\partial y$ with s, and its displacement towards the high temperature (low density) side: a sharper edge on the high temperature side makes it more likely for a pocket of high temperature fluid to be entrained into the mixing layer, biasing S_θ towards positive values. It is also interesting to observe that, on top of the shifting, K_θ and K_u show some changes in their shape with s. In particular, both kurtosis become larger in the high density half of the mixing layer ($y \lesssim 0$). This can be interpreted as an increase in the intermittency of u and T, and it suggests that mixing becomes more difficult near the high density region as s increases, in agreement with the qualitative arguments of [10] regarding the reduced velocity fluctuations near the denser stream. As a result, the size of the well mixed region (i.e., with values of K below the Gaussian threshold) is reduced.

3.4.5 Turbulence structure

We provide now visualizations to obtain an impression of the changes in the turbulent structures of the mixing layer induced by the density ratio. Instantaneous fields of the temperature and velocity field are shown in figures 3.11, 3.12 and 3.13, using vertical planes (figures 3.11 and 3.13 for θ and u, respectively) and horizontal planes (figure 3.12 for θ at the plane $y = 0$). For case $s = 1$, in which the temperature is a passive scalar, the visualization in figure 3.11(a) shows the typical features of a turbulent mixing layer, with patches of mixed fluid in the central region alternating with patches of unmixed fluid that are entrained from both streams. The presence of quasi-2D rollers is visible in both temperature (figure 3.11a) and velocity

(a)

(b)

(c)

(d)

Fig. 3.11 Visualization of θ on an xy-plane, at the beginning of the self-similar evolution. The corresponding density ratios and times are (*a*) $s = 1$, $t\Delta U/\delta_m^0 = 400$; (*b*) $s = 2$, $t\Delta U/\delta_m^0 = 418$; (*c*) $s = 4$, $t\Delta U/\delta_m^0 = 455$; and (*d*) $s = 8$, $t\Delta U/\delta_m^0 = 570$.

(a)

(b)

(c)

(d)

Fig. 3.12 Visualization of θ on an xz-plane at $y = 0$, at the beginning of the self-similar evolution. The corresponding density ratios are (*a*) $s = 1$, (*b*) $s = 2$, (*c*) $s = 4$, (*d*) $s = 8$. Times as in figure 3.11.

(a)

(b)

(c)

(d)

Fig. 3.13 Visualization of streamwise velocity on an xy-plane, at the beginning of the self-similar evolution. The corresponding density ratios are (*a*) $s = 1$, (*b*) $s = 2$, (*c*) $s = 4$, (*d*) $s = 8$. Times as in figure 3.11. The black lines show contours of $u = \pm\Delta U/2$.

(figure 3.13*a*) visualizations, but maybe more clearly so in the midplane visualization of the temperature shown in figure 3.12(*a*).

Increasing the density ratio produces small changes in the flow visualizations. The quasi-2D rollers are also observed for $s = 2$, 4 and 8 in both temperature (figure 3.11*b*, *c* and *d*) and velocity (figure 3.13*b*, *c* and *d*). Also, in agreement with the results discussed in section 3.4.3, the mixing layer shifts upwards (towards the low density side) with increasing s, as it can be observed in figure 3.11 and 3.13. In addition, the temperature field becomes somewhat smoother at the small scales. This fact is reflected in the lower value of Re_λ obtained in the cases with large s, as shown in table 3.1.

The shift of the mixing layer is also apparent in the visualization of the $y = 0$ plane sown in figure 3.12. With increasing s the temperature field at this height is increasingly dominated by patches of fluid entrained from the lower stream. The footprint of the quasi-2D rollers is also clear in the figure 3.12 for all density ratios.

We can better visualize the turbulent structures changes in figure 3.14, with a direct comparison between the cases $s = 2$ (on the left) and $s = 8$ (on the right). On the top of the figure, iso-surfaces of $T(s) = T_\mathrm{t} - 0.1\Delta T$ are shown for both cases, this magnitude would give an insight about the energy structures distribution. Namely, we observe that these structures are bigger and blunter for $s = 8$. On the other hand, at the bottom part of 3.14, we present iso-surfaces of Q equal to two times its standard deviation $Q(s) = 2Q_\mathrm{std}$, where Q is the widely used velocity gradient invariant (e.x. [18]). This magnitude would give an insight on the small structures of the flow related to the energy dissipation. Note that for both density ratio cases, we can easily distinguish the turbulence characteristic vortex structures. Once again, the structures found are larger for $s = 8$ but more dispersed than for $s = 2$; these differences are due to the different turbulent state of both cases, with a significantly larger Re_λ value for the case $s = 2$ (140 versus 90).

Finally, it is interesting to observe in figure 3.13 that the turbulence within the mixing layer produce irrotational perturbations into the free-stream, with characteristic sizes of the order of δ_w. This potential perturbations are relatively weak, and are highlighted in figure 3.13 by contours of $u = \pm\Delta U$ (in black).

In order to quantify the changes in the structure of the turbulent motions in the mixing layer due to the density ratio, we proceed to analyze the one dimensional spectra of velocity and temperature fluctuations: $E_{ii}(k_x, y)$ and $E_{ii}(k_z, y)$ for $i = u, v$ and T (no summation). These spectra are computed during runtime, as functions of $k_x\delta_m^0$, $k_z\delta_m^0$, y/δ_m^0 and t. Then, during post-processing, these spectra are interpolated into wavenumbers and vertical distances normalized with $\delta_w(t)$, and averaged (ensemble and in time) for the self-similar

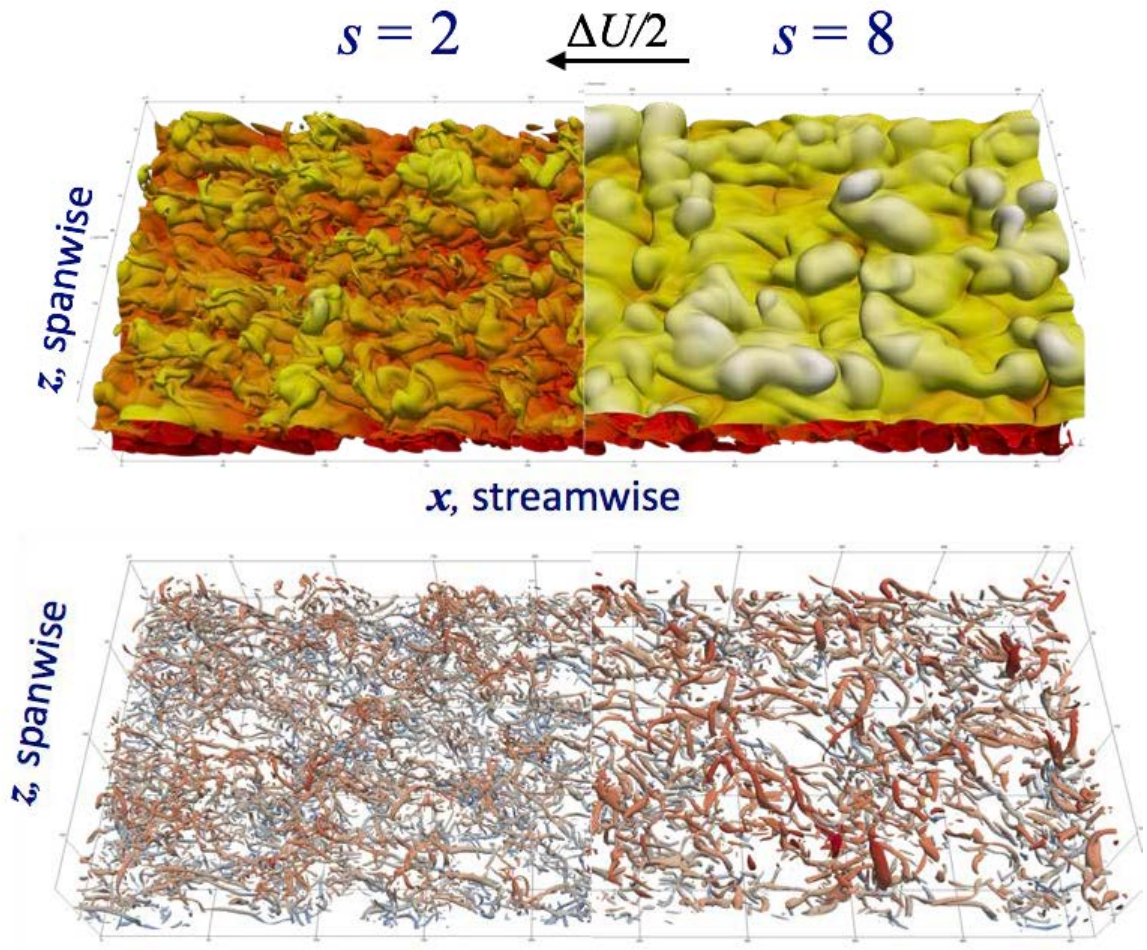

Fig. 3.14 Structures comparison between case $s = 2$ and $s = 8$. Top figure: temperature iso-surfaces $T(s) = T_t - 0.1\Delta T$, bottom figure $Q(s) = 2Q_{std}$; x-z coordinates corresponds to x/δ_m^0 and z/δ_m^0. Color code is used to represent the crosswise component of the points y/δ_m^0.

evolution of the mixing layer. The smallest wavenumbers considered in the interpolation are $k_x^0\delta_w \approx 0.4 - 0.5$ and $k_z^0\delta_w \approx 1.1 - 1.3$, depending on the density ratio.

Figure 3.15 shows the premultiplied spectra ($k_x E_{ii}$ and $k_z E_{ii}$), as a function of the vertical position in the mixing layer and the streamwise or spanwise wavelength, $\lambda_x = 2\pi/k_x$ and $\lambda_z = 2\pi/k_z$. The spectra is premultiplied by the wavenumber so that, when plotted in log-scale for the wavelength, the area under the surface corresponds to the actual energy content of a given range of wavelengths. The contours plotted in the figure correspond to 20% and 40% of the maxima among all cases, so that they represent equal levels of energy density for all cases. The small inset to the right of each panel shows the energy in wavenumbers smaller than k_x^0 and k_z^0, denoted $E_{k_x=0}$ and $E_{k_z=0}$, respectively. From a physical point of view, these two quantities roughly corresponds to the energy in structures that are infinitely long or wide.

For the incompressible case, figure 3.15 shows that the spectra of u tend to be longer than wide, while the spectra of v and T tend to be wider than long. Indeed, both T and v show considerably more energy on structures that are wide ($\lambda_z > 2\pi/k_z^0 \approx 5\delta_w$) than in structures that are long ($\lambda_x > 2\pi/k_x^0 \approx 12\delta_w$), which is shown by $E_{k_z=0} > E_{k_x=0}$. This is consistent with the observations of the 2D rollers in the flow visualizations. It is also apparent that the spectra of v is shifted towards smaller scales with respect to the spectra of u and T, both in λ_x and λ_z. In terms of the vertical extension of the spectra, 3.15(a) and (b) show that the temperature spreads over $|y| \lesssim 0.8\delta_w$, while u and v are limited to a narrower region ($|y| \lesssim 0.5\delta_w$), in agreement with the results shown in figure 3.9. Interestingly, figure 3.15(e) shows that E_{vv} has a larger spread in the vertical direction, at about $\lambda_x \approx 4\delta_w$. Careful inspection of figures 3.15(a) and (b) shows that those peaks correspond to infinitely wide structures ($k_z = 0$): note that $E_{vv}(\lambda_z, y)$ at $y = 0.7\delta_w$ has little energy in figure 3.15(f), while $E_{kz=0}$ at that height is maximum. Although not shown here, instantaneous visualizations of v show that these wavelengths ($\lambda_x \approx 4\delta_w$, $\lambda_z \to \infty$) roughly correspond to potential perturbations of v into the free-stream.

As the density ratio increases, figures 3.15(a) and (b) show that the spectra of the temperature gradually shifts towards the low density side (see the contours of 20% in the figures). The shift occurs first on the high density edge of the spectrum ($y < 0$), and a bit later in low density side ($y > 0$). Note that for $y/\delta_w \gtrsim 0.25$, there are little differences between the spectra of the $s = 1$ and $s = 2$ cases, consistent with the agreement of T_{rms}^2 in figure 3.9(d) in these same vertical locations. In terms of the effect of s in the streamwise and spanwise wavelengths, figure 3.15(a) shows that the longest scales in the high density side are gradually inhibited ($\lambda_x/\delta_w \approx 5 - 10, y \approx 0$). The same effect, although weaker, is also present in the spanwise wavelengths (figure 3.15b). In terms of the small scales, figures 3.15(a) and

(b) suggest that the effect of s is stronger on λ_z than on λ_x. This could be related to the fact that the small scales in x are not only due to turbulent fluctuations (i.e., vortices), but to the formation of sharp gradients $\partial T/\partial x$, due to the roll-up of the shear layer (see blue lines in figures 3.11 and 3.12).

The behavior of the spectra of u and v in figures 3.15($c - f$) is qualitatively similar to that discussed for T, with all spectra shifting towards the low-density side, with a gradual reduction of the energy in small scales (both λ_x and λ_z). There is also a clearer reduction of the energy of large scales near the high-density edge of the mixing layer, more apparent for wide ($\lambda_z/\delta_w \gtrsim 3 - 5$) structures than for long structures ($\lambda_x/\delta_w \gtrsim 5 - 10$). The u and v spectra of cases $s = 1$ and $s = 2$ also agree reasonably well near the low-density edge of the mixing layer ($y \gtrsim 0.25\delta_w$), except for the v spectrum at about $\lambda_x \approx 4\delta_w$, suggesting that even a small change on the density ratio has an important effect on the potential perturbations of the mixing layer into the free-stream.

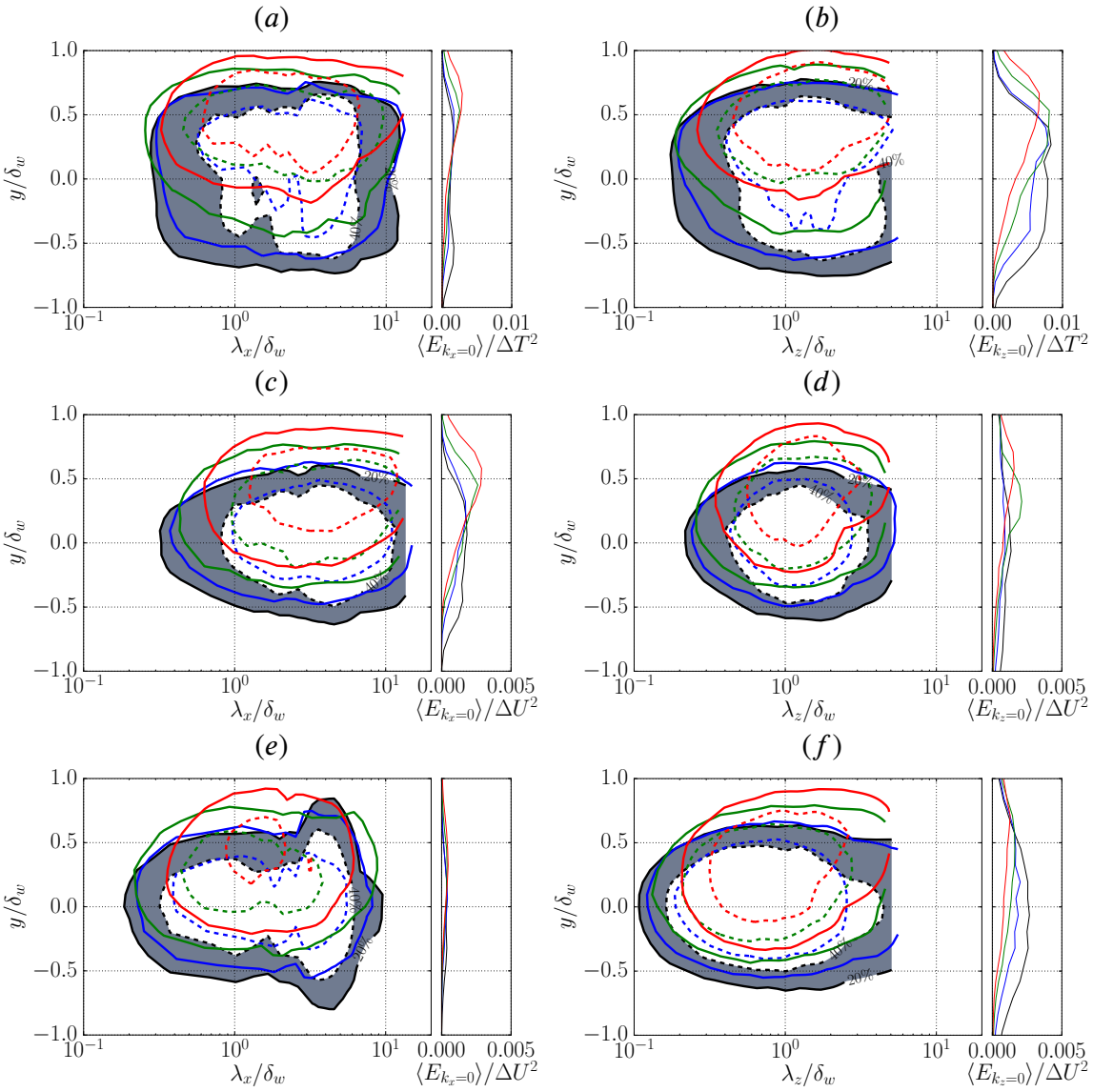

Fig. 3.15 Vertical distribution of the premultiplied spectral energy distribution of velocity and temperature. (*a*) $k_x E_{\theta\theta}(\lambda_x, y)$. (*b*) $k_z E_{\theta\theta}(\lambda_z, y)$. (*c*) $k_x E_{uu}(\lambda_x, y)$. (*d*) $k_z E_{uu}(\lambda_z, y)$. (*e*) $k_x E_{vv}(\lambda_x, y)$. (*f*) $k_z E_{vv}(\lambda_z, y)$. The inset to the right of each panel shows the energy in wavenumbers not included in the corresponding panel (see text for discussion). The contours plotted correspond to 20% (solid) and 40%(dashed) of the maxima of all the spectra shown in each panel. Different colours correspond to different density ratios: black with shading, $s = 1$; blue, $s = 2$; green, $s = 4$ and red, $s = 8$.

3.5 Conclusions

In this chapter we have presented results from direct numerical simulations of temporal, turbulent mixing layers with variable density. The simulations are performed in the low-Mach number limit, so that temperature and density fluctuations develop while the thermodynamic pressure remains constant. Four different density ratios are considered, $s = 1$, 2, 4 and 8, which are run in large computational boxes until they reach an approximate self-similar evolution. To give an impression of the turbulence in these mixing layers, during the self-similar evolution the Reynolds numbers based on the Taylor micro-scale vary between $Re_\lambda = 140$-150 for the case $s = 1$, and $Re_\lambda = 85$-95 for the case with the highest density ratio, $s = 8$.

The results of the simulations show that, in agreement with turbulent mixing layers with higher velocities (and convective Mach number, $M_c = 0.7$), the growth rate of the momentum thickness decreases with the density ratio. However, the decrease is more marked for high speeds. Hence, at a given density ratio, the momentum thickness of the low-Mach number mixing layer will grow faster than the subsonic one. However, the ratio between the growth rate for large density ratios and the growth rate of the $s = 1$ case seems to be independent of the flow speed in the range considered. For example, for $s = 8$ a 60% growth reduction with respect to $s = 1$ is obtained for both the present low Mach number case and the $M_c = 0.7$ case.

In terms of the visual thickness of the mixing layer, the effect of the density ratio in the growth reduction with respect to the $s = 1$ case is smaller, and our results agree with previous theoretical models for $M_c = 0$ and with the data of high-speed mixing layers. However, the growth rate reduction for low density ratio ($s = 2$) is not the same in the $M_c = 0$ and in the $M_c = 0.7$ cases from Pantano and Sarkar [50]. The reason for this discrepancy is unclear at the moment.

The Favre averaged profiles of velocity show that with increasing density ratio, the gradients shift towards the low density side. The behaviour is analogous to that observed in high-speed mixing layers. Indeed, the velocity and density profiles of our low-Mach number cases agree qualitatively well with the high-speed cases when the vertical distance is normalised with δ_m. There are some small differences in the mean velocities near the low density stream, and the density profiles of the high-speed cases seem to be displaced with respect to the low-Mach number profiles.

We have quantified the shifting of the Favre-averaged velocity profiles as a function of the density ratio obtaining an empirical relation. Using this empirical relation and a theoretical prediction of the reduction of the vorticity thickness growth rate due to Ramshaw [56], we have developed a semi-empirical prediction of the reduction of the momentum thickness growth rate with the density ratio, see equation (3.14). From a physical point of view, the

model assumes that the only effect of the density ratio is a shift in the velocity profile, with no change on the shape of the density and velocity profiles. Our data for $M_c = 0$ and the data of Pantano and Sarkar [50] for $M_c = 0.7$ are in good agreement with the model prediction, except for maybe the $M_c = 0.7$ case at low density ratios ($s \approx 2$). It would be interesting to check the validity of the model prediction for higher density ratios.

The fluctuations profiles of the low-Mach number cases show that, as expected, the fluctuations follow the gradients, shifting towards the low-density region. The analysis of the skewness and the kurtosis of the fluctuations shows that increasing the density ratio, the well mixed region that appears in the central region of the case $s = 1$ becomes narrower, since mixing becomes more difficult near the high density side as the density ratio is increased.

Finally, the flow structures have been analyzed using flow visualizations and premultiplied spectra. The spectra shows that with increasing density ratio there is a shift towards the low density side and the longest scales in the high density side are gradually inhibited. A gradual reduction of the energy in small scales with increasing density ratio is also observed. This effect is consistent with the reduction of Re_λ with increasing density ratio mentioned above.

Chapter 4

Differential diffusion in laminar and turbulent diffusion flames

4.1 Introduction

This chapter deals with nonpremixed combustion systems in which the fuel and the air enter the combustion chamber through separate feed streams. When the chemical reactions are sufficiently fast, the combustion process is known to be controlled by the transport rates of the chemical species and heat. The solution can be described in the first approximation by considering the Burke–Schumann limit of infinitely fast reaction rate, in which the flame appears as a surface separating two equilibrium regions, one without fuel and the other without oxidizer, with the reactants reaching the flame from opposite sides in stoichiometric proportions. In this limit the temperature exhibits an apparent peak at the flame, whose value T_f at a given location depends on the transport rates of heat and reactants in the outer equilibrium regions and also on the heat losses by conduction to the combustor walls or by radiation.

To focus on differential-diffusion effects our analysis below will consider radiation-free systems with adiabatic walls. Under those conditions it is well know that, when the reactant diffusivities are equal to the thermal diffusivity (i.e. for unity Lewis numbers of the reactants), the transport rates of reactants and heat are balanced outside the flame in such a way that the resulting flame temperature is everywhere uniform, with a value equal to the adiabatic flame temperature T_S obtained by burning at constant pressure the reactive mixture formed by mixing in stoichiometric proportions the fuel and the oxidizer streams. In most combustion systems employing air as oxidizer, the assumption of unity Lewis number is a good approximation for O_2. By way of contrast, the approximation $L_F = 1$ of unity Lewis number is only accurate for methane and methanol. Consequently, for these two fuels the

resulting diffusion-flame temperature T_f differs by a small amount from T_S, but for all other fuels differential-diffusion effects associated with non-unity values of L_F can be expected to be significant, leading to flame temperatures $T_f \neq T_S$. According to the prevailing understanding, for values of $L_\mathrm{F} < 1$, corresponding for instance to hydrogen-air combustion, the rate of fuel transport into the flame sheet is higher than the rate of heat removal, resulting in superadiabatic temperatures $T_f > T_S$, while the opposite is expected to occur for heavy fuels with $L_\mathrm{F} > 1$.

In general, the value of $T_f - T_S$ may vary along the flame as a consequence of the balance of accumulation, convection, and diffusion in the outer equilibrium regions, so that the result depends on the specific flow conditions, including in particular the flow geometry, the relevant Reynolds number, and the dilution of the fuel-feed stream. The present numerical investigation is intended to contribute understanding on these dependences by considering different flow configurations. Widely used selfsimilar configurations are studied first, beginning with the two-dimensional steady counterflow and coflow configurations as well as the one-dimensional unsteady planar mixing layer. Following, a time-dependent planar diffusion flame distorted by a vortex, equivalent to a three-dimensional steady vortex flame in a stretched field, is considered. Finally, three-dimensional simulations of temporal mixing layers are analyzed.

4.2 Literature survey

An important effort has been devoted to better understand the effect of preferential diffusion on combustion processes. In [2], numerical simulations of the response of a premixed flame to randomly defined two-dimensional flow fields were performed. They assumed a one-step reaction with a large activation energy, studying the case of $L_F = 0.5$ and $L_F = 2$, keeping constant density. They concluded that flames with $L_F = 0.5$ have a larger probability for increased reaction rate and demonstrated a high correlation between strain-rate normal to the flame and the excess enthalpy.

In 1995, [60] explored differential diffusion effects in non-premixed turbulent jet flames. This was an experimental study with chemically reacting turbulent jets of H_2 (36%) and CO_2 (64%) into air. They compared with laminar flame calculations for opposed flow flame using the Chemkin-based numerical model and Sandia transport property code to account for diffusion of all species. They found that average and fluctuating effects of differential diffusion are greatest on the fuel rich side of the flame (where H_2 exists). Continuing this research, in 2005 Barlow [5] published results from multi-scalar point measurements of piloted 25% CH_4/75% air jet frames, emphasizing the importance of molecular diffusion and turbulent transport in these flames for laminar, transitional and turbulent regimes. Their results pointed to an evolution in the scalar structure from one dominated by molecular diffusion at low Reynolds numbers to one that is dominated by turbulent transport, showing only minor effects of differential species diffusion. This same conclusion was found by [68] and [4]. In [68], a comprehensive study to evaluate the effect of molecular transport on the PDF modeling of turbulent non-premixed flames was performed. They used Sandia piloted jet flame E as the validation test case with three configurations: neglecting the molecular transport (A), considering the molecular transport (B), and considering both the molecular transport and its effect on mixing (C). They assumed equal diffusivities for all species, stating that the study of the modeling of differential diffusion and its effect on the PDF modeling would be an interesting future work.

In the work by Maragkos, Rauwoens and Merci [42], they analyzed the effect in the gas composition and maximum flame temperature to incorporate differential diffusion effects in CFD simulations of turbulent reactive flows (LES). The maximum flame temperature exceeded the adiabatic temperature when considering differential diffusion (DD) up to 400 K. This same effect was also observed by [33], also observing a vortical intensity and velocity distortions reduction when considering DD. In [14], laminar flame calculations for a Tsuji counterflow geometry were made with the objective of investigating salient features caused by the differential diffusion effect in nitrogen-diluted hydrogen diffusion flames. They solved reacting and non-reacting flows with 0, 1, 5, 15, 25, 50 and 77 % nitrogen in hydrogen as

the fuel stream. A detailed chemical mechanism is used in the numerical calculations (48 steps). They identified two source terms on the differential diffusion parameter z_H: mixing and chemical reactions. They concluded that dilution in the fuel stream rather than strain rate has a strong influence on the magnitudes of z_H in reacting flows, where chemical source term becomes the dominant contribution on z_H. For acoustically pulsed Burke-Schumann hydrogen flames, Chaos, Welle and Roberts [12], isolated the effect of fuel Lewis number on flame dynamics by investigating steady and unsteady 40% H_2/60% He ($L_F > 1$) and 40%H_2/ 60% Ar ($L_F < 1$) flames. For $L_F < 1$, local temperature increased with stretch imparted on the reaction zone by the unsteady flow, whereas the opposite trend was observed for $L_F > 1$. Moreover, they observed that unsteadiness yielded higher flame temperatures than steady flames for $L_F > 1$.

Sutherland, Smith and Chen [64], presented a general method for evaluating differential diffusion in premixed or non-premixed systems based on conservation equations for the elemental mass fractions, forming a basis for analyzing differential diffusion. They tested their method for one-dimensional, steady, opposed flow diffusion flame and 2D spatially evolving *turbulent* jets with different detailed chemistry models: one being a $CO/H_2/N_2$-air jet with $Z_{st} = 0.296$ and the second a $CH_4/H_2/N_2$-air jet flame with $Z_{st} = 0.167$. On the other hand, results from one-dimensional laminar calculations showed that differential diffusion near the stoichiometric mixture fraction can be sensitive to strain rate, particularly for hydrocarbon flames (attributed primarily to the generation of H_2 in the flame zone). They concluded that, in the context of LES, as filter size increases, the importance of differential diffusion relative to molecular diffusion on the filter scale diminishes. The most recent publication found on differential molecular diffusion is [28]. In this work, they analyzed two previously generated DNS datasets, studying the effect of differential molecular diffusion (DMD) in turbulent non-premixed flames. In agreement with previous works, they found that DMD decreases when Re increases. They did not analyze the effect on temperature in this work, focusing on the differences on the mixture fractions of the different elements ($z_{\alpha\beta}$) instead.

As stated by [28], *The modeling of differential molecular diffusion in turbulent combustion remains a challenge. Incorporating detailed molecular diffusion treatment in existing turbulent combustion models in non-trivial since many existing turbulent combustion models do not transport species and energy directly due to the closure problem associated with the highly nonlinear reaction source terms. In turbulent non-premixed combustion, chemical reaction occurs at the molecular scale, and thus how the reactants are brought together at the molecular scale directly determines the chemical pathways. Fundamentally, it is molecular diffusion that ultimately mixes reactants at the molecular scale. A quantitative under-*

standing of the effect of molecular diffusion and its interaction with turbulent diffusion and chemical reaction is needed.

4.3 Formulation

We address non-premixed combustion systems in which the fuel and the air are provided by different feed streams, with dilution with an inert gas permitted in the fuel-feed stream for generality. The temperature in the air and fuel feed streams will be denoted by T_A and T_0, and the corresponding reactant mass fractions are $Y_{O_2A} = 0.232$ and $Y_{F_0} \leq 1$. The Lewis number of the oxygen will be assumed to be unity, a good approximation in most fuel-air systems, whereas a general non-unity Lewis number L_F will be employed for the fuel. The focus of the analysis will be on the description of differential-diffusion effects, with specific attention given to the quantification of the unbalanced transport rates in the convective-diffusive regions, leading to flame temperatures T_f that differ from the stoichiometric adiabatic value.

This fundamental transport problem can be investigated by assuming that the reaction between the fuel and the oxygen occurs according to the infinitely fast irreversible reaction $F + sO_2 \rightarrow (1+s)P + q$, where s is the amount of oxygen needed to burn the unit mass of fuel and q in the amount of heat released in the process. Note that, although the quantification of the flame temperature is performed in the diffusion-controlled Burke-Schumann limit of infinitely fast reaction, because of the strong temperature sensitivity of the reaction rates, the variations in temperature described here are fundamental for the description of finite-rate effects, with temperature decrements possibly leading to extinction. In the Burke-Schumann limit considered here the flame appears as a surface $\Sigma_f(x) = 0$ separating a region without oxygen and a region without fuel. Following [40], the problem is formulated with use made of coupling functions, including the two mixture-fraction variables

$$Z = \frac{S\hat{Y}_F - \hat{Y}_O + 1}{S + 1} \tag{4.1}$$

and

$$\tilde{Z} = \frac{S\hat{Y}_F/L_F - \hat{Y}_O + 1}{S/L_F + 1} \tag{4.2}$$

and the normalized excess-enthalpy variable

$$\xi = \frac{c_p(T - T_A) + (qY_{F_0}/S)(\hat{Y}_O - 1)}{c_p(T_0 - T_A) + (qY_{F_0}/S)}, \tag{4.3}$$

involving the amount of air needed to burn the unit mass of fuel $S = sY_{F_0}/Y_{O_2A}$, the normalized reactant mass fractions $\hat{Y}_O = Y_{O_2}/Y_{O_2A}$ and $\hat{Y}_F = Y_F/Y_{F_0}$, the temperature T, and the specific heat at constant pressure c_p, which is assumed to be constant. The coupling

functions satisfy the conservation equations

$$\frac{\partial}{\partial t}(\rho Z) + \nabla \cdot (\rho \mathbf{v}) - \frac{1}{L_m}\nabla \cdot \left(\rho D_T \tilde{Z}\right) = 0, \tag{4.4}$$

involving the effective Lewis number

$$L_m = \frac{S+1}{S/L_F + 1}, \tag{4.5}$$

and

$$\frac{\partial}{\partial t}(\rho \xi) + \nabla \cdot (\rho \mathbf{v} \xi) - \nabla \cdot \left(\rho D_T \xi\right) = 0 \tag{4.6}$$

with boundary conditions $Z = \tilde{Z} = \xi = 1$ in the fuel stream and $Z = \tilde{Z} = \xi = 0$ in the air stream. In the notation, ρ and D_T represent the density and the thermal diffusivity, respectively. Equations (4.4) and (4.6) must be complemented with the chemical equilibrium condition $\hat{Y}_O \hat{Y}_F = 0$ and the definitions (4.1) - (4.3) to allow us to calculate $\hat{Y}_F$, $\hat{Y}_O$, and T in terms of Z (or $\tilde{Z}$) and ξ. At the flame surface $\Sigma_f(x,t) = 0$ the reactant mass fractions $\hat{Y}_F$ and $\hat{Y}_O$ are simultaneously zero, corresponding to values of the mixture fraction $Z = Z_S = 1/(1+S)$ and $\tilde{Z} = \tilde{Z}_S = 1/(1+S/L_F)$. For $Z \geq Z_S$

$$\hat{Y}_O = 0; \quad \hat{Y}_F = \frac{Z - Z_S}{1 - Z_S} = \frac{\tilde{Z} - \tilde{Z}_S}{1 - \tilde{Z}_S}, \quad T - T_A = (T_0 - T_A)\xi + (\Delta T)_c(1-\xi), \tag{4.7}$$

whereas for $Z \leq Z_S$

$$\hat{Y}_F = 0; \quad \hat{Y}_O = 1 - \frac{Z}{Z_S} = 1 - \frac{\tilde{Z}}{\tilde{Z}_S}, \quad T - T_A = (T_0 - T_A)\xi + (\Delta T)_c(Z/Z_S - \xi), \tag{4.8}$$

The expressions for the temperature in (4.7) and (4.8) have been written in terms of the characteristic combustion temperature increase

$$(\Delta T)_c = \frac{q Y_{F_0}}{c_p S} = \frac{q Y_{O_2 A}}{c_p s}. \tag{4.9}$$

This last equation indicates that $(\Delta T)_c$ is independent of the dilution of the fuel stream, with typical values of the order of $(\Delta T)_c \approx 2000 - 2200K$. As we shall see below, a related

quantity of interest is the adiabatic flame temperature

$$T_S = T_A + (T_0 - T_A)Z_S + (\Delta T)_c(1 - Z_S), \tag{4.10}$$

resulting from the adiabatic combustion, at constant pressure, of the reactive mixture generated by mixing in stoichiometric proportions the air and fuel streams, each at its initial temperature.

The piecewise linear relation between Z and $\tilde{Z}$ defined in n (4.7) and (4.8) is needed to integrate (4.4). The gradients of $\tilde{Z}$ and ξ are continuous at the flame surface, whereas that of Z exhibits a jump, associated with the localized chemical source. The distribution of the $\xi_f(x,t)$ on the flame surface $\Sigma_f(x,t) = 0$, to be obtained as part of the solution, determines the flame temperature according to

$$T_f = T_A + (T_0 - T_A)\xi_f + (\Delta T)_c(1 - \xi_f). \tag{4.11}$$

The solution simplifies greatly when $L_F = 1$, when $Z = \tilde{Z} = \xi$ everywhere in the flow field. Consequently, the flame value of the excess enthalpy is simply $\xi_f = Z_S = 1/(S+1)$ and the associated flame temperature evaluated from (4.11) becomes $T_f = T_S$, equal the adiabatic flame temperature defined in (4.10). By way of contrast, when $L_F \neq 1$ the value of the excess enthalpy at the flame differs in general from the stoichiometric value of the mixture fraction. Correspondingly, the flame temperature computed from (4.11) with $\xi_f \neq Z_S$ deviates from the stoichiometric adiabatic value by an amount given by

$$\frac{T_f - T_S}{(\Delta T)_c + T_A - T_0} = (Z_S - \xi_f), \tag{4.12}$$

obtained by subtracting (4.10) from (4.11). As can be inferred from (4.12), since the characteristic temperature increases due to combustion, $(\Delta T)_c$ is much larger than $T_A - T_0$ for all cases of practical interest and values of ξ_f higher/lower than Z_S correspond to subadiabatic/superadiabatic flame temperatures, respectively.

According to the prevailing understanding of differential-diffusion effects, for values of $L_F < 1$ the rate of fuel transport into the flame sheet is higher than the rate of heat removal, resulting in superadiabatic temperatures with $\xi_f < Z_S$, while the opposite is expected to occur for heavy fuels with $L_F > 1$. The extent of this effect can be anticipated to be smaller in flows dominated by convective transport and larger in flows dominated by diffusive transport. To see this, note that with diffusive transport neglected in (4.4) and (4.6) the solution reduces to $\xi = Z$, so that $\xi = \xi_f = Z_S$ at the flame, yielding $T_f = T_S$, as follows from (4.12). By

way of contrast, if diffusive transport is domimant, the solution to (4.4) and (4.6) reduces to $\xi = \tilde{Z}$. The associated flame value of the excess enthalpy $\xi_f = \tilde{Z}_S$ can be used in (4.12) to yield

$$\frac{T_d - T_S}{(\Delta T)_c + T_A - T_0} = \frac{Z_S(1 - Z_S)(1 - L_F)}{1 - (1 - L_F)Z_S}, \tag{4.13}$$

where T_d is the flame temperature with diffusion-controlled transport. Although one would expect the flame temperature to lie between the adiabatic stoichiometric value T_S and the diffusion-controlled value T_d given in (4.13), the computations presented below will reveal more complex behaviors, with the nonlinear interactions occurring in the outer transport regions leading to flame temperatures lying outside these anticipated bounds.

4.4 One-dimensional flamelet models

The computation of the distribution of T_f on the flame surface $\Sigma_f(x,t) = 0$ requires integration of the transport equations (4.4) and (4.6) coupled with the continuity and momentum equations. In the integration, the relationships (4.7) and (4.8) are employed to evaluate the temperature and composition in terms of Z and ξ, with the equation of stated used to compute the density. Besides, expressions must be provided for the transport properties in terms of the temperature and composition. Different flows of increasing complexity are to be addressed below, beginning with two canonical one-dimensional configurations, namely, counterflow and coflow diffusion flames.

4.4.1 Counterflow Burke-Schumann flames

Consider the planar mixing layer separating two steady counterflowing streams of fuel and air, with the fuel coming from $y = \infty$ and the air coming from $y = -\infty$. In agreement with the notation introduced above, the subscripts A and 0 will be used to denote properties in the air and fuel stream, respectively, so that, for instance, the densities will be denoted by ρ_A and ρ_0. In the stagnation region the velocity outside the mixing layer is given by $u = A_A x$ and $v = -A_A y$ on the air side and by $u = A_0 x$ and $v = -A_0 y$ on the fuel side. Here x and y represent cartesian coordinates measured from the stagnation point, with y pointing towards the fuel stream, and u and v are the associated velocity components. The strain rates of the colliding streams are in general different, with the condition of vanishing pressure jump across the mixing layer providing the relationship $A_0/A_A = (\rho_A/\rho_0)^{1/2}$. A simplified sketch for this configuration is shown on 4.1.

The solution in the mixing layer is selfsimilar, with the temperature and composition being function of the distance y to the stagnation plane. Following [40], we choose to describe the flow in terms of the thermal-conductivity-weighted coordinate

$$\zeta = \left(\frac{A_A}{D_{T_A}}\right)^{1/2} \int_0^y \frac{dy}{(\lambda'/\lambda_A)} \tag{4.14}$$

and associated transverse mass flow rate

$$F = -\frac{\rho v}{\rho_A (D_{T_A} A_A)^{1/2}} \tag{4.15}$$

where λ' is the local value of the thermal conductivity and D_{T_A} is the thermal diffusivity in the air stream, whose properties are used to define the dimensionless variables $T^* = T/T_A$,

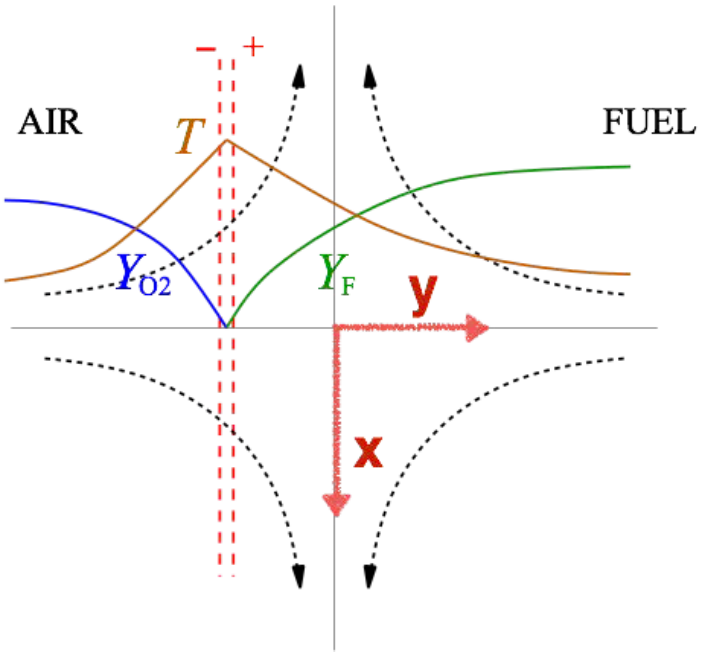

Fig. 4.1 Counterflow Burke-Schumann flame sketch.

$\rho^* = \rho/\rho_A$, $\lambda^* = \lambda'/\lambda_A$, $A^* = A/A_A$. In the following, the asterisks denoting dimensionless quantities will be dropped to simplify notation.

The variables ξ and F can be used to write the continuity and streamwise momentum equations

$$\frac{dF}{d\zeta} - \rho\lambda A = 0 \tag{4.16}$$

$$Pr\frac{d^2}{d\zeta^2} + F\frac{dA}{d\zeta} + \lambda(1 - \rho A^2) = 0 \tag{4.17}$$

whereas the conservation equations (4.4) and (4.6) become

$$\frac{1}{L_m}\frac{d^2\tilde{Z}}{d\zeta^2} + F\frac{dZ}{d\zeta} = 0, \tag{4.18}$$

$$\frac{d^2\xi}{d\zeta^2} + F\frac{d\xi}{d\zeta} = 0. \tag{4.19}$$

In the momentum equation Pr denotes the Prandtl number of the gas mixture, with $Pr = 0.7$ used in the integrations reported below. The above equations must be supplemented with

$$Z \geq Z_S : \frac{Z - Z_S}{1 - Z_S} = \frac{\tilde{Z} - \tilde{Z}_S}{1 - \tilde{Z}_S}, T - 1 = \left(\frac{T_0}{T_A} - 1\right)\xi + \frac{(\Delta T)_c}{T_A}(1 - \xi), \tag{4.20}$$

$$Z \leq Z_S : 1 - \frac{Z}{Z_S} = 1 - \frac{\tilde{Z}}{\tilde{Z}_S}, T - 1 = \left(\frac{T_0}{T_A} - 1\right)\xi + \frac{(\Delta T)_c}{T_A}(Z/Z_S - \xi), \tag{4.21}$$

obtained by writing (4.7) and (4.8) in dimensionless from, and by

$$\rho T = 1 \quad \text{and} \quad \lambda = T^{\sigma} \tag{4.22}$$

obtained by neglecting variations of the mean molecular weight in the equation of state along with variations with composition of the thermal conductivity, with a power law with exponent $\sigma = 0.7$ assumed for the temperature dependence of the latter, a reasonable approximation in most combustion processes. The problem is subject to the boundary conditions $F = 0$ at $\zeta = 0$ and

$$A - 1 = Z = \tilde{Z} = \xi = 0 \quad \text{as} \quad \zeta \to -\infty \tag{4.23}$$

$$A - (T_0/T_A)^{1/2} = Z - 1 = \tilde{Z} - 1 = \xi - 1 = 0 \quad \text{as} \quad \zeta \to \infty, \tag{4.24}$$

where the equation of state has been used to compute the boundary value of the strain rate $A_0/A_A = (\rho_A/\rho_0)^{1/2} = (T_0/T_A)^{1/2}$ as $\zeta \to \infty$.

The numerical integration for given values of S and L_F provides the location of the flame ζ_f and the associated flame value of the excess enthalpy ξ_f which determines through (4.12) the flame temperature T_f. The results depend on the temperature ratio T_0/T_A and on the heat of reaction $(\Delta T)_c/T_A$. The results shown in Fig. 4.2 correspond to equal feedstream temperatures $T_0/T_A = 1$ with $(\Delta T)_c/T_A = 7$ for two different fuel Lewis numbers $L_F = 0.3$ and $L_F = 2.0$, selected to represent the properties of hydrogen and of a heavy hydrocarbon. As expected, for $L_F = 2.0$ the flame value of the excess enthalpy is such that $(Z_S - \xi_f) < 0$, corresponding to the subiadiabatic flame temperatures, whereas the opposite behavior is found for $L_F = 0.3$. The comparison with the value of the temperature increase obtained when transport is dominated by diffusion, given in (4.13), reveals that, perhaps unexpectedly, the magnitude of the temperature departure from the adiabatic value $|T_f - T_S|$ can be larger or smaller than $|T_d - T_S|$ depending on the value of Z_S.

The resulting temperature is also compared with the approximate result obtained by assuming the linear variation $F = \zeta$ for the transverse mass flux, an excellent approximation in counterflow flames ([40]). In that case, the excess enthalpy obtained from integration of

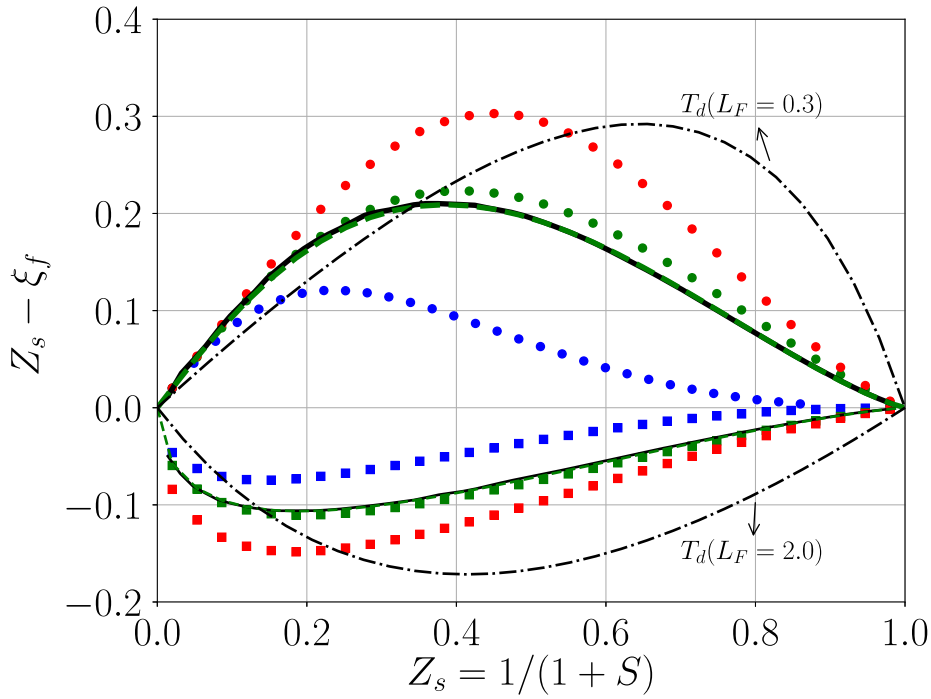

Fig. 4.2 The departure of the flame temperature from the adiabatic value for the counterflow and coflow diffusion flames with T_0/T_A with $(\Delta T)_c/T_A = 7$. Labels as fig. 4.3.

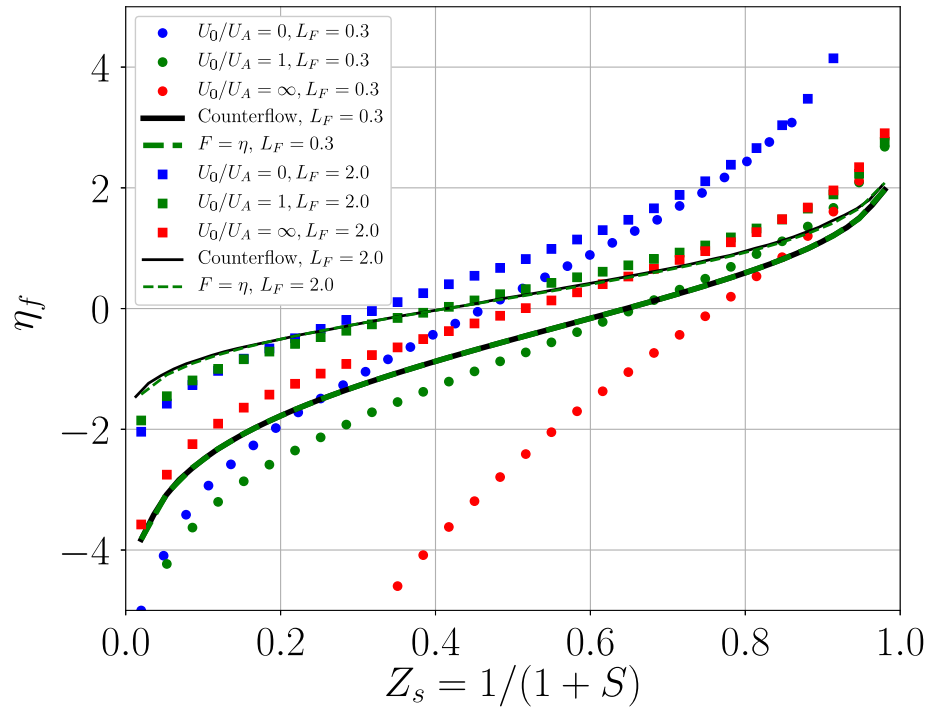

Fig. 4.3 Flame position results for counterflow and coflow diffusion flame problems.

(4.19) reduces to $\xi = \frac{1}{2}[1 + \mathrm{erf}(\zeta/\sqrt{2})]$, whereas integration of (4.18) supplemented with (4.20) and (4.21) provides

$$1 - \frac{Z}{Z_S} = 1 - \frac{\tilde{Z}}{\tilde{Z}_S} = 1 - \frac{1 + \mathrm{erf}(\zeta/\sqrt{2})}{1 + \mathrm{erf}(\zeta_f/\sqrt{2})} \quad \text{for} \quad \zeta < \zeta_f, \tag{4.25}$$

$$\frac{Z - Z_S}{1 - Z_S} = \frac{\tilde{Z} - \tilde{Z}_S}{1 - \tilde{Z}_S} = 1 - \frac{1 - \mathrm{erf}(\zeta\sqrt{L_F/2})}{1 - \mathrm{erf}(\zeta_f\sqrt{L_F/2})} \quad \text{for} \quad \zeta > \zeta_f \tag{4.26}$$

$$\tag{4.27}$$

for the mixture-fraction variables. The flame location is determined from the implicit equation

$$\left(\frac{S}{\sqrt{L_F}}\right)\frac{\exp(-L_F\zeta_f^2/2)}{1 - \mathrm{erf}(\zeta_f\sqrt{L_F/2})} = \frac{\exp(-\zeta_f^2/2)}{1 + \mathrm{erf}(\zeta_f/\sqrt{2})}, \tag{4.28}$$

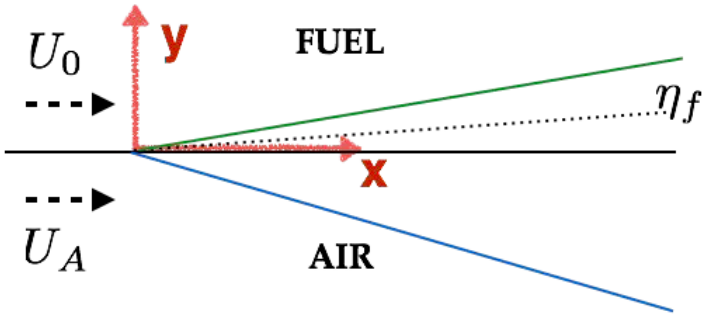

Fig. 4.4 Coflow Burke-Schumann flame sketch.

obtained by imposing the continuity of $d\tilde{Z}/d\zeta$ at the flame. The value of ζ_f can be used to yield

$$\xi_f = \frac{1 + \mathrm{erf}\left(\zeta_f/\sqrt{2}\right)}{2}, \tag{4.29}$$

which is used to generate the prediction shown by a dashed curve in figure 4.2. As can be seen, the approximate solution is almost indistinguishable from that obtained numerically. For completeness, we show in figure 4.3 the flame position ζ_f (η_f in the case of coflow) for the counterflow flame computed both analytically with the $F = \zeta$ approximation and numerically.

4.4.2 Coflow Burke-Schumann flames

As a second canonical problem let us consider the Burke-Schumann diffusion flame separating two parallel streams of fuel and air with velocities U_0 and U_A. Configuration sketch is shown in figure 4.4. Introducing the self-similar coordinate

$$\eta = \left(\frac{U_A}{2D_{T_A}x}\right)^{1/2} \int_0^y \frac{dy}{(\lambda'/\lambda_A)}, \tag{4.30}$$

where x and y are the streamwise and transverse coordinates, and accompanying stream function

$$\psi = \rho_a (2D_{T_A} U_A x)^{1/2} F(\eta) \tag{4.31}$$

reduces the problem to that of integrating

$$\frac{dF}{d\eta} - \rho\lambda u = 0 \tag{4.32}$$

$$Pr\frac{d^2u}{d\eta^2} + F\frac{du}{d\eta} = 0 \tag{4.33}$$

$$\frac{1}{L_m}\frac{d^2\tilde{Z}}{d\eta^2} + F\frac{dZ}{d\eta} = 0 \tag{4.34}$$

$$\frac{d^2\xi}{d\eta^2} + F\frac{d\xi}{d\eta} = 0 \tag{4.35}$$

supplemented by (4.20)-(4.22) with boundary conditions $F = 0$ at $\eta = 0$ and

$$u - 1 = Z = \tilde{Z} = \xi = 0 \quad \text{as} \quad \eta \to -\infty \tag{4.36}$$

$$u - U_0/U_A = Z - 1 = \tilde{Z} - 1 = \xi - 1 = 0 \quad \text{as} \quad \eta \to \infty, \tag{4.37}$$

Here u denotes the streamwise velocity scaled with U_A, so that the velocity ratio U_0/U_A appears as a parameter in the fuel-side boundary condition. The solution in the case $U_0/U_A = 1$ is particularly simple, in that the velocity reduces to $u = 1$ everywhere across the mixing layer. It is worth noting that the resulting mathematical problem becomes identical to that describing the unsteady mixing of two stagnant semi-infinite spaces of fuel and air separated initially by a planar interface, with corresponding selfsimilar coordinate given by $\eta = \int_0^y \lambda^{-1} dy/\sqrt{2D_{T_A}t}$ in terms of the distance y to the initial interface and the time t.

To show the dependence of the flame temperature on the coflow velocity ratio U_0/U_A, figure 4.2 represents results corresponding to the case of equal velocities $U_0/U_A = 1$ along with those corresponding to the extreme cases of stagnant air and stagnant fuel. It is seen that a larger velocity of the fuel stream enhances differential-diffusion effects on flame temperature, both for $L_F = 0.3$ and $L_F = 2.0$, with the $Z_S - \xi_f$ departing more from the adiabatic value. Also of interest is that when the two streams have the same velocity, the resulting peak temperature is not very different from that of the counterflow.

Regarding the flame position, in figure 4.3 is shown that for the coflow case (with $L_F = 0.3$ or $L_F = 2.0$) the flame position for any value of U_0/U_A is bounded between the case $U_0/U_A = \infty$ with $L_F = 0.3$ and the results obtained for $U_0/U_A = 0$ with $L_F = 2.0$.

4.5 Diffusion flame in a vortex

4.5.1 Marble's problem

As a second example, we address the case of a diffusion flame distorted by a vortex with circulation $\Gamma(r)$, a problem introduced by Marble as a model to analyze nonpremixed combustion in a turbulent mixing layers. Specifically, we consider the time evolution of the flow in the presence of a line vortex lying in the initially planar interface separating two semi-infinite spaces of fuel and air. In the thermo-diffusive approximation, the velocity induced is purely azimuthal, with magnitude $\Gamma/(2\pi r)$, and the transport equation for the coupling functions can be written in cylindrical coordinates (r, θ) as

$$\frac{\partial Z}{\partial t} + \frac{\Gamma}{2\pi r}\frac{\partial Z}{\partial \theta} = \frac{D_T}{L_m}\left[\frac{\partial^2 \tilde{Z}}{\partial r^2} + \frac{1}{r}\frac{\partial \tilde{Z}}{\partial r} + \frac{1}{r^2}\frac{\partial^2 \tilde{Z}}{\partial \theta^2}\right] \tag{4.38}$$

$$\frac{\partial \xi}{\partial t} + \frac{\Gamma}{2\pi r}\frac{\partial \xi}{\partial \theta} = D_T\left[\frac{\partial^2 \xi}{\partial r^2} + \frac{1}{r}\frac{\partial \xi}{\partial r} + \frac{1}{r^2}\frac{\partial^2 \xi}{\partial \theta^2}\right], \tag{4.39}$$

The solution must be 2π-periodic and analytic, with initial distribution at $t = 0$ given by $Z = \tilde{Z} = \xi = 1$ for $0 < \theta < \pi$ and $Z = \tilde{Z} = \xi = 0$ for $0 > \theta > -\pi$.

Attention is focused on potential vortices with constant circulation $\Gamma = \Gamma_0$. Because of the absence of geometrical scales there exists a selfsimilar solution involving the rescaled radial coordinate $\eta = r/\sqrt{(\Gamma_0 t)/(2\pi)}$, which reduces the problem to that of integrating

$$-\frac{\eta}{2}\frac{\partial Z}{\partial \eta} + \frac{1}{\eta^2}\frac{\partial Z}{\partial \theta} = \frac{1}{PeL_m}\left(\frac{\partial^2 \tilde{Z}}{\partial \eta^2} + \frac{1}{\eta}\frac{\partial \tilde{Z}}{\partial \eta} + \frac{1}{\eta^2}\frac{\partial^2 \tilde{Z}}{\partial \theta^2}\right) \tag{4.40}$$

$$-\frac{\eta}{2}\frac{\partial \xi}{\partial \eta} + \frac{1}{\eta^2}\frac{\partial \xi}{\partial \theta} = \frac{1}{Pe}\left(\frac{\partial^2 \xi}{\partial \eta^2} + \frac{1}{\eta}\frac{\partial \xi}{\partial \eta} + \frac{1}{\eta^2}\frac{\partial^2 \xi}{\partial \theta^2}\right), \tag{4.41}$$

for $\eta \geq 0$ with the condition that all coupling functions be 2π-periodic in θ, regular at $\eta = 0$, and such that

$$Z = \tilde{Z} = \xi = 1 \quad \text{for} \quad 0 < \theta < \pi \quad \text{and} \quad Z = \tilde{Z} = \xi = 0 \quad \text{for} \quad 0 > \theta > -\pi \quad \text{as} \quad \eta \to \infty. \tag{4.42}$$

The solution depends on the stoichiometric parameters S, on the Lewis number L_F, and on the Peclet number $Pe = \Gamma_0/(2\pi D_T)$.

Note that the same mathematical problem is encountered for the case of a steady diffusion flame wrapped in a stretched vortex with radial, axial and azimuthal velocity components $v_r = -Ar/2$, $v_z = Az$, and $v_\theta = \Gamma/(2\pi r)$, with the corresponding selfsimilar coordinate being in that case $\eta = r/\sqrt{\Gamma/(2\pi A)}$.

4.5.2 Sample numerical results

In order to solve equations (4.38) and (4.39), we decided to make use of a simplified version of code LoMaHZ (explained in Chapter 2). The first step is to write these equations in cartesian coordinates as

$$\frac{\partial Z}{\partial t} - \frac{\Gamma y}{2\pi r^2}\frac{\partial Z}{\partial x} + \frac{\Gamma x}{2\pi r^2}\frac{\partial Z}{\partial y} = \frac{D_T}{L_m}\left(\frac{\partial^2 \tilde{Z}}{\partial x^2} + \frac{\partial^2 \tilde{Z}}{\partial y^2}\right), \tag{4.43}$$

$$\frac{\partial H}{\partial t} - \frac{\Gamma y}{2\pi r^2}\frac{\partial H}{\partial x} + \frac{\Gamma x}{2\pi r^2}\frac{\partial \xi}{\partial y} = D_T\left(\frac{\partial^2 \xi}{\partial x^2} + \frac{\partial^2 \xi}{\partial y^2}\right). \tag{4.44}$$

Presented this way, the velocities u, v are just known functions of (x, y), so we can eliminate from the code the evolution equations for the momentum and the continuity and leave the conservation equations of the scalars $\tilde{Z}$ and ξ. The numerical solution is complicated by the singularity of the velocity at $r = 0$, responsible for the factor r^{-2}. To avoid this, the integrations were performed by using the circulation distribution $\Gamma = \Gamma_0[1 - \exp(-r^2/R_0^2)]$, corresponding to a vortex with a viscous core of characteristic radius r_0. Another difficulties arise when considering the finite computational box and the periodic boundary conditions on the homogeneous direction x. In order to mitigate this effect, the simulations were performed in a large computational domain of size $185R_0$ x $160R_0$ x $10R_0$, up to the point where the solution scaled by $\sqrt{t}$ does not change from one time-step to the next one.

In figure 4.5, the temperature increment $(T-1)/\gamma$ (with $\gamma = \frac{qY_{F0}}{c_p T_A(1+S)}$), is shown for three different Peclet numbers: 10, 100 and 1000; These results are obtained for the case $L_F = 2$ and $S = 4$. It is observed how the flame shape gets more complicated as Pe increases, further approaching the vortex center.

The limit $Pe >> 1$

As shown by Liñán, the problem can be further simplified in the limit $Pe \to \infty$ when mixing is confined to thin layers of relative characteristic thickness $Pe^{-1/2}$ about the spiral interfaces $\theta - \eta^{-2} = 0$ and $\theta - \eta^{-2} = \pi$. To investigate mixing in this limit, it is convenient to replace

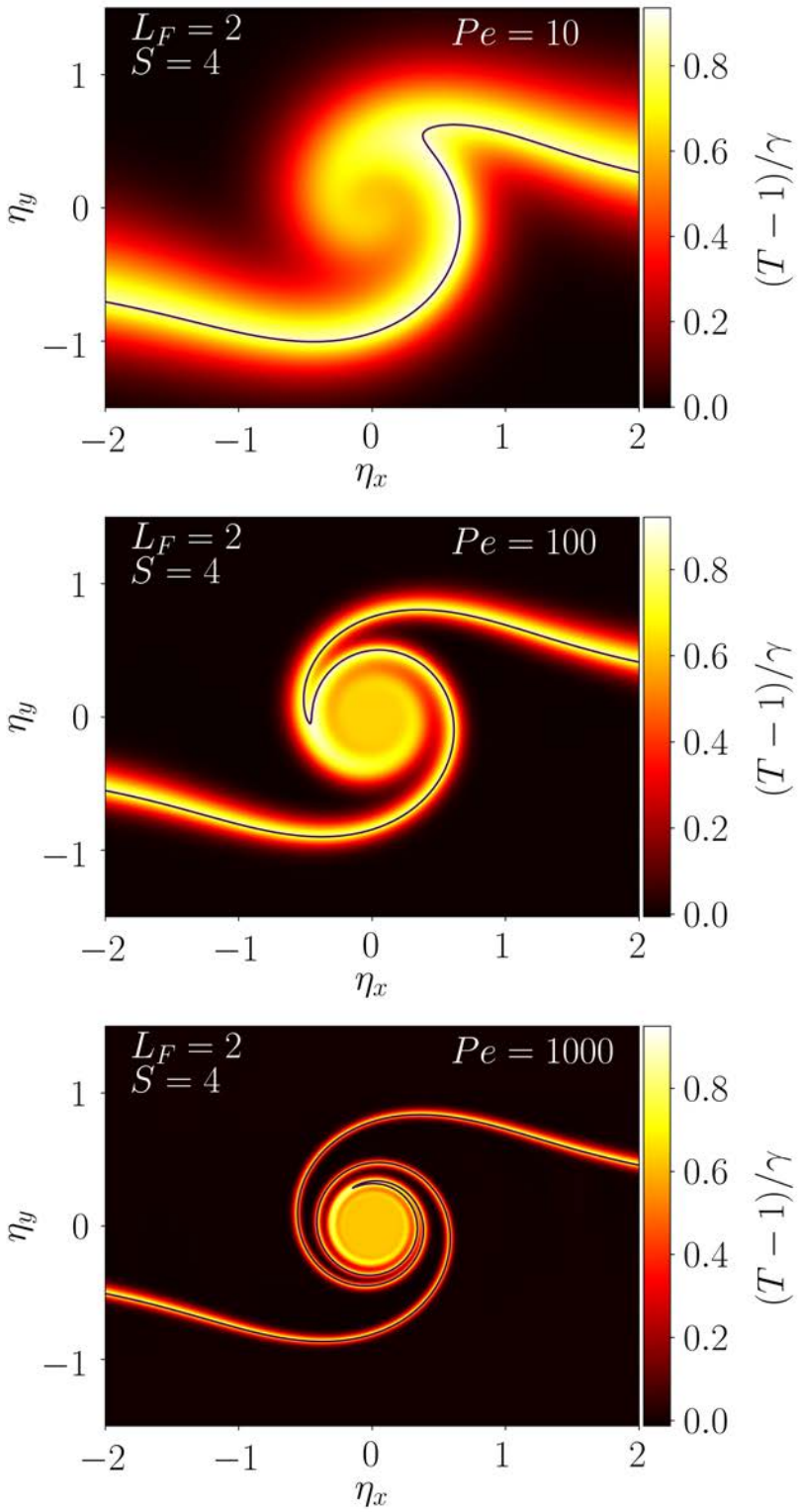

Fig. 4.5 Numerical solution of the vortex problem obtained using the LoMaHZ branch for $Pe = 10$,100 and 1000. Showing the temperature increment with respect of the adiabatic temperature normalized with γ for the case $L_F = 2$ and $S = 4$. Black lines represent the flame position. $\eta_x = x/\sqrt{t}$, $\eta_y = y/\sqrt{t}$, with t the simulation time.

the coordinate θ by $\mu = \theta - \eta^{-2}$, reducing (4.40) and (4.41) to

$$-\frac{\eta}{2}\frac{\partial Z}{\partial \eta} = \frac{1}{PeL_m}\left[\left(\frac{4}{\eta^6}+\frac{1}{\eta^2}\right)\frac{\partial^2 \tilde{Z}}{\partial \mu^2}+\frac{4}{\eta^3}\frac{\partial^2 \tilde{Z}}{\partial \eta \partial \mu}-\frac{4}{\eta^3}\frac{\partial \tilde{Z}}{\partial \mu}+\frac{1}{\eta}\frac{\partial \tilde{Z}}{\partial \eta}+\frac{\partial^2 \tilde{Z}}{\partial \eta^2}\right], \tag{4.45}$$

$$-\frac{\eta}{2}\frac{\partial \xi}{\partial \eta} = \frac{1}{Pe}\left[\left(\frac{4}{\eta^6}+\frac{1}{\eta^2}\right)\frac{\partial^2 \xi}{\partial \mu^2}+\frac{4}{\eta^3}\frac{\partial^2 \xi}{\partial \eta \partial \mu}-\frac{4}{\eta^3}\frac{\partial \xi}{\partial \mu}+\frac{1}{\eta}\frac{\partial \xi}{\partial \eta}+\frac{\partial^2 \xi}{\partial \eta^2}\right]. \tag{4.46}$$

The solution must be 2π-periodic in μ, regular at $\eta = 0$, and such that $Z = \tilde{Z} = \xi = F(\mu)$ as $\eta \to \infty$, with

$$F(\mu) = \begin{cases} 1, & \text{for } 0 < \mu < \pi. \\ 0, & \text{for } 0 > \mu > -\pi. \end{cases} \tag{4.47}$$

as follows from (4.42). As can be seen, in the limit $Pe \to \infty$ the equations reduce to $\partial Z/\partial \eta = \partial \xi/\partial \eta = 0$, which can be integrated using the distribution (4.47) as $\eta \to \infty$ to give $Z = \xi = F(\mu)$.

Mixing is confined to thin layers located about $\mu = n\pi$ ($n = 0, \pm 1, \pm 2, ...$). The associated mixing-layer thickness $\delta\mu$, determined from (4.45) and (4.46) by the condition that the diffusion term be comparable to the convection term, increases for decreasing values of η. Since the dominant terms in the diffusion operator in (4.45) and (4.46) are those involving $\partial^2/\partial\mu^2$, a simple order-of-magnitude balance yields $\delta\mu \sim Pe^{-1/2}$ at the radial distances $\eta \sim 1$, increasing to values $\delta\mu \sim 1$ in the near-core region $\eta \sim Pe^{-1/6}$, where the neighboring mixing layers begin to overlap. This can be described rewriting (4.45) and (4.46) in terms of the apparent time

$$\tau = \frac{1}{Pe}\left(\frac{4}{3\eta^6}+\frac{1}{\eta^2}\right), \tag{4.48}$$

and discarding smaller terms in negative power of Pe to yield the pseudo-transient diffusion equations

$$\frac{\partial Z}{\partial \tau}-\frac{1}{L_m}\frac{\partial^2 \tilde{Z}}{\partial \mu^2} = \frac{\partial \xi}{\partial \tau}-\frac{\partial^2 \xi}{\partial \mu^2} = 0 \tag{4.49}$$

with initial condition $Z = \tilde{Z} = \xi = F(\mu)$ at $\tau = 0$ and boundary conditions

$$\frac{\partial Z}{\partial \mu} = \frac{\partial \tilde{Z}}{\partial \mu} = \frac{\partial \xi}{\partial \mu} = 0 \text{ at } \eta = \pm\frac{\pi}{2}, \tag{4.50}$$

the latter being consisten with the 2π-periodicity of the solution.

As can be inferred from (4.48), the temperature along the flame outside the vortex core (i.e. for values of the rescaled radial distance $\eta >> Pe^{-1/6}$) is obtained from the solution to (4.49) in the limit $\tau << 1$. Introducing the selfsimilar variable $\zeta = \mu/\sqrt{2\tau}$ reduces the problem to

$$\zeta\frac{\partial Z}{\partial \zeta} + \frac{1}{L_m}\frac{\partial^2 \tilde{Z}}{\partial \zeta^2} = \zeta\frac{\partial \xi}{\partial \zeta} - \frac{\partial^2 \xi}{\partial \zeta^2} = 0, \begin{cases} Z = \tilde{Z} = \xi = 0, & \text{as } \zeta \to -\infty. \\ Z = \tilde{Z} = \xi = 0, & \text{as } \zeta \to \infty \end{cases}, \tag{4.51}$$

which describes also counterflow flames in the approximation $F = \zeta$, as discussed above. Therefore, the temperature along the flame outside the mixing core remains equal to the counterflow value, determined implicitly by (4.28) and (4.29).

With this formulation, we can solve the problem much faster than with the complete formulation. Note that, we have reduced the problem to two 1D nonlinear diffusive equations, as shown in equation (4.49), with the boundary conditions defined in (4.50). Taking advantage of this, we will analyze the effect of the parameters S and L_F on the flame temperature.

In figure 4.6, the flame temperature expressed as $Z_S - \xi_f$ is shown as a function of τ for the cases of $L_F = 0.3$ and $L_F = 2$ for a range of values of S. The first check of our results can be done by comparing the temperature value at $\tau = 0$ with the results of the counterflow shown in fig. 4.2. We can see that the values match as expected.

It is interesting to observe that the flame temperature in the diffusion flame varies along itself, getting closer to the adiabatic value when the value of S goes to one.

On the other hand, we observe how the flame is always extinguished before for lower values of L_F. For example, in the case of $L_F = 2$ and $S = 4$, the flame is extinguished at $\tau_e = 1.65$, whereas for $L_F = 0.3$ and $S = 4$ we have $\tau_e = 0.45$. This is a consequence of the oxidizer running out before reaching the center of the vortex for $S > 1$.

However, the most interesting phenomena is found for $S < 1$. As it can be seen in figure 4.6, the flame temperature crosses the adiabatic limit, reaching subadiabatic temperatures for $L_F = 0.3$ and superadiabatic temperatures for $L_F = 2$. This behavior was not found on the previous one-dimensional flamelet models studied and requires special attention. In the inset of fig.4.6 it is shown the evolution of temperature profiles as a function of μ for $S = 0.5$ and $L_F = 0.3$; here we can see the transition of the temperature profiles, represented by

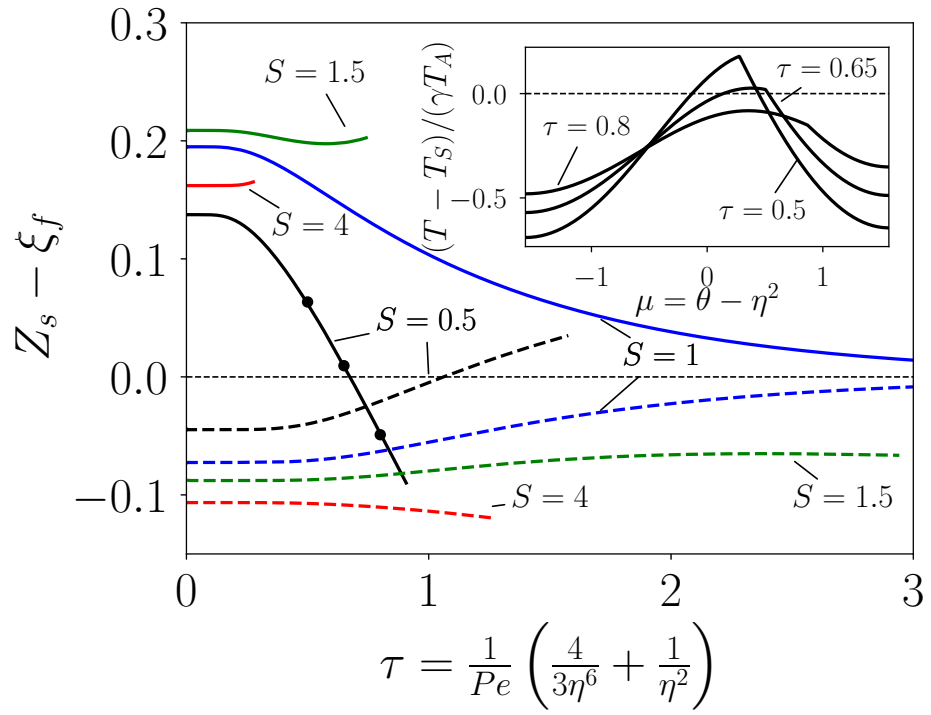

Fig. 4.6 Vortex results in the limit $Pe >> 1$, flame temperature $(Z_s - \xi_f)$ versus τ for different values of S. Continuous lines for $L_F = 0.3$ and dashed lines for $L_F = 2.0$. Dots represent the origin of inset view. Inset: temperature profile evolution as a function of μ for $S = 0.5$, $L_F = 0.3$

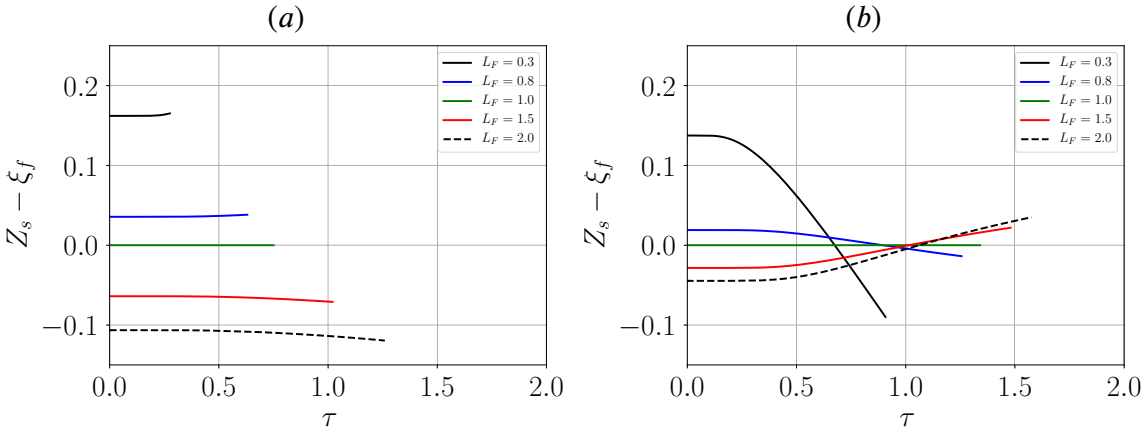

Fig. 4.7 Vortex problem results for the $Pe >> 1$ approximation, flame temperature $(Z_s - \xi_f)$ versus τ for different values of L_F. (a) Case $S = 4$, (b) case $S = 0.5$. Colors as: black: $L_F = 0.3$, blue: $L_F = 0.8$, green: $L_F = 1$, red: $L_F = 1.5$, dashed black: $L_F = 2$.

$(T(\mu) - T_S)/(\gamma T_A)$, from peak temperatures located at the flame and higher than the adiabatic temperature, to profiles where the peak temperature has been delocalized from the flame. To the best of our knowledge, this is the first time that this phenomena is observed.

In figure 4.7(a), the flame temperature as a function of τ is shown again, this time for $S = 4$ and a range of values of L_F. We observe here that the value of τ_e increases with L_F and the temperature along the flame does not change significantly in any of the cases shown. Nevertheless, this behavior changes abruptly when considering a the case $S < 1$; in figure 4.7(b), the flame temperature versus τ is shown for a range of values of L_F for $S = 0.5$. In this case, we can see that the changes in temperature along the flame are significant, shifting from subadiabatic/superadiabatic to superadiabatic/subadiabatic respectively as τ increases.

In order to discard that this variation of the temperature is an artifact of the approximation or an error on the computation, we have compared the results obtained by solving the full set of equations in 2D with the approximation for $Pe >> 1$. In figure 4.8 (a), the flame position for the two calculations is shown for the case of $L_F = 2$, $S = 0.5$. Here we can see that both solutions overlap for $Pe = 1000$ and $Pe = 100$ and differ for $Pe = 10$. It is not surprising that the results for low values of Pe using the $Pe >> 1$ approximation diverge. However, even in this case we can see that the flame position predicted by the approximation is very similar to the exact solution. On the other hand, when analyzing the flame temperature value (by means of $Z_s - \xi_f$), as a function of η for the three different Peclet values, shown in figure 4.8 (b), we can see that the $Pe >> 1$ approximation predicts only one temperature value for each η, whereas the complete solution has two different branches as we approach to the vortex center $(\eta \to 0)$. As we can see in figure 4.8 (b), as the Peclet number increases, the

two branches tend to collapse; hence, in the limit of $Pe \to \infty$ we would likely recover the $Pe >> 1$ approximation solution.

As a final check, simulations for the complete problem have been carried out for $S = 0.5$, obtaining the same results shown in figure 4.7 (b) ($Pe >> 1$ limit).

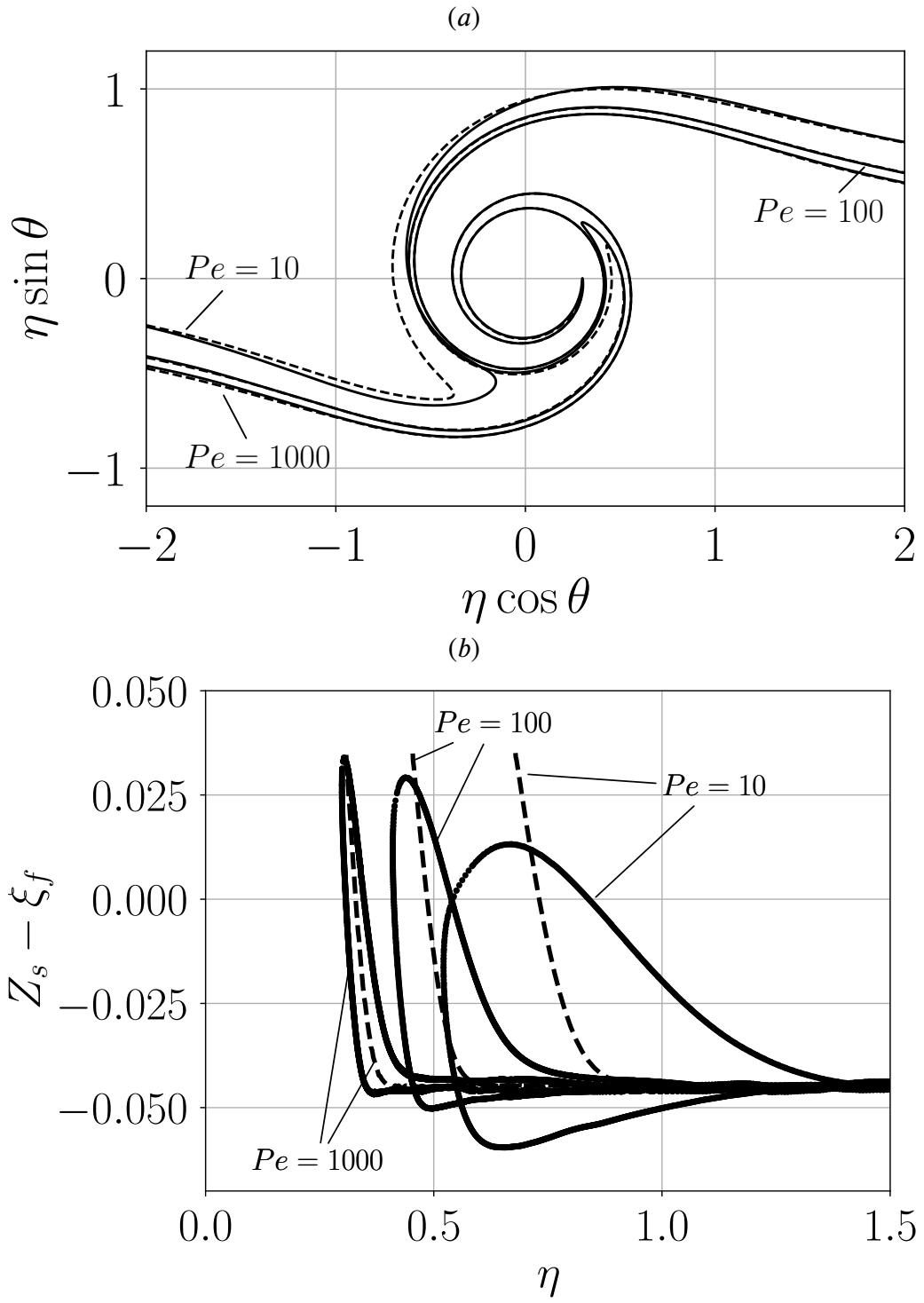

Fig. 4.8 Solution comparison for the vortex problem for $L_F = 2$ and $S = 0.5$: (a) Flame position $Z = Z_S$ for different values of Pe. (b) Flame temperature as a function of η. Continuous lines belong to the complete problem and dashed lines to the $Pe >> 1$ approximation.

4.6 Diffusion flame in turbulent flows

The previous results belong to the laminar regime. In the three cases analyzed so far, we have found that the flame temperature significantly varies when considering $L_F \neq 1$, with ranges depending on S, L_F and the problem of study. In this section, we want to extend this study to the three-dimensional case. For this purpose, several temporal turbulent mixing layer simulations have been carried out using LoMaHZ (see Chapter 2 for details on the code).

The simulations have been performed on a relatively small computational domain of ($11.5\delta_w^0$x $25\delta_w^0$ x $5.8\delta_w^0$), where δ_w^0 is the initial vorticity thickness of the mixing layer. The number of grid points in all the runs was (768 x 1001 x 384). The initial conditions are created similarly to the non-reactive case presented in Chapter 3. The initial Reynolds number, defined as $\mathrm{Re} = \rho_A \delta_w^0 \Delta U / \mu_A$ is 10000 for the cases of $L_F = 0.3$ and 8000 for the rest. This difference in the Reynolds number is due to the fact that lower values of L_F require higher Reynolds to promote the turbulent state.

Two cases of S, $S = 0.5$ and $S = 1$, are considered for $L_F = 0.3$ and $L_F = 2$, together with a reference case of $L_F = 1$ with $S = 4$. In all the cases we have used $\gamma = 4$, therefore $T_s = 5$. In figures 4.9 (a) and 4.9 (b), the temporal evolution of vorticity thickness δ_w/δ_w^0 and the integrated turbulent energy dissipation rate (see eq. (3.7)) respectively, are shown. As seen in figure 4.9(a), after a transient the vorticity thickness starts to increase linearly, reaching values between $1.5\delta_w^0$ and 2.5 δ_w^0 at the end of the simulations. The noisy results are due to the small computational domain and the fact that the definition of δ_w is based on the derivative of the mean streamwise velocity profile. On the other hand, the integrated turbulent energy dissipation rate $\zeta/\Delta U^3$ reaches a peak in all the cases at dimensionless times between 15 $t\delta_w^0/\Delta U$ for the $L_F = 1$ case, and 23 $t\delta_w^0/\Delta U$ for the case $L_F = 2$ and $S = 1$.

For the purpose of this study, we want to obtain a fully developed turbulent flow to be used as a framework to investigate 3D effects on diffusion flames. As a reference, the Re_λ obtained at the end of the simulations ranges between 90 and 120, therefore we can assume that the flow has reached a turbulent regime.

In figures 4.10 (a) and 4.10 (b), the mean density profiles and mean streamwise profiles are shown for all the cases under consideration; note that these mean profiles have been obtained at the end of the simulations. As a reference, we include in fig. 4.10 (a), the results for a compressible mixing layer ($M \approx 0.7$) obtained by Pantano, Sarkar and Williams [51] for their case B, with a heat release similar to our case ($\gamma = 4$). This profile lies somehow close to our results for $L_F = 1$ considering the differences in the formulation and the flow considered. Moreover, we can see that the mean density peaks of all the cases simulated are

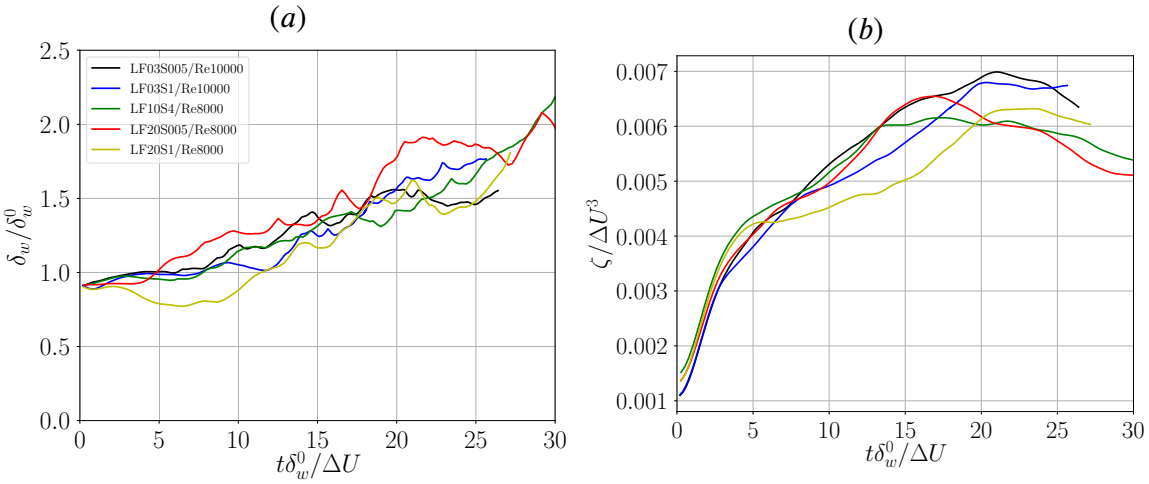

Fig. 4.9 (*a*) Temporal evolution of the vorticity thickness δ_w/δ_w^0 and (*b*) integrated turbulent energy dissipation rate. Black line: $L_F = 0.3$, $S = 0.5$, blue line: $L_F = 0.3$, $S = 1$, green line: $L_F = 1$, $S = 4.0$, red line: $L_F = 2$, $S = 0.5$, yellow line: $L_F = 2$, $S = 1$.

found at different y/δ_w depending on the values of S and L_F. However, these differences are less obvious for the mean streamwise velocity profiles shown in figure 4.10 (b).

Regarding the scalar variance of $\tilde{Z}$, as shown in 4.11 (a), we find a very different distribution for each case. First, in terms of L_F, the cases of $L_F = 0.3$ show a clear shifting towards the fuel side (negative values of y), with an additional contribution from S (with small values of S shifting even more to the fuel side), whereas the shifting is less obvious for $L_F = 2$ for the small values of S considered. However, the impact on the peak value of the scalar variance seems bigger for $L_F = 2$ than $L_F = 0.3$. Finally, for $L_F = 1$ we observe a reasonable agreement with the compressible flow.

When analyzing the integrated turbulent energy dissipation rate, see figure 4.11 (b), all the profiles collapse about the middle of the mixing layer, with no apparent shifting between the profiles, and significant differences in the peak value depending on both parameters S and L_F.

In figures 4.12, 4.13 and 4.14, 4.15 some visualizations of $\tilde{Z}$ and T in a xy plane are shown for the cases of $L_F = 0.3$ and $L_F = 2$ respectively. From these visualizations, we can confirm the turbulent state of the flow, with a flame already corrugated in all the cases. Even though coherent structures are hardly distinguishable in these visualizations, we can still detect two different rolls in the temperature field for both cases of $L_F = 2$, see figure 4.15, and for $L_F = 0.3$ with $S = 0.5$, see figure 4.13 (a). However, in the case of $L_F = 0.3$ with $S = 1$, see figure 4.13 (b), the rolls are not visually detectable. The reason of this

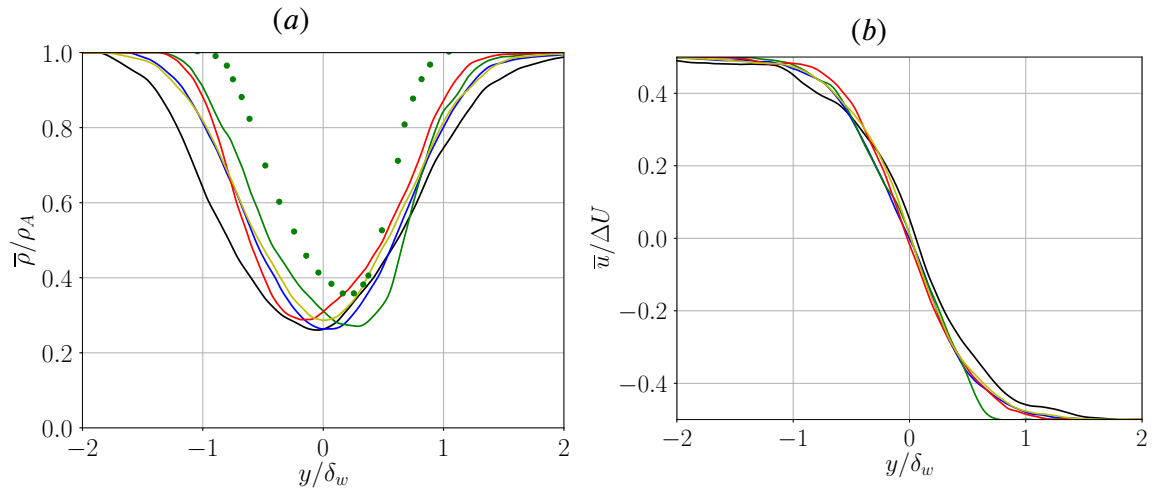

Fig. 4.10 (*a*) Mean density profiles and (*b*) mean velocity profiles for the different cases of study. Green dots: case B from Pantano et al. [51] for $M \approx 0.7$ and $\gamma \approx 4$. Black line: $L_F = 0.3$, $S = 0.5$, blue line: $L_F = 0.3$, $S = 1$, green line: $L_F = 1$, $S = 4$, red line: $L_F = 2$, $S = 0.5$, yellow line: $L_F = 2$, $S = 1$.

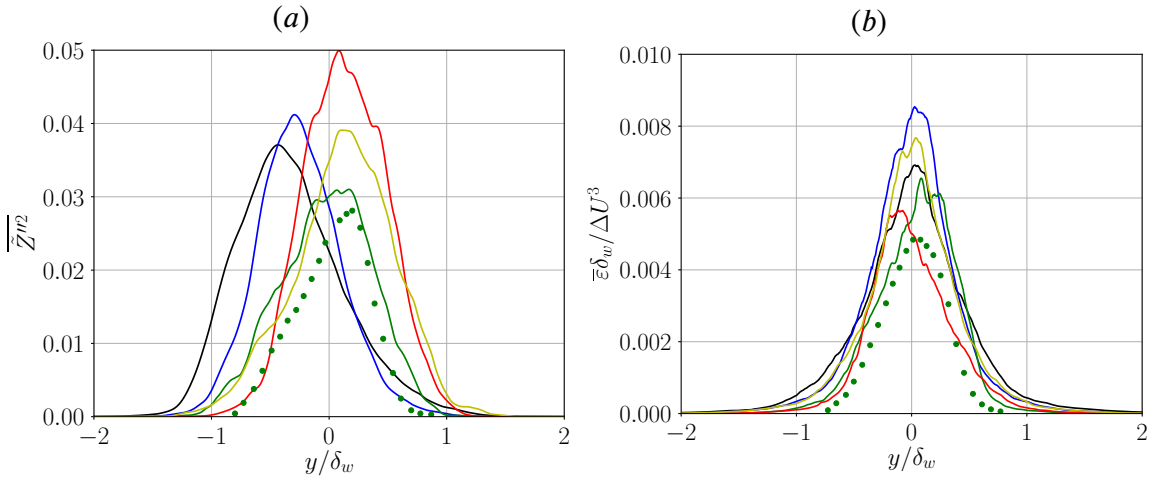

Fig. 4.11 (*a*) Scalar variance of $\tilde{Z}$ and (*b*) turbulent energy dissipation rate profiles for the different cases of study. Green dots: case B from Pantano et al. [51] for $M \approx 0.7$ and $\gamma \approx 4$. Black line: $L_F = 0.3$, $S = 0.5$, blue line: $L_F = 0.3$, $S = 1$, green line: $L_F = 1$, $S = 4$, red line: $L_F = 2$, $S = 0.5$, yellow line: $L_F = 2$, $S = 1$.

discrepancy is not clear, but it may be just an artifact due to the small computational domain used.

Even though the flame shape and position look similar in all the cases, closer examination will reveal an uneven distribution of the $\tilde{Z}$ scalar regarding S and L_F. This can be observed more clearly by means of the conditional average temperature obtained as a function of $\tilde{Z}$, as shown in figure 4.16. Here we can see very different temperature distributions depending on S and L_F. Although the conditional average temperature peak is similar for all the cases of study and close to the adiabatic flame temperature ($T_S = 5$), the ranges of these temperatures (shown by means of dotted lines representing minimum and maximum temperatures) are very different. For example, the flame temperature variations for the cases $L_F = 2$, represented by red and yellow lines, are significantly smaller than for the cases of $L_F = 0.3$. Note that for $L_F = 1$ the three lines (minimum, average and maximum) collapse as expected.

On the other hand, the results shown in figure 4.16 imply that, for the turbulent case considering preferential diffusion, it is possible to find temperatures in the outer region higher than the average flame temperature.

Focusing now on the flame temperature distribution, we proceed to obtain the temperature value at all points within the flame surface Σ_f. In figure 4.17, the probability density function (p.d.f.) of the temperature (in terms of $Z_S - \xi_f$) is shown for all the cases considered. Note that, this p.d.f. would give the probability of finding a point on the flame within a given temperature interval, as the area below the curve within that interval. First of all, the vertical line shown at $Z_S - \xi_f = 0$ would represent the flame temperature for all the points for the case $L_F = 1$, separating between subadiabatic and superadiabatic regions. Moreover, we observe that for $L_F = 0.3$, a significant number of points are located within the the subadiabatic region. These results are in accordance with the result found for the vortex flow, obtaining subadiabatic (superadiabatic) temperatures for $L_F < 1$ ($L_F > 1$). Nevertheless, we can see that, as a result of the turbulent transport, even for the case of $S = 1$ we find a significant number of points crossing the adiabatic temperature limit. Note that this behavior was not found previously in the vortex flow analysis (laminar regime).

All the analysis provided so far were done under the assumption that we could find some similarities on the flame temperature distribution between the simple canonical flamelet models and the more complex 3D case of turbulent flow. In fact, we are trying to analyze the turbulent (complex) flow as a composition of regions behaving as coflow with different velocity ratios, plus regions more similar to a counterflow configuration or vortex flow configuration. On top of this, we should consider the turbulent transport effect not found in the laminar flamelet models.

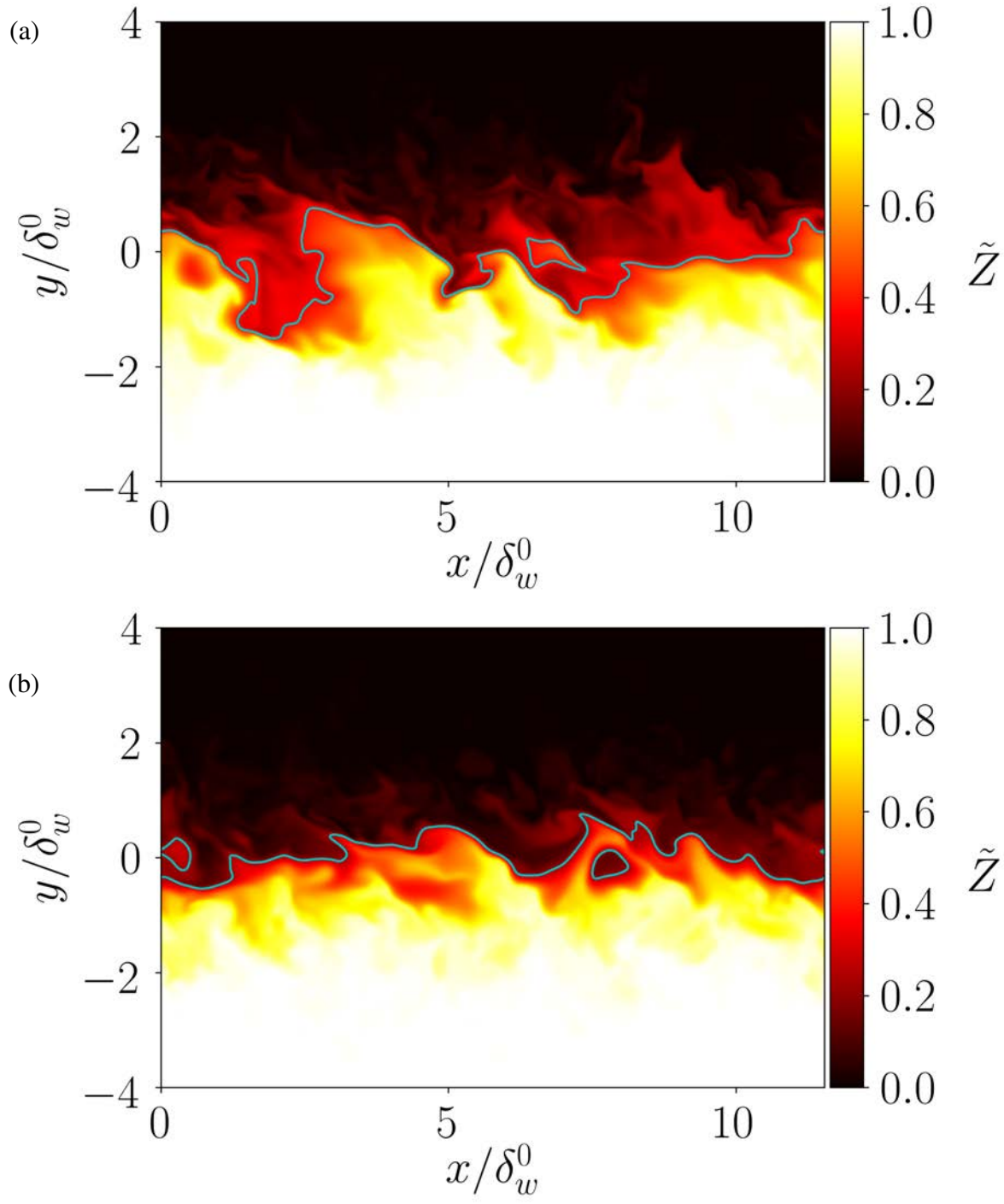

Fig. 4.12 Field visualization of $\tilde{Z}$ at the first yx plane for the cases of $L_F = 0.3$: (*a*) $S = 0.5$, (*b*) $S = 1$. Contour representing $\tilde{Z} = \tilde{Z}_S$.

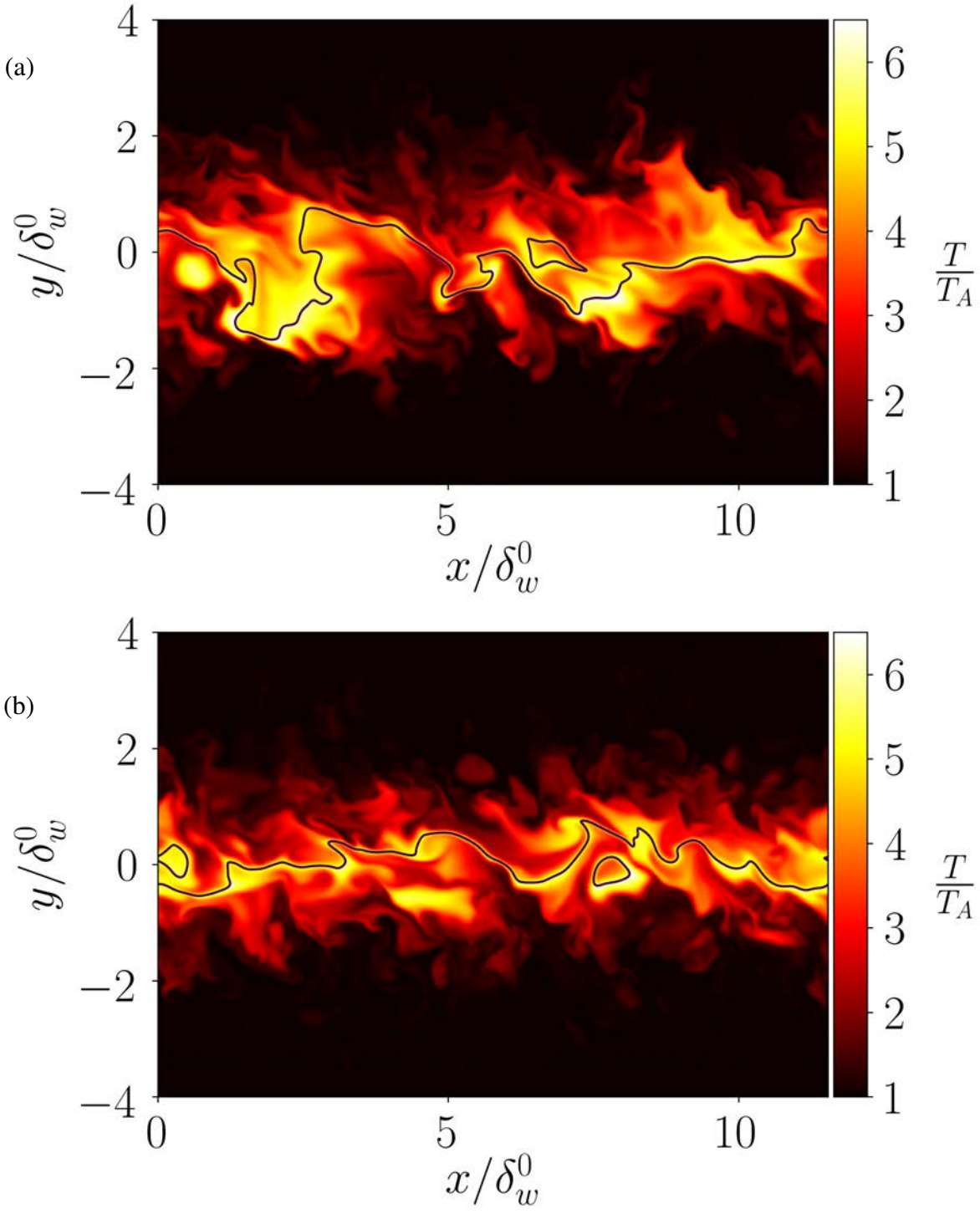

Fig. 4.13 Temperature field visualization at the first yx plane for the cases of $L_F = 0.3$: (a) $S = 0.5$, (b) $S = 1$. Contour representing $\tilde{Z} = \tilde{Z}_S$.

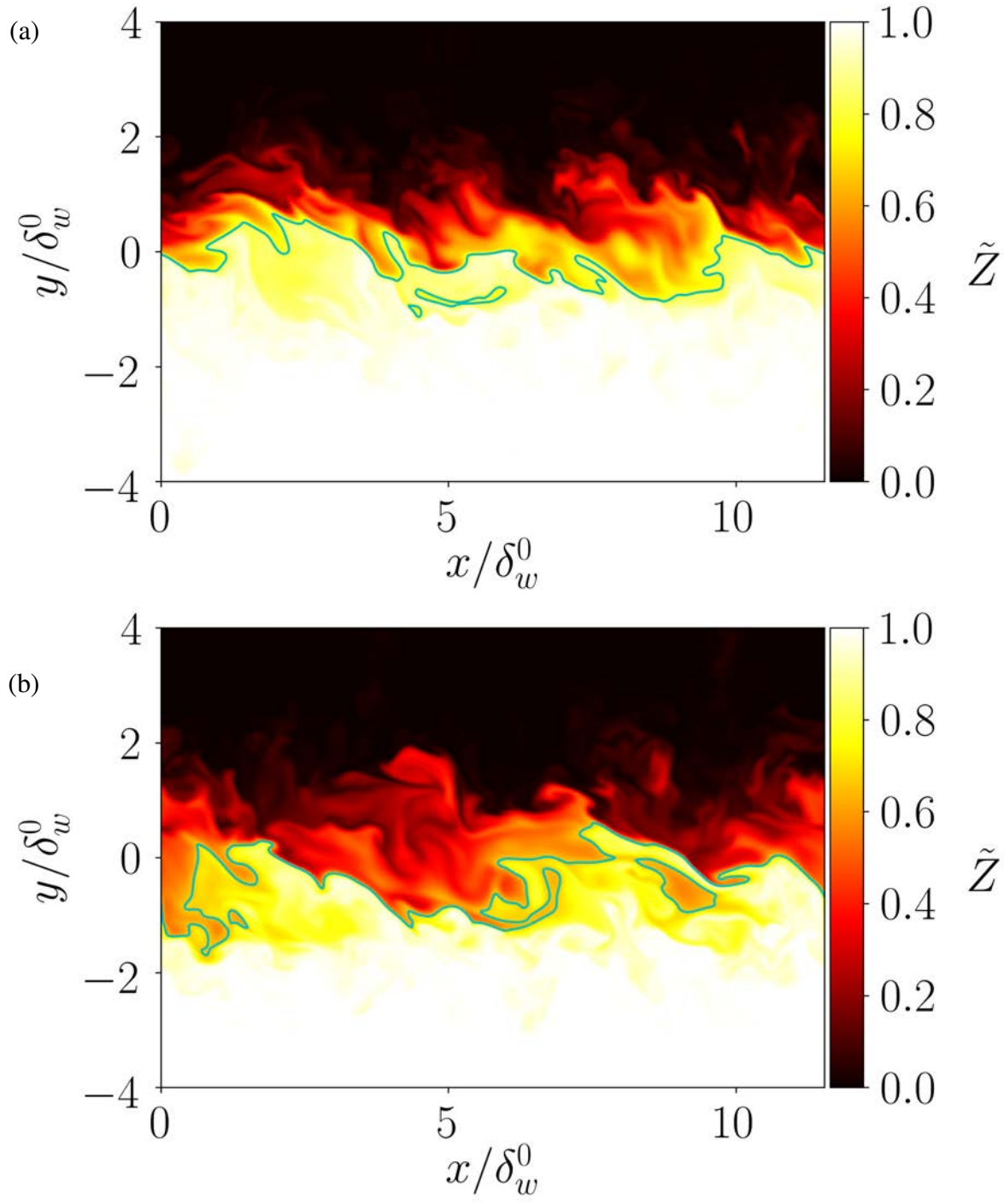

Fig. 4.14 Field visualization of $\tilde{Z}$ at the first yx plane for the cases of $L_F = 2$: (*a*) $S = 0.5$, (*b*) $S = 1$. Contour representing $\tilde{Z} = \tilde{Z}_S$.

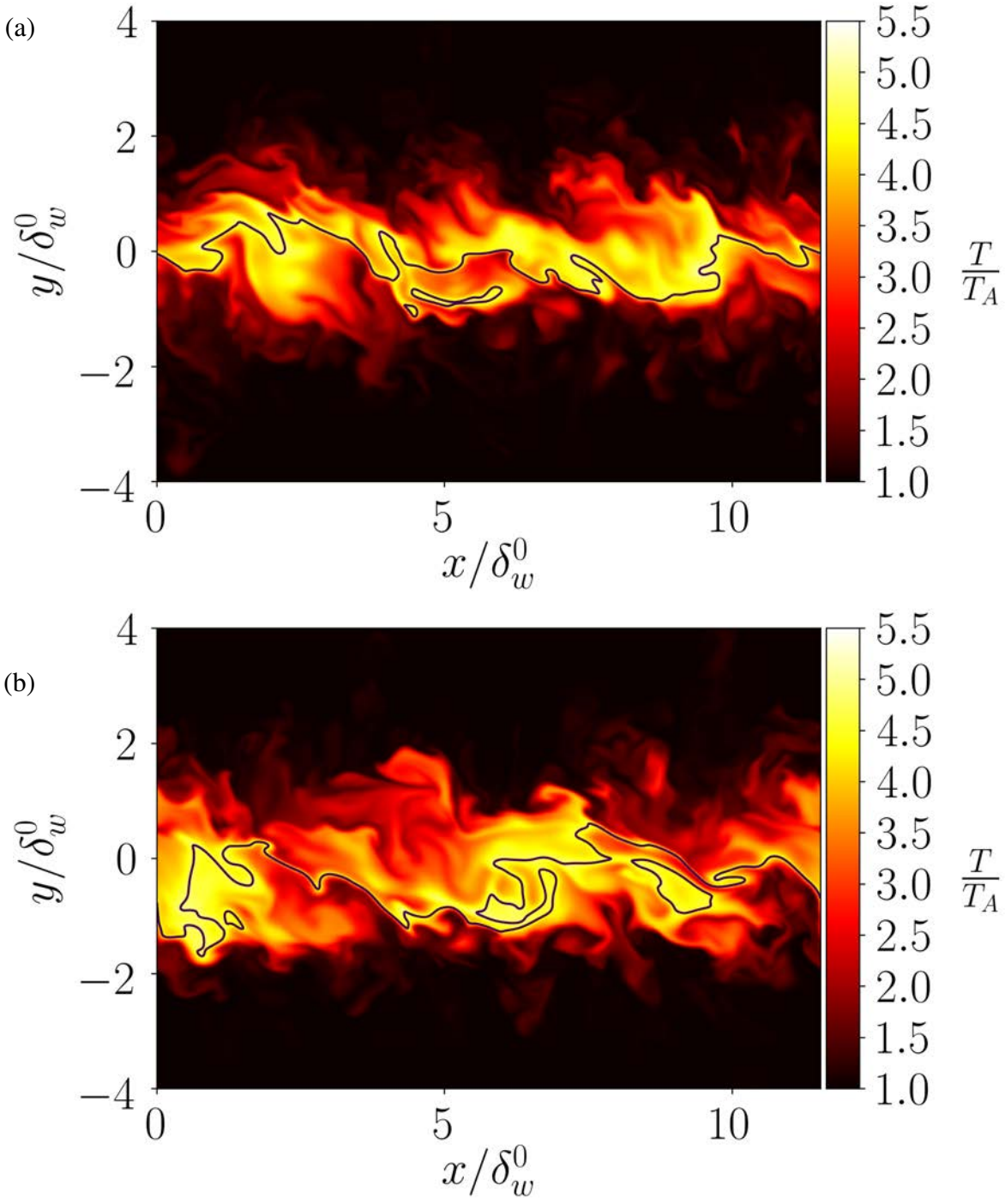

Fig. 4.15 Temperature field visualization at the first yx plane for the cases of $L_F = 2$: (a) $S = 0.5$, (b) $S = 1$. Contour representing $\tilde{Z} = \tilde{Z}_S$.

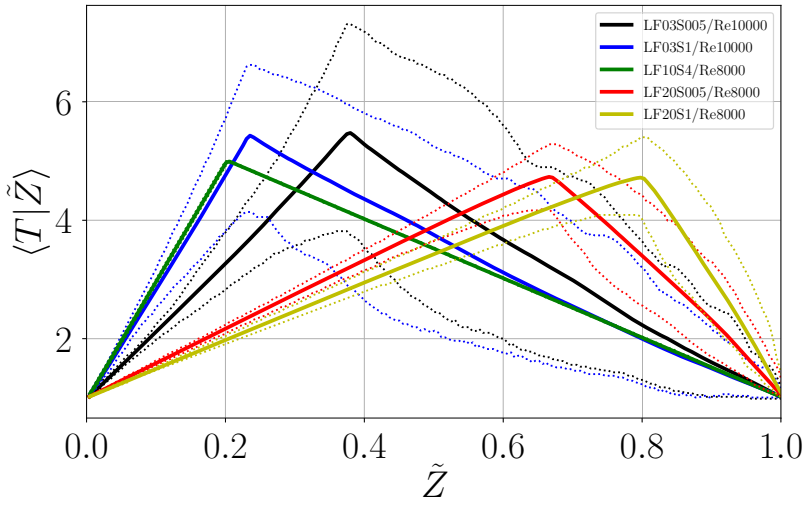

Fig. 4.16 Conditional average temperature as a function of the mixture fraction at the end of the simulations. Dotted lines represent minimum and maximum temperatures found in the field for each case.

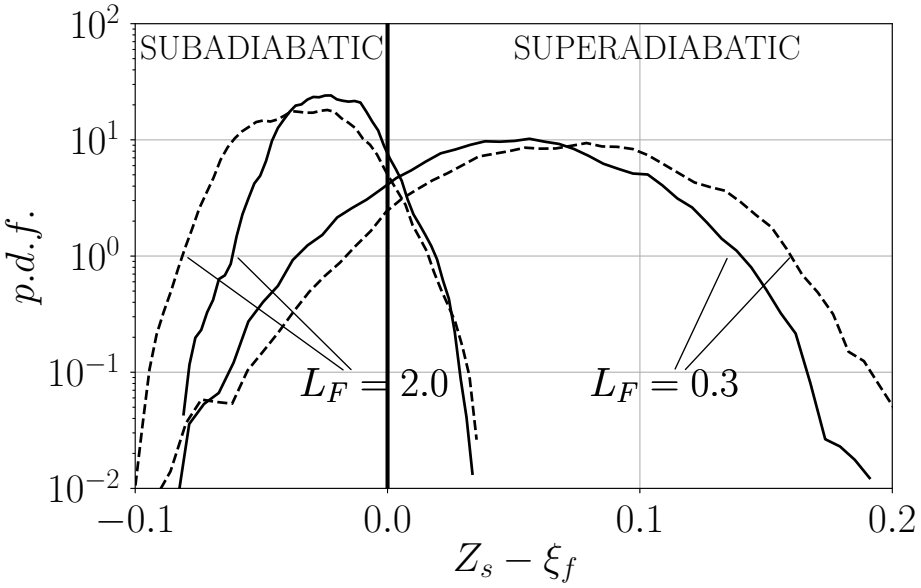

Fig. 4.17 Probability density function of $Z_S - \xi_f$ on the flame for the different turbulent cases. Dashed lines for $S = 0.5$, continuous lines for $S = 1$.

Table 4.1 Summary of flame temperature ranges obtained for coflow, vortex flow ($Pe >> 1$) and turbulent flow.

		$Z_S - \xi_f$					
Case		**Coflow**		**Vortex flow**		**Turbulent flow**	
L_F	S	Min.	Max.	Min.	Max.	Min.	Max.
0.3	0.5	0.03	0.2	-0.08	0.14	-0.08	0.18
	1.0	0.07	0.3	0.0	0.19	-0.08	0.2
2.0	0.5	-0.06	-0.01	-0.04	0.03	-0.08	0.03
	1.0	-0.1	-0.03	-0.08	0.0	-0.10	0.03

In order to check how this hypothesis stands, we have collected the results from all the cases studied. Namely, we will consider the minimum and maximum flame temperature obtained for: coflow (considering the two extremes $U_0/U_A = 0$ and $U_0/U_A = \infty$), vortex flow ($Pe >> 1$ approximation), and turbulent mixing layers. These results are presented in table 4.1. Focusing on the atypical behavior of $S = 0.5$, as mentioned before, the 1D flamelet models do not predict the negative (positive) values on $Z_S - \xi_f$ peak temperatures for $L_F = 0.3$ ($L_F = 2$), found both in the vortex and the turbulent flow cases. Furthermore, the flame temperature range in the turbulent case seems to be approximately bounded by the overlapping of the coflow and the vortex flow results.

On the other hand, as mentioned above, for $S = 1$ the turbulent flow crosses the adiabatic limit for the two different L_F considered, despite the fact that this was not predicted by any of the canonical solutions considered. This effect should be the result of the turbulent transport processes (not modeled by laminar flow cases).

4.7 Conclusions

The effects of fuel Lewis number and dilution have been investigated for different combustion problems. Steady one-dimensional self-similar counterflow and coflow configurations were considered first. As expected, for these canonical flamelet models, superadiabatic temperatures are always found for $L_F < 1$, whereas subadiabatic temperatures are found for $L_F > 1$. However, it has been found that peak temperatures not always lie between the adiabatic flame temperature and the peak temperature of diffusion-reaction systems, instead this condition depends on the value of Z_S. For the coflow configuration, it is seen that a larger velocity of the fuel stream enhances differential-diffusion effects on flame temperature, both for $L_F = 0.3$ and $L_F = 2.0$. Also of interest is that when the two streams have the same velocity the resulting peak temperature is not very different from that of the counterflow. One question not addressed in this topic is why $T_d > T_f$ for sufficiently large values of Z_S.

A time-dependent planar diffusion flame distorted by a vortex, equivalent to a three-dimension steady vortex flame in a stretched field, was also investigated. The Marble's problem was solved both numerically by brute force (using a vortex with a viscous core to avoid singularities), and by means of a reduced problem in the limit of $Pe >> 1$. It was shown that both solutions match very well for sufficiently high Pe, proven that this approximation could be used to predict the temperature on the flame surface as a function of the variables (μ, τ). This approach allowed us to perform a parametric study on the solution of the vortex flame for different values of S and L_F. We have found an atypical behavior on the flame temperatures for the cases of $S < 1$ independently of the value of L_F, obtaining superadiabatic (subadiabatic) flame temperatures for $L_F > 1$ ($L_F < 1$).

By analyzing 3D simulations of turbulent temporal mixing layer with $L_F \neq 1$, we have shown that the flame temperature significantly varies along the flame surface. For the cases of study, we have shown how the 1D and 2D diffusion flame problems considered could give a very good approximation of the flame temperature ranges found on complex three-dimensional flows. Nevertheless, we have seen that turbulent transport could lead to subadiabatic and superadiabatic temperatures independently of the value of L_F provided that S is not far from 1.

Chapter 5

Conclusions and outlook

In this work, DNS of reacting and non-reacting, temporally evolving, turbulent shear layers in the low-Mach number limit have been performed. Two main numerical tools were developed for this purpose: LoMa and LoMaHZ.

For the non-reacting case, the DNS have been done for four different density ratio values $s = 1$, 2, 4 and 8, reaching a self-similar evolution. The mixing layer growth rate has been characterized and modeled as a function of the density ratio, showing that the ratio between the growth rate for large density ratios and the growth rate of the $s = 1$ is almost independent of the flow speed. Furthermore, a semi-empirical prediction of the reduction of the momentum thickness growth rate with s has been obtained. Moreover, the shifting on the Favre-averaged velocity profiles with the density ratio has been quantified, obtaining an empirical relation with s. One interesting possibility for future work would be to extend the analysis to higher density ratios and check the validity of the models developed for the growth rate reduction and the shifting of the mixing layer. Finally, the flow structures have been analyzed, showing that with increasing density ratio there is a shift towards the low density side and the longest scales in the high density side are gradually inhibited.

The reacting, temporally evolving, turbulent mixing layer simulations were performed to analyze the flame temperature distribution of the more realistic case of fuel Lewis number different to unity. By means of 1D and 2D flamelet models analysis, a framework was created to better understand the influence of the transport processes on the flame temperature. This framework proved to be valid for an estimation of the flame temperature boundaries of turbulent combustions. The results suggest that even during a full turbulent regime, we could assume that there are regions of the flame similar to a coflow or counterflow configuration and some others similar to vortex flow, whereas the rest could be seen as the result of turbulent transport.

In most of the turbulent DNS on the literature, two very common assumptions are $L_F = 1$ (used to simplify the equations) and $S \approx 4$ (used to avoid numerical integration problems related to high values of S). In this work, it has been shown how the flame temperature significantly varies when considering preferential diffusion and the important role of the fuel dilution S, affecting the temperature distribution not only quantitatively but also qualitatively (crossing the adiabatic flame limit). Thus, we have shown how neglecting the preferential diffusion effects could lead to a wrong prediction on the flame temperature for engineering applications, therefore to a bad prediction on the pollutants produced on the combustion.

Following this research, the next step would be to find a metric (for instance, using velocity gradient or strain tensor invariants) in order to map regions within the turbulent flow with the canonical solutions described in this work (coflow, counterflow or vortex flow). Finally, it would be interesting to extend the turbulent database results for $L_F = 0.3$ and $L_F = 2.0$ considering more realistic values of S (e.g. $S = 18, 32...$), using large computational domains in order to extract relevant statistics that could feed industry application models considering differential diffusion effects.

Conclusiones y previsión

En este trabajo se ha realizado DNS (Simulación Numérica Directa) de capas turbulentas de cizalladura, reactivas, y no reactivas, que evolucionan con el tiempo. Para este propósito, se han desarrollado principalmente dos herramientas: LoMa y LoMaZH. Para el caso no reactivo, la DNS se ha realizado para cuatro valores diferentes de ratios de densidad $s = 1$, 2, 4 y 8, alcanzando una evolución auto similar. La tasa de crecimiento de la capa de mezcla se ha caracterizado y modelado en función del ratio de densidad, mostrando que el ratio entre la tasa de crecimiento para ratios de densidad altos y la tasa crecimiento de s = 1 son prácticamente independientes de la velocidad de flujo. Asimismo, se ha obtenido una prediction semi-empírica de la reducción de la tasa de crecimiento del espesor de momento con s. Además, se ha cuantificado el desplazamiento en los perfiles de velocidad "Favre promediado" con el ratio de densidad, obteniendo una relación empírica con s. Una posibilidad interesante para trabajos futuros sería extender el análisis a ratios de densidad mayores y chequear la validez de los modelos desarrollados para la reducción de la tasa de crecimiento y el desplazamiento de la capa de mezcla. Finalmente, se han analizado las estructuras de los flujos, mostrando que cuando se incrementa el ratio de densidad se produce un desplazamiento hacia la parte de densidad baja y las escalas más largas en el lado de alta densidad se inhiben gradualmente. Las simulaciones de capa de mezcla temporal turbulenta reactiva, se realizaron para analizar la distribución de la temperatura de la llama en el caso más realista de número de Lewis de fuel diferente a la unidad. Por medio del análisis de los modelos de llama 1D y 2D, se creó un borrador para entender mejor la influencia de los procesos de transporte en la temperatura de la llama. Este borrador probó ser válido para la estimación de los límites de la temperatura de la llama en combustiones turbulentas. Los resultados sugieren que incluso durante un regimen turbulento completo, podríamos asumir que hay regiones de la llama similares a las configuraciones de coflow (flujos desplazándose en el mismo sentido) o counterflow (flujos desplazándose en sentidos opuestos), otras similares al flujo de los vórtices, mientras el resto se podría ver como resultado del transporte turbulento. En la mayoría de los casos de DNS turbulenta en literatura se encuentran dos suposiciones comunes que son $L_F = 1$ (usada para simplificar las ecuaciones) y $S \approx 5$ (usada para evitar

problemas de integración numérica relacionados con valores altos de S). En este trabajo se ha mostrado cómo la temperatura de la llama varía de forma significativa cuando se consideran difusión preferencial, así como la importancia del papel de la disolución de fuel S, afectando la distribución de temperatura no sólo cuantitativamente, sino también cualitativamente (cruzando el límite adiabático de llama). De este modo, se ha probado cómo ignorar los efectos de la difusión preferencial podría conducir a una predicción errónea de la temperatura de la llama para aplicaciones en ingeniería y, por tanto, a una mala predicción de los contaminantes producidos durante la combustión.

Continuando con esta investigación, el siguiente paso sería encontrar una métrica (por ejemplo los invariantes del tensor de velocidad o de deformación) con la que relacionar las regiones del flujo turbulento con las soluciones canónicas descritas en este trabajo (coflow, counterflow, o vórtice 2D). Por último, sería interesante extender los resultados de la base de datos turbulenta para $L_F = 0.3$ y $L_F = 2.0$ considerando valores más realistas de S (p.ej. $S = 18, 32...$).

References

[1] Almagro, A., García-Villalba, M., and Flores, O. (2017). A numerical study of a variable-density low-speed turbulent mixing layer. *Journal of Fluid Mechanics*, 830:569–601.

[2] Ashurst, WM. M T., P. N. and Smooke, M. D. (1987). Numerical Simulation of Turbulent Flame Structure with Non-unity Lewis Number. *Combustion Science and Technology*, 53(4-6):339–375.

[3] Ashurst, W. T. and Kerstein, A. R. (2005). One-dimensional turbulence: Variable-density formulation and application to mixing layers. *Phys. Fluids*, 17:025107.

[4] Attili, A., Bisetti, F., Mueller, M. E., and Pitsch, H. (2016). Effects of non-unity Lewis number of gas-phase species in turbulent nonpremixed sooting flames. *Combustion and Flame*, 166:192–202.

[5] Barlow, R. S., Frank, J. H., Karpetis, A. N., and Chen, J. Y. (2005). Piloted methane/air jet flames: Transport effects and aspects of scalar structure. *Combustion and Flame*, 143(4):433–449.

[6] Bell, J. H. and Mehta, R. D. (1990). Development of a two-stream mixing layer from tripped and untripped boundary layers. *AIAA J.*, 28(12):2034–2042.

[7] Bogdanoff, D. W. (1983). Compressibility effects in turbulent shear layers. *AIAA J.*, 21(6):926–927.

[8] Bretonnet, L., Cazalbou, J.-B., Chassaing, P., and Braza, M. (2007). Deflection, drift, and advective growth in variable-density, laminar mixing layers. *Phys. Fluids*, 19(10):103601.

[9] Brown, G. L. (1974). The entrainment and large structure in turbulent mixing layers. In *Proc. 54th Australasian Conf. Hydraulics and Fluid Mech.*, pages 352–359.

[10] Brown, G. L. and Roshko, A. (1974). On density effects and large structure in turbulent mixing layers. *J. Fluid Mech.*, 64(4):775–816.

[11] Carlier, J. and Sodjavi, K. (2016). Turbulent mixing and entrainment in a stratified horizontal plane shear layer: joint velocity-temperature analysis of experimental data. *J. Fluid Mech.*, 806:542–579.

[12] Chaos, M., C. R.-H. W. E. J. and Roberts, W. (2004). Fuel Lewis number effects in unsteady Burke–Schumann hydrogen flames. *Combustion Science and Technology*, 177(1):75–88.

[13] Chassaing, P., Antonia, R. A., Anselmet, F., Joly, L., and Sarkar, S. (2002). *Variable density fluid turbulence*. Springer.

[14] Chen, Y. C. and Chen, J. Y. (1998). Fuel-dilution effect on differential molecular diffusion in laminar hydrogen diffusion flames. *Combustion Theory and Modelling*, 2(4):497–514.

[15] Clemens, N. T. and Mungal, M. G. (1992). Two-and three-dimensional effects in the supersonic mixing layer. *AIAA J.*, 30(4):973–981.

[16] Cook, A. W. and Riley, J. J. (1996). Direct numerical simulation of a turbulent reactive plume on a parallel computer. *J. Comput. Phys.*, 129(2):263–283.

[17] da Silva, C. and Pereira, J. (2008a). Invariants of the velocity-gradient, rate-of-strain, and rate-of-rotation tensors across the turbulent/nonturbulent interface in jets. *Phys. Fluids*, 20(5):055101.

[18] da Silva, C. B. and Pereira, J. C. F. (2008b). Invariants of the velocity-gradient, rate-of-strain, and rate-of-rotation tensors across the turbulent/nonturbulent interface in jets. *Physics of Fluids*, 20(5):055101.

[19] Dimotakis, P. E. (1986). Two-dimensional shear-layer entrainment. *AIAA J.*, 24(11):1791–1796.

[20] Dimotakis, P. E. (1991). Turbulent free shear layer mixing and combustion. *High Speed Flight Propulsion Systems*, 137:265–340.

[21] Dimotakis, P. E. (2005). Turbulent Mixing. *Annu. Rev. Fluid Mech.*, 37(1):329–356.

[22] Dimotakis, P. E. and Brown, G. L. (1976). The mixing layer at high reynolds number: large-structure dynamics and entrainment. *Journal of Fluid Mechanics*, 78(3):535–560.

[23] Driscoll, T., Bornemann, F., and Trefethen, L. (2008). The chebop system for automatic solution of differential equations. *BIT Num. Math.*, 48(4):701–723.

[24] Flores, O. and Jiménez, J. (2006). Effect of wall-boundary disturbances on turbulent channel flows. *J. Fluid Mech.*, 566:357–376.

[25] Fontane, J. and Joly, L. (2008). The stability of the variable-density Kelvin–Helmholtz billow. *J. Fluid Mech.*, 612:237–260.

[26] Gatski, T. B. and Bonnet, J.-P. (2013). *Compressibility, turbulence and high speed flow*. Academic Press.

[27] Hall, J. L., Dimotakis, P. E., and Rosemann, H. (1993). Experiments in nonreacting compressible shear layers. *AIAA J.*, 31(12):2247–2254.

[28] Han, C., Lignell, D. O., Hawkes, E. R., Chen, J. H., and Wang, H. (2016). Examination of the effect of differential molecular diffusion in DNS of turbulent non-premixed flames. *International Journal of Hydrogen Energy*, 42(16):11879–11892.

[29] Higuera, F. J. and Moser, R. D. (1994). Effect of chemical heat release in a temporally evolving mixing layer. *CTR Report*, pages 19–40.

[30] Hoyas, S. and Jiménez, J. (2006). Scaling of the velocity fluctuations in turbulent channels up to reτ= 2003. *Phys. Fluids*, 18(1):011702.

[31] Jahanbakhshi, R. and Madnia, C. K. (2016). Entrainment in a compressible turbulent shear layer. *J. Fluid Mech.*, 797:564–603.

[32] Jang, Y. and de Bruyn Kops, S. M. (2007). Pseudo-spectral numerical simulation of miscible fluids with a high density ratio. *Computers & Fluids*, 36(2):238–247.

[33] Jiang, J., Jiang, X., and Zhu, M. (2015). A computational study of preferential diffusion and scalar transport in nonpremixed hydrogen-air flames. *International Journal of Hydrogen Energy*, 40(45):15709–15722.

[34] Kim, J., Moin, P., and Moser, R. (1987). Turbulence statistics in fully developed channel flow at low Reynolds number. *J. Fluid Mech.*, 177:133–166.

[35] Klainerman, S. and Majda, A. (1982). Compressible and incompressible fluids. *Communications on Pure and Applied Mathematics*, 35(5):629–651.

[36] Knaus, R. and Pantano, C. (2009). On the effect of heat release in turbulence spectra of non-premixed reacting shear layers. *J. Fluid Mech.*, 626:67.

[37] Knio, O. M. and Ghoniem, A. F. (1992). The three-dimensional structure of periodic vorticity layers under non-symmetric conditions. *J. Fluid Mech.*, 243:353–392.

[38] Lele, S. K. (1992). Compact finite difference schemes with spectral-like resolution. *J. Comput. Phys.*, 103(1):16–42.

[39] Lele, S. K. (1994). Compressibility effects on turbulence. *Annu. Rev. Fluid Mech.*, 26(1):211–254.

[40] Liñán, A., Vera, M., and Sánchez, A. L. (2015). Ignition, Liftoff, and Extinction of Gaseous Diffusion Flames. *Annual Review of Fluid Mechanics*, 47(1):293–314.

[41] Mahle, I., Foysi, H., Sarkar, S., and Friedrich, R. (2007). On the turbulence structure in inert and reacting compressible mixing layers. *J. Fluid Mech.*, 593:171–180.

[42] Maragkos, G., Rauwoens, P., and Merci, B. (2015). Assessment of a methodology to include differential diffusion in numerical simulations of a turbulent flame. *International Journal of Hydrogen Energy*, 40(2):1212–1228.

[43] McMullan, W., Coats, C., and Gao, S. (2011). Analysis of the variable density mixing layer using large eddy simulation. In *41st AIAA Fluid Dynamics Conference and Exhibit*. AIAA 2011-3424.

[44] McMurtry, P. A., Jou, W.-H., Riley, J., and Metcalfe, R. W. (1986). Direct numerical simulations of a reacting mixing layer with chemical heat release. *AIAA J.*, 24(6):962–970.

[45] Mcmurtry, P. A., Riley, J. J., and Metcalfe, R. W. (1989). Effects of heat release on the large-scale structure in turbulent mixing layers. *J. Fluid Mech.*, 199:297–332.

[46] Moin, P. and Mahesh, K. (1998). Direct numerical simulation: a tool in turbulence research. *Annu. Rev. Fluid Mech.*, 30(1):539–578.

[47] Nicoud, F. (2000). Conservative high-order finite-difference schemes for low-Mach number flows. *J. Comput. Phys.*, 158(1):71–97.

[48] O'Brien, J., Urzay, J., Ihme, M., Moin, P., and Saghafian, A. (2014). Subgrid-scale backscatter in reacting and inert supersonic hydrogen–air turbulent mixing layers. *J. Fluid Mech.*, 743:554–584.

[49] Orszag, S. A. (1971). Accurate solution of the orr–sommerfeld stability equation. *Journal of Fluid Mechanics*, 50(4):689–703.

[50] Pantano, C. and Sarkar, S. (2002). A study of compressibility effects in the high-speed turbulent shear layer using direct simulation. *J. Fluid Mech.*, 451:329–371.

[51] Pantano, C., Sarkar, S., and Williams, F. A. (2003). Mixing of a conserved scalar in a turbulent reacting shear layer. *J. Fluid Mech.*, 481:291–328.

[52] Papamoschou, D. and Roshko, A. (1988). The compressible turbulent shear layer: an experimental study. *J. Fluid Mech.*, 197:453–477.

[53] Peters, N. (2000). *Turbulent combustion*. Cambridge Univ. Press.

[54] Pickett, L. and Ghandhi, J. (2001). Passive scalar measurements in a planar mixing layer by PLIF of acetone. *Exp. Fluids*, 31(3):309–318.

[55] Pouransari, Z., Vervisch, L., and Johansson, A. V. (2013). Heat release effects on mixing scales of non-premixed turbulent wall-jets: A direct numerical simulation study. *Int. J. Heat Fluid Flow*, 40:65–80.

[56] Ramshaw, J. D. (2000). Simple model for mixing at accelerated fluid interfaces with shear and compression. *Phys. Rev. E*, 61:5339–5344.

[57] Reinaud, J., Joly, L., and Chassaing, P. (2000). The baroclinic secondary instability of the two-dimensional shear layer. *Phys. Fluids*, 12(10):2489–2505.

[58] Rogers, M. M. and Moser, R. D. (1994). Direct simulation of a self-similar turbulent mixing layer. *Phys. Fluids*, 6(2):903–923.

[59] Sánchez, A. L., Liñán, A., and Williams, F. a. (1997). A Generalized Burke-Schumann Formulation for Hydrogen-Oxygen Diffusion Flames Maintaining Partial Equilibrium of the Shuffle Reactions. *Combustion Science and Technology*, 123(1-6):317–345.

[60] Smith, L. L., Dibble, R. W., Talbot, L., Barlow, R., and Carter, C. D. (1995). Laser Raman-Scattering Measurements of Differential Molecular-Diffusion in Turbulent Non-premixed Jet Flames of H2/CO2 Fuel. *Combustion and Flame*, 100(1-2):153–160.

[61] Soteriou, M. C. and Ghoniem, A. F. (1995). Effects of the free-stream density ratio on free and forced spatially developing shear layers. *Phys. Fluids*, 7(8):2036–2051.

[62] Spalart, P. R., Moser, R. D., and Rogers, M. M. (1991). Spectral methods for the Navier-Stokes equations with one infinite and two periodic directions. *J. Comput. Phys.*, 96(2):297–324.

[63] Spencer, B. and Jones, B. (1971). Statistical investigation of pressure and velocity fields in the turbulent two-stream mixing layer. In *AIAA Paper, no 71-613*.

[64] Sutherland, J. C., Smith, P. J., and Chen, J. H. (2005). Quantification of differential diffusion in nonpremixed systems. *Combustion Theory and Modelling*, 9(2):365–383.

[65] Thorpe, S. A. (2005). *The turbulent ocean*. Cambridge Univ. Press.

[66] Turner, J. S. (1979). *Buoyancy effects in fluids*. Cambridge Univ. Press.

[67] Vreman, A. W., Sandham, N. D., and Luo, K. H. (1996). Compressible mixing layer growth rate and turbulence characteristics. *J. Fluid Mech.*, 320:235–258.

[68] Wang, H. and Kim, K. (2015). Effect of molecular transport on PDF modeling of turbulent non-premixed flames. *Proceedings of the Combustion Institute*, 35(2):1137–1145.

[69] Wang, P., Fröhlich, J., Michelassi, V., and Rodi, W. (2008). Large-eddy simulation of variable-density turbulent axisymmetric jets. *Int. J. Heat Fluid Flow*, 29(3):654–664.

[70] Williams, F. A. (1985). *Combustion theory*. Westview Press.

[71] Wyngaard, J. C. (2010). *Turbulence in the Atmosphere*. Cambridge Univ. Press.

Appendix A

Variable density laminar mixing layer: self-similar solution

In this appendix we present the procedure followed to obtain a self-similar solution for a laminar temporal mixing layer. The configuration is the same discussed in the body of the paper for the turbulent mixing layer: two opposing streams with a velocity difference ΔU and a density ratio s. The differences with respect to equations (2.1-2.3) is that the spanwise velocity is $w = 0$, and that the rest of the fluid variables are only functions of the vertical coordinate, y, and time, t. Then, the equations governing the problem are

$$\frac{\partial \rho}{\partial t} + \frac{\partial \rho v}{\partial y} = 0, \tag{A.1}$$

$$\frac{\partial u}{\partial t} + v\frac{\partial u}{\partial y} = T\frac{\mu}{\rho_0 T_0}\frac{\partial^2 u}{\partial y^2}, \tag{A.2}$$

$$\frac{\partial T}{\partial t} + v\frac{\partial T}{\partial y} = T\frac{k}{\rho_0 C_p T_0}\frac{\partial^2 T}{\partial y^2}, \tag{A.3}$$

plus the equation of state $\rho T = \rho_0 T_0$. In these equations μ is the dynamic viscosity, κ is the thermal conductivity and C_p is the specific heat at constant pressure. Note that the vertical component of the momentum equation is not included, since it introduces an additional unknown, the mechanical pressure $p^{(1)}(y,t)$. The boundary conditions are the same as for the turbulent mixing layer, with velocity and density (temperature) going to the free-stream values when $y \to \pm\infty$.

In order to solve the system of coupled partial differential equations given by (A.1-A.3) we define the density-weighted vertical coordinate,

$$\xi = \frac{1}{\rho_0}\int_{-\infty}^{y} \rho dy. \tag{A.4}$$

We also define a characteristic length for the problem, based on the kinematic viscosity ($\nu = \mu/\rho_0$) and time, $\delta = \sqrt{\nu t}$. Then, using ξ and δ it is possible to recast equations (A.1-A.3) into a self-similar set of equations in which the time dependence is absorbed into the self-similar coordinate $\eta = \xi/\delta$,

$$\frac{\partial V}{\partial \eta} + \frac{\eta}{2}\frac{\partial \Theta}{\partial \eta} = 0, \tag{A.5}$$

$$\frac{\partial U}{\partial \eta}\frac{\eta}{2} + \frac{\partial}{\partial \eta}\left(\frac{1}{\Theta}\frac{\partial U}{\partial \eta}\right) = 0, \tag{A.6}$$

$$\frac{\partial \Theta}{\partial \eta}\frac{\eta}{2} + \frac{1}{Pr}\frac{\partial}{\partial \eta}\left(\frac{1}{\Theta}\frac{\partial \Theta}{\partial \eta}\right) = 0, \tag{A.7}$$

where $U = u/\Delta U$, $V = v/\sqrt{\nu/t}$, $\Theta = T/T_0$ and Pr is the Prandtl number. The boundary conditions for $U(\eta)$ and $\Theta(\eta)$ are $U(\pm\infty) = \mp 0.5$, $\Theta(+\infty) = (1 + s)/2$ and $\Theta(-\infty) = (1 + 1/s)/2$. Interestingly, in the self-similar set of equations, V appears only in the continuity equation, allowing to solve for $U(\eta)$ and $\Theta(\eta)$. using the momentum and energy equations only. Unfortunately, the equations only admit analytical solution when $s = 1$. For other values of s, equations (A.6) and (A.7) are solved together using Chebychev polynomials [23].